U.S. DEPARTMENT OF THE INTERIOR
U.S. GEOLOGICAL SURVEY

SAR Studies in Two Arizona Deserts: Sand Penetration, Geology, and the Detection of Military Ordnance Debris

by

Gerald G. Schaber[1] and Carol S. Breed[2]

Open-File Report 98-339

[1]U.S. Geological Survey (Emeritus), Flagstaff Field Center, Flagstaff, AZ 86001
[2]U.S. Geological Survey (Retired), Sedona, AZ 86336

1998

ABSTRACT *-Radar images acquired over two desert landscapes in southwestern and north-central Arizona demonstrate the ability of C-, L-, and P-band AIRSAR signals to backscatter, respectively, from increasingly greater depths, reaching 2 m or more in blow sand and sandy alluvium . AIRSAR images covering part of the Yuma Desert south of Yuma, Arizona, show a total reversal of C- and P-band backscatter contrast (image tone) for three geologic units. This phenomenon results in part from an increasingly greater radar imaging depth with increasing radar wavelength and the presence of a calcic soil horizon in the shallow subsurface that acts as a volume scatterer. Significantly, AIRSAR images obtained within the Barry M. Goldwater Bombing and Gunnery Range near Yuma are found to be extremely useful for detecting military ordnance debris that is located either on the surface or covered by centimeters to several meters of blow sand. The degree of detectability of this ordnance increases with SAR wavelength and is clearly maximized on P-band images processed in the cross-polarized mode (HV). This is attributed to superior penetration at P-band and the enhanced contrast in backscatter (image tone) on cross-polarized images between the radar-bright ordnance debris and the radar-dark sandy desert. In a salient of Ward Terrace in the Painted Desert of north-central Arizona, an elongated sand sheet, or sand streak, is shown to further document the increasingly greater radar imaging depths achievable in dry sand with C-, L-, and P-band AIRSAR signals, respectively. The 2.5 m maximum thickness of the studied sand streak is achieved only at P-band. This paper focuses on the interpretation of high-resolution AIRSAR images but also compares these airborne radar images with spacecraft-borne radar images.*

INTRODUCTION

Prior to NASA's Space Radar Laboratory (SRL) or Shuttle Imaging Radar-C missions (SIR-C/X-SAR) in 1994, the authors requested that the NASA/JPL AIRborne Synthetic Aperture Radar (AIRSAR) be flown over selected desert sites in southwestern and north-central Arizona as a test of radar penetration and geologic mapping in a domestic, arid-to-semiarid environment (Fig. 1). The DC-8-72 AIRSAR platform simultaneously acquires radar data in C-band (6-cm wavelength), L-band (24 cm), and P-band (68 cm)(van Zyl et al., 1990). These data can be collected in any or all of four transmit-receive polarization modes (HH, VV, HV, VH) (Evans et al., 1986, 1988; Elachi et al., 1990).

The Arizona radar-geology research described here is part of a global-scale investigation of deserts using both spacecraft-borne [e.g., SIR-C/X-SAR, European Remote Sensing satellites (ERS)] and aircraft-borne (e.g., AIRSAR) SAR sensors. The major objective is to evaluate how geologic features and structures that are mantled by blow sand and/or sandy alluvium can best be discriminated using multifrequency and polarimetric SAR. Our geologic work using SAR in deserts has been focused primarily in southern Egypt and northern Sudan--the hyperarid core of the Eastern Sahara (see **Background on SAR Signal Penetration in Deserts** below). The objective of the Saharan radar-geology research activities is to map geologic features such as duricrusts (e.g., calcretes and ferricretes), paleodrainages, and structures in sedimentary and crystalline basement rocks that are otherwise hidden by blow sand and sandy alluvium. Paleodrainages and duricrusts are known indicators of paleoclimatic conditions in desert environments while basement crystalline rocks are potential sources of economic mineral deposits.

The primary objective of the domestic radar-geology research described here is to better understand and document radar imaging depth within sand-rich sediments in a less arid and more accessible environment than North Africa.

Background on SAR Signal Penetration in Deserts

The first NASA Shuttle Imaging Radar missions (SIR-A and SIR-B) to image parts of the northeastern Sahara in the early 1980's demonstrated the capability of 24.5-cm wavelength (L-band) radar signals to return geologic information from below a few centimeters to a meter or two of loose blow sand or sandy alluvium (Schaber et al., 1986). Images produced by the return of SIR radar signals from both the surface and shallow subsurface of these sediments revealed previously unknown patterns of buried erosion surfaces, including ancient river beds ("radar-

river" channels) of widely diverse sizes (McCauley et al., 1982, 1986a,b; Breed et al., 1983, 1987; Schaber et al., 1986; Issawi and McCauley, 1992; Davis et al., 1993). Similar penetration of sandy sediments in arid environments by radar from orbital altitudes was subsequently demonstrated in the Badan-Jaran Desert of China (Guo et al., 1986), in Saudia Arabia (Berlin et al., 1986; Avery and Berlin, 1992), and in the Mohave Desert of California (Blom et al., 1984; Farr et al., 1986). One of the earliest observations of long wavelength (P-band) radar signal penetration to about 2 m into dry, windblown sediments over rough lava flows was reported from Pisgah Crater area, California, by Ellermeier et al. (1967) and Delliwig (1969). Recently, Schaber et al. (1997) documented the use of multifrequency and polarimetric SIR-C/X-SAR radar images in geologic mapping of crystalline basement rocks and other geologic features mostly covered by blow sand at Bir Safsaf in southern Egypt.

Subsurface imaging of natural geologic terrains using low frequency SAR from aircraft or orbital altitudes has to date been demonstrated to occur only where the topographic surface is relatively flat and radar smooth (image dark) and the shallow subsurface contains either some type of layered dielectric interface or disseminated dielectric inhomogeneities that backscatter strongly. It has been shown that the penetrated material must be fine grained, no more than a few meters thick, and extremely dry (e.g., with a small loss tangent, or tan δ[1] (McCauley et al., 1982; Blom et al., 1984; Schaber et al., 1986) (Table 1). General functions for depth of microwave signal penetration in unconsolidated sediments can be no more than an approximation given the wide variety of physical and chemical properties of such sediments. Depth of microwave penetration in any natural terrain (hyperarid or otherwise) is determined by many factors such as antenna gain and spreading losses, and attenuation produced from the sum of electrical conductivity, dielectric relaxation, geometric scattering, dielectric contrast between the scatterers and enclosing medium, and other losses in the shallow subsurface[2].

---

[1] **Loss tangent**: Tan $\delta = \varepsilon''/\varepsilon'$, where ε'' and ε' are the imaginary and real parts, respectively, of the complex permittivity (or dielectric constant)(See Ulaby et al., 1982).

[2] ***Surface and Volume Scattering*** - When a radar wave encounters the upper boundary surface of a two layer semi-infinite geologic medium, some of the incident energy is scattered back toward the radar antenna and the remainder is transmitted forward into the lower medium. The problem is simple if the lower geologic medium is homogeneous because scattering takes place only at the surface boundary (Ulaby et al., 1982). However, if the lower geologic medium is a mixture of materials of different dielectric properties, or inhomogeneous, then a portion of the transmitted wave scattered backward by the inhomgeneities may breach the boundary surface into and out of the upper medium to be recorded by the

In dry materials at low frequencies, dc conduction mechanisms convert electromagnetic energy into thermal energy (heat); at higher frequencies, inhomogenities scatter electromagnetic energy randomly, appearing as a loss mechanism (Schaber et al., 1986). In wet materials, the dipolar relaxation of the water molecule may also add a variety of chemical loss mechanism, if water-related mineral reactions occur[3]. The only known chemical reactions above 1 MHz occur from hydrate formation or from diffusion-limited relaxation of colloidal particles such as clay minerals (Olhoeft, 1984; Hallikainen et al., 1985; Dobson et al., 1985; Schaber et al., 1986). The effect of clay dramatically increases the real part and decreases the imaginary part of the complex dielectric constant compared, for example, to clay-free, dry sand.

Recent laboratory microwave measurements between 0.245 GHz and 6 GHz by Matzler (1998) of the permittivity of dry, fine-grained, bright red-brown (hematite-rich) sand from the Grand Erg Orientale in the Tunisian Sahara show a rather constant penetration depth of about 1 m

---

radar antenna. In this case, scattering takes place within the volume of the lower medium and is referred to as "volume scattering". Surface and volume scattering are usually both present in EM scattering from natural terrain. The spatial locations of the dielectric discontinuities mainly causing volume scattering are random; thus, one expects the waves within the volume to be widely scattered in all directions. In the case of an inhomogeneous medium with a small average dielectric constant, the angular backscattering curve is usually rather uniform. To determine the presence of volume scattering, Ulaby et al. (1982) suggest that we need to know (1) if the medium is inhomogeneous and (2) what is effective depth of penetration. [See Ulaby et al.(1982) for more details on how information (1) and (2) can be obtained.]

The effect of grain size in the penetrated medium is extremely important for volume scattering. Roth and Elachi (1975) determined that the scattering loss from volume inhomogenities is large in a general region of $0.1 < r_o/\lambda < 100$, where r_o (correlation distance) from a practical point of view represents an average of the radius of the volume scatterers. However, the SAR signal actually changes wavelength and refracts to steeper incidence angles with increasing depth (and density) in the penetrated medium. The wavelength in the penetrated medium, λ_o, is equal to $\lambda_o\sqrt{\varepsilon_o\varepsilon_a}$, where ε_o is the permittivity of free space, and ε_a is the average dielectric constant of the medium. It is important that these effects be taken into consideration when modeling radar penetration depths.

[3]Since water molecules are dipolar, they will rotate to align with an electrical field. This rotation causes some of the propagating EM energy to be converted into mechanical energy used in the rotation, and is lost as heat. When the electrical field is taken away, the molecules return to their normal state; the time required for this is called the relaxation frequency, and the entire event is referred to as dielectric relaxation (Olhoeft, 1984; Huffman III, 1992). The relaxation frequencies of diffusion-limited mechanisms are determined by the size of the particle on whose surface the reaction is occurring; normal clay particle size distributions put this relaxation in the MHz-to-GHz frequency range. However, clay minerals do not exhibit this mechanism until they are wet by several monolayers of water of more (Olhoeft, 1984; Hallikainen et al., 1985; Dobson et al., 1985). In the case of the upper meter or so of sandy sediments such as those in the Eastern Sahara sites, Schaber et al. (1986) suggested that there is generally insufficient water to activate even the small amount of clay that may be present. At what point water and clay losses appear would depend on the specific surface area of the clay, the amount of clay present, and the amount of water. Thus, the dominant mechanism operating in arid to hyperarid environments would be dc conduction and scattering loss (Schaber et al., 1986, 1997).

extending over a large frequency range (1-10 GHz). Matzler suggests, however, that pure quartz sand [i.e., without the Debye relaxation losses caused by the highly-conducting hematite] would have a still larger penetration depth. Consequently, the "volume" effects on microwave remote sensing would be even larger. These latest laboratory results are in accord with the observations described in this paper and in the earlier papers by McCauley et al. (1982, 1986a,b) and Schaber et al. (1986, 1997) on their Shuttle Imaging Radar (SIR-A, B, and C) studies in the northeastern Sahara (mentioned above).

THE YUMA SITE

The most arid desert overflown by AIRSAR in the southwestern United States is that part of the Yuma Desert that includes the Barry M. Goldwater Bombing and Gunnery Range operated by the United States Marine Corps Air Station near Yuma, Arizona (Fig. 2). The Yuma Desert occupies the southernmost part of a broad topographic and structural basin along the border of the United States with Mexico (Breed, 1998). It is bounded on the west and north by irrigated river valleys. Parts of the Yuma Desert have long been considered to be analogous in climate and terrain to parts of the North African deserts (Robinson, 1954; Van Lopik et al., 1965). The Yuma Desert is hot as well as extremely arid. It lies entirely within the 75 mm precipitation isohyet of the U.S. Weather Bureau Map of Normal Annual Precipitation (State of Arizona, 1960). On the aridity scale of Henning and Flohn (1977), the Yuma Desert ranks only a 10 compared with 200+ for the hyperarid core of the Eastern Sahara in southern Egypt and northern Sudan (McCauley et al., 1986a). The Yuma Desert is one of the most arid parts of North America and it probably has been a core North American desert for much of the Quaternary (Cole, 1986).

The southern part of the desert southeast of the Colorado River (centered at latitude 32.5°N. and longitude 114.5°W.) is a nearly level, windswept plain consisting of deposits of Tertiary and Quaternary age that fill a broad intermontane basin to depths of more than 1,000 m. The desert surface is a lag pavement of reworked alluvial pebbles and coarse sand over semi-consolidated alluvium and intercalated eolian deposits that are cemented at depths of one to two meters by a calcic soil horizon (caliche or calcrete, $CaCO_3$). The lag surface is overlain in many places by a modern eolian sand sheet as much as a meter thick, and in a few localities by fields of active barchan dunes as much as 10 m high (not shown or discussed here). Vegetation is sparse and consists mostly of creosote bushes (*Larrea tridentata*), bursage (*ambrosia dumosa)* and

bunch grass (*Hilaria*), with annuals that appear following infrequent rains.

SAR Databases

The Yuma Desert site within the Barry M. Goldwater Bombing and Gunnery Range, and including the specific area described in this paper (32° 28.6' N., 114° 28.2' W.), was imaged by AIRSAR on March 26 and June 28, 1990, and May 21, 1991 (Figs. 1,2,4; Table 2). A SPOT image (Fig. 3), used here for comparision with the SAR images was taken in 1988. Unfortunately, most of the SAR data acquired at L- and P-band during all three overflight missions were contaminated with electronic interference arising from the complex of commercial and military radars located in the Yuma area (see Fig. 4h,i). Despite this difficulty, some of the SAR images have been found to be satisfactorily calibrated with respect to the radar cross section (σ^o)(see below).

SAR images from all three AIRSAR flights over the Yuma site were processed at the Jet Propulsion Laboratory (Pasadena, California) in slant range projection using SAR Processor version 3.55 (see caption Fig. 4). These data are internally calibrated to ±2 dB with regard to radar cross section (rcs)(personal commun. - Anthony Freeman, JPL, 1993). The calibration accuracy of data acquired during the June 28, 1990, and May 21, 1991, overflights were verified using 2 m aluminum corner reflectors (van Zyl, 1990). The returns from these reflectors were analyzed using MacSigma Zero software provided by the Jet Propulsion Laboratory for quantitative analysis of AIRSAR data (Zebker et al., 1991; Freeman, 1992). Fair to excellent agreement is found between measured and theoretical rcs for one or more of the corner reflectors deployed on both the June 1990 and May 1991 AIRSAR overflights of the site. Backscatter values (dBs) for the Yuma site discussed in this paper were obtained only from AIRSAR data acquired on May 21, 1991, because these were found to be the most effectively calibrated using the corner reflectors[4]. The AIRSAR images used as illustrations in this paper are, however, limited to those acquired during the March 1990 overflight of the Yuma site. This decision was made because these SAR data include substantially less

---

[4]Note that SAR cross-calibration experiments comparing trihedral corner reflectors and truck-mounted polarimetric scatterometers by Sarabandi et al. (1994) showed that SAR calibration with trihedrals alone may lead to unreliable results. They showed that coherent and incoherent interaction of the ground with a trihedral reflector can significantly alter the expected radar cross section of an isolated trihedral corner reflector. It is not known to what extent these processes may have affected the absolute accuracy of the backscatter data shown here. Despite this uncertainty, the relative backscatter values between the various geologic units and ordnance debris sites discussed in this paper are significant.

radar interference than the data acquired during the two subsequent AIRSAR overflights of the Yuma site.

Spacecraft-borne SAR data of the Yuma site described here include a CVV SAR image acquired with the European Remote Sensing Satellite-1 (ERS-1) and XVV, CHH, CHV, LHH, and LHV images (SIR-C/X-SAR) acquired during the first of two Space Radar Laboratory missions in 1994 (described after AIRSAR results below)(Table 2).

AIRSAR Geologic Results

The AIRSAR images acquired within the Barry M. Goldwater Bombing and Gunnery Range show distinct frequency-dependent backscatter responses from the three major geologic units discussed here. Table 3 lists the level of recognition rankings for these units for each AIRSAR wavelength and polarization mode. The geologic units described include: (1) sand-mantled alluvium- sandy to small pebble alluvium mantled by a few centimeters to several meters of moderately active blow sand that supports scattered live vegetation year round (Figs. 4a; 5a); (2) scald- scabby, flat surface created by eolian deflation of the sand mantle from unit 1 above; surface characterized by a lag deposit of small pebbles and sparse, moisture-stressed or dead vegetation, especially during the dry season (Figs. 4a; 5b,c); and (3) coarse-grained river gravels- older gravels of the Colorado and Gila Rivers, which commonly form low ridges or terraces composed of medium to large cobble gravels with diameters reaching 25 cm or more (Figs. 4a; 5d). The blow sand and calichified blow sand samples collected from depths of from 0.05 and 0.40 m below the surface contained between 2.4 and 3.9 percent water (by weight) on the day of the AIRSAR overflight in May 1991.

It is noteworthy that the PHH and PVV images show a striking reversal in image tonal contrast from that observed on the C-band images for the three geologic units listed above (Fig. 4a,c,d,f, Table 3). In other words, where the CHH and CVV images show high backscatter responses (i.e., are radar bright), the PHH and PVV images show low backscatter responses (i.e., are radar dark), and vice versa. The LHH and LVV images (Fig. 4b,e), acquired at a wavelength (24 cm) intermediate to those of the C-band (5.7 cm) and P-band (68 cm), show considerably less overall visual contrast in radar backscatter between these geologic units than do the equivalent images at C-band and P-band. As would be expected, the level of backscatter from any specific geologic unit at L-band reflects an intermediate response between those found on the C-band and P-band images.

The CHH and CVV response from the sand-mantled unit is one of generally low backscatter (image dark) because of the absence of any scatter from surface rocks, the sparsity of vegetation, and the limited

radar imaging depth range (20 to 40 cm) for the 5.7-cm wavelength SAR signals in dry, loose sand with a very low tanδ value (Tables 1, 3; Fig. 4a,d).

The LHH(VV) and PHH(VV) images portray the sand-mantled alluvium units as intermediate and radar bright, respectively. The sand sheet would be distinctively image-dark at these SAR wavelengths, especially P-band, if the sand mantle was not being penetrated (Fig. 4b,c,e,f). The LHH and LVV image responses from the sand-mantled alluvium are noticeably radar-bright only at incidence angles between 25° and 40° (Fig. 4b,e). The LHH and LVV image responses become progressively more radar-dark (more C-band-like) at incidence angles larger than 40°. On the PHH and PVV images, the backscatter from the sand-mantled alluvium unit remains distinctively radar-bright throughout the 25° to 55° range in incidence angles across the image swath (Fig. 4c,f).

Four backhoe trenches were excavated on May 7, 1991, to help explain the unique backscattering differences between these geologic units at C-band and P-band, which were first discovered on analyses of the AIRSAR images of the Yuma site acquired in 1990 (not shown here) (Figs. 6a; 7). Study of the trench walls revealed that the radar-bright L-band and P-band responses from the sand-mantled alluvium are most likely attributable to penetration of the active blow sand and volume-scattering from a calcic soil horizon (including disseminated $CaCO_3$ nodules) lying about a meter or so below the surface (see footnote 2)(Figs. 6b,c). Samples of these nodules were collected and found to consist of between 42 and 47 percent $CaCO_3$ and between 29 and 58 percent quartz sand (Analyst- David Allerton, U.S. Geological Survey, Denver).

A similar explanation for unusually strong subsurface scattering from rough caliche nodules disseminated within sand-mantled sandy alluvium was reported earlier by these authors during radar-geologic evaluation of SIR-A, SIR-B, and SIR-C/X-SAR images from the southern Egyptian Sahara (Schaber et al, 1986, 1997) (**see Background on SAR Signal Penetration in Deserts** above). The caliche nodules at Yuma are, however, less dense and more moist than the "bone-dry" nodules encountered in the eastern Sahara. The disseminated nodules at the Yuma site, as in the eastern Sahara, increase in number and merge downward into a generally continuous calcrete horizon at a depth of about 1.5 to 2.5 m.

The enhanced AIRSAR backscatter response from the sand-mantled alluvium unit at L-band, and to a greater extent P-band, is therefore attributed dominantly to volume scattering from the calcic nodules described above. Backscatter from the irregular upper surface of the

underlying calcrete horizon may also be contributing to some backscatter, at least at P-band. The caliche nodules and underlying calcrete horizon are also present below the surface of the scald surfaces, which are radar dark both on the L-band and P-band images for the reasons discussed below.

The CHH and CVV responses from the scald surfaces in HH and VV polarization are characterized by moderately strong backscatter compared to the surrounding sand-mantled surfaces (Figs. 4a,d, Table 3). This backscatter is attributed to diffuse scattering of the C-band signals by the small- to moderate-size gravels that form the lag on the scald surfaces (Figs. 5b,c; 8). In contrast, the LHH, LVV, PHH and PVV responses from the scald surfaces are characterized by relatively weak backscatter (dark image tone) compared to the sand-mantled alluvium surfaces discussed above. This response is attributed to the inability of both the 24-cm and 68-cm signals to be diffusely backscattered by the small average size of the gravels that form the lag and the mirror-like specular reflection from such flat and dense, sand-free, surfaces at low SAR frequencies.

For a logical explanation of the surface scattering observed at C-band, but not P-band, from the lag on the surface of the scald unit (Figs. 4b,c,d,f; 5b,c; 8, Table 3) one can apply the Rayleigh Criterion[5] (Beckmann and Spizzichino, 1963; Peake and Oliver, 1971; Ulaby et al., 1982). This criterion and its variants conveniently relate radar wavelength and incidence angle to effective surface roughness for use in geologic studies using SAR (Schaber et al., 1976, 1997; Avery and Berlin, 1992; Sabins, 1997). Table 4 shows that the standard deviation of surface height (σ) required to produce a "Rayleigh rough" (i.e., definitely rough) response at an incidence angle (θ) of 45° is 1.83 cm at C-band. The C-band value of σ that marks the Rayleigh transition between radar smooth and radar rough

---

[5]The relation of radar wavelength and incidence angle to surface roughness is conveniently described by the Rayleigh criterion (Beckmann and Spizzichino, 1963; Peake and Oliver, 1971; Schaber et al., 1976, 1997; Sabins, 1997; Ulaby et al., 1982). The criterion considers a surface to be smooth if $h < \lambda/8 \sin\theta$, where h = the height of surface irregularities, or surface roughness [the standard deviation of surface height], λ = wavelength, and θ = incidence angle of radar wave onto a flat surface. For a random surface chararacterized by a standard deviation of surface height σ [not to be confused with radar backscatter, σ_0] the Rayleigh criterion may be expressed as $\sigma < \lambda/8 \cos\theta$ (Ulaby et al., 1982). The criterion was modified by Peake and Oliver (1971) to define the upper and lower values of h for surfaces of intermediate roughness. Their *smooth criterion* considers a surface to be clearly smooth if $\sigma > \lambda/25 \cos\theta$; their *rough criterion* considers a surface to be clearly rough if $\sigma > \lambda/4.4 \cos\theta$. Ulaby et al. (1982) suggest that while the Rayleigh criterion is useful as a first-order classifier of surface smoothness or roughness, a more stringent criterion is needed for modeling the scattering behavior of natural surfaces in the microwave region. For this purpose they adopted the so-called Fraunhofer criterion (used to define the far-field distance of an antenna) for defining a radar-smooth surface, where $\sigma < \lambda/32 \cos\theta$.

at θ =45° is 1.01 cm. Similarly, the value of σ that delineates the Rayleigh Smooth and Fraunhofer Smooth surface at C-band is 0.32 cm and 0.25 cm at 45°, respectively (See footnote 5 for definitions). It can be seen on Figure 8 that 66.5 percent of the lag gravels collected from one scald surface have maximum diameters in excess of the Rayleigh transition value of 1.01 cm. Therefore, the surface is expected to and does return a radar-bright C-band response at θ=45°, compared to the surrounding sand-mantled units.

The criteria values shown in Table 4 for P-band at θ=45° also explain the observed weak backscatter that characterizes the scald unit on AIRSAR images acquired at this frequency (Fig. 4c,f). At P-band, σ must be about 22 cm in order to act as a Rayleigh Rough surface. The Rayleigh Transition (Rayleigh Criterion), Rayleigh Smooth, and Fraunhofer Smooth values at P-band for θ=45° are about 12 cm, 4 cm, and 3 cm, respectively. P-band signals at θ=45° are dominantly reflected down range from the flat scald unit in mirror-like fashion. They are not backscattered to the SAR antenna given the rather large σ value of 12 cm required to even reach the Rayleigh Criterion that marks the transition between dominantly Rayleigh and dominantly diffuse scattering (more on the use of the Rayleigh criteria in **The ERS and SRL SAR Images**)

The coarse-grained older gravels deposited by the Colorado River show as distinctly radar-bright on the AIRSAR CHH and CVV images compared to either the sand-mantled alluvium or scald surfaces (Figs. 4a,d; 5d, Table 3). The gravels are still recognizable on the CHV image but are not nearly as distinctive there as on the co-polarized (HHVV) C-band images (Fig. 4g). The terrace of coarse river gravel is barely recognizable on the LHH and LVV images and is very poorly discernible on the LHV image (Fig. 4b,e,h). However, the gravels are distinct from their surroundings on the PHH and PVV images. They are radar dark--not radar bright--as observed on the equivalent C-band and L-band images. On the PHV image, the gravels are not easily discernible as a distinct geologic unit because the entire image is quite dark with the exception of the military ordnance that is described next.

Ordnance Detection Using AIRSAR

AIRSAR C-, L-, and P-band SAR images of the Panel Stager military ordnance targets in the southern part of the Barry M. Goldwater Bombing and Gunnery Range each reveal three large, radar-bright streaks of ordnance debris trending north-northeast (Fig. 4). These streaks of ordnance debris are not visible on the SPOT image shown in Figure 3. Two of these debris fields (T1 and T2) transect concentric circles of old automobile tires placed there to enhance visibility of the target

objective to the pilots of military aircraft (Figs. 3; 9a,b). The third streak (T3) is associated with twin mounds of dirt from which a single line of automobile tires extends to the north-northeast to mark the established flightline azimuth that is common to all three targets in the Panel Stager area (Fig. 10a). These mounds and the surrounding surfaces are covered with non-explosive military aircraft cannon projectiles (Fig. 10b).

The ability to separate metallic ordnance debris from the natural ground clutter (i.e., backscattered return from desert floor and scattered vegetation) in the vicinity of the military targets varies considerably. It depends strongly on SAR wavelength and polarization mode as indicated in Table 3. All surface vegetation is removed from within the tire circles during their construction by military personnel. As a result, the larger target circle (T1) is especially well defined as a radar-dark spot on selected AIRSAR images (see description below).

Two things are obvious after examining the AIRSAR C-, L-, and P-band images of the Panel Stager ordnance targets. First, the cross-polarized (HV) images acquired in all three wavelengths show a higher degree of contrast between the ordnance debris and the surrounding desert surface than do the co-polarized (HH or VV) images (Fig. 4, Table 3). Secondly, the PHV images are clearly superior to any other SAR wavelength/polarization combination at enhancing this contrast. The first observation can be attributed to the inherent reduction in returned signal strength (generally 4 to 17 dB) for cross-polarized signals compared to co-polarized images (see Ulaby et al., 1986). This characteristic of the cross-polarized return thus acts to reduce the overall background "clutter" arising from the desert surface, which is more apparent on the co-polarized images. Thus, the desert surface appears quite radar-dark on the HV images with the highly conductive metallic ordnance strongly contrasted as radar-bright against this background. The second observation--maximization of the contrast between the ordnance and desert background on the PHV images--is the result of both the increased radar imaging depth of P-band compared to C- and L-bands and the apparent extreme radar smoothness (image darkness) of the sandy desert floor at P-band.

An increasing amount of ordnance debris that is either totally covered or partly covered by blow sand can be seen on the images as the SAR wavelength increased from C- to L- to P-band. This is best observed on the HV image for each SAR wavelength, as indicated above and illustrated in Figure 4g,h,i. The CHV image, for example, shows sparse radar-bright ordnance up range, down range, and cross-range from the cores of the target zones. However, the amount of partly and totally buried ordnance visible outside of the core zones increases significantly

as the SAR wavelength is increased from L- to P-band (Figs. 4h,i). An especially noteworthy example is the north-northeast-trending ordnance streak northwest of target T1 and labeled A on figures 4g, h and i. This feature is barely visible on the CHV images (Fig. 4g) but is much more distinctive on the LHV image (Fig. 4h). However, it is extremely well portrayed on the PHV image where it contrasts sharply with the radar-dark desert surface.

The ability of the C-, L-, and P-band SAR signals, respectively, to detect increasingly greater amounts of ordnance buried within the blow sand at the Yuma site is attributable primarily to the potential for increasingly greater radar imaging depths as the SAR wavelength is increased (see Table 3). As shown in Table 1, the theoretical radar imaging depths for X-, C-, L-, and P-band SAR sensors can range (theoretically) between 0.2 m and 6 m in totally dry blow sand with a $\tan\delta$ and between 0.005 and 0.007. For lightly compacted, fine-grained, sandy alluvium and small-gravel alluvium ($\tan\delta$= 0.01 and 0.05, respectively), the radar imaging depths for X- C-, L-, and P-band SARs can range from 0.1 to 2.9 m. The access roads (roughly paved) and boundary fence lines in the vicinity of the three Panel Stager targets are recognized to various degrees on each AIRSAR image. The reader is referred to Fig. 4 and Table 3 for further details.

It is clear from this SAR study of the Panel Stager targets at the Yuma study site that high quality airborne SAR images, such as those acquired by AIRSAR, could be applied immediately to any ongoing Department of Defense programs to clean up ordnance debris on military ranges (Schaber et al., 1993). We have shown here that the use of PHV images could be especially useful for this purpose at sandy desert sites such as that described.

Quantitative Analyses of AIRSAR Backscatter Data

Polarimetric radar backscatter coefficient values (σ^oHH,VV,HV) for typical sand-mantled alluvium and scald surfaces just northeast of the Panel Stager target sites (Fig. 11a) confirm the radar-photogeologic observations reported above of a distinct reversal in the backscatter relationship between the scalds and sand-mantled alluvium on the P-band and C-band co-polarized images (Fig. 4a,c,d,f). The quantitative relationship in backscatter coefficient values between the sand-mantled alluvium unit and the coarse-grained river gravels is shown graphically in Figure 11b. As noted during the radar-photogeologic evaluation above, the river gravels have a significantly higher backscatter value than the sand-mantled alluvium surfaces on the CHH and CVV images (Fig. 4a,d). Conversely, the river gravel unit and sand-mantled alluvium units have a

reversed backscatter relationship on the PHH and PVV data, thus supporting the radar-photogeologic interpretations given above (Figs. 4c,f; 11b).

The qualitative interpretation of the AIRSAR images indicated that the ordnance debris fields are increasingly better contrasted against the background sand-mantled alluvium as the SAR wavelength is increased (L- and P-band), especially in the cross-polarized mode (Fig. 4; Table 3). This conclusion is supported by the quantitative results shown in figure 11c comparing the backscatter coefficient values at each SAR frequency and polarization for the sand-mantled alluvium and the Panel Stager ordnance sites.

The ERS and SRL SAR Images

The photo-equivalent "image resolution" of ERS and SRL data (~25 m) of the Yuma desert site is inherently lower than that of AIRSAR (~5 m) and the spacecraft-borne SAR images show considerably more "radar speckle" than those acquired with AIRSAR when viewed at the same scale (Figs. 4, 12, 13). As a result, details of the scald surfaces, sand-mantled alluvium, river gravels, and ordnance targets are superior on the AIRSAR images compared to the equivalent ERS and SRL images. The problem of speckle is severe with synthetic aperture radar because SAR inherently produces pixels with one independent sample per pixel, or one "look", and because a larger number of looks are possible with the considerably smaller synthetic aperture antennas on aircraft SAR platforms compared with the spacecraft-borne platform (R. Jordon, JPL- personal communication, 1997). Reducing speckle and increasing the sharpness of SAR images for optimal radar-photogeologic interpretation requires complex tradeoffs between antenna aperture, resolution, and the number of independent looks. Details on these engineering tradeoffs are given by Ulaby et al. (1982, pp. 682-687).

Given their similar incidence angles (θ=22° to θ=23°), the ERS CVV and SRL CHH images shown here are equivalent in general backscatter response for most geologic units and other surface features within the Yuma study site (Figs. 12,13b). Despite the differences in image resolution and degree of radar speckle, the backscatter characterization of most geologic units on the ERS and SRL images are, overall, similar to those on AIRSAR images acquired with an equivalent wavelength and polarization mode (Tables 3, 5).

The contacts between the scald surfaces, sand-mantled alluvium and the coarse river gravels are not readily discernible on the ERS CVV image (Fig. 12; Table 5). The ridge of coarse river gravels that is portrayed as distinctly radar-bright compared to the sand-mantled alluvium on the CVV and CHH band AIRSAR images is recognizable on the

ERS image only by the weak portrayal of the dendritic drainage channels that are cut into it--but not by any distinctive backscatter signature.

The most notable backscattering features on the ERS image are the vegetation-free interior (radar-dark circle) of ordnance target T1 and the debris-laden central core areas (radar bright) of both target T1 and target T2. The twin mounds of target T3 cannot be recognized on the ERS image. The diffuse streaks of ordnance debris revealed on the AIRSAR LHV and PHV images (described above, Fig. 4g,h,i), extending north-northeast from the central core zones of targets T1, T2, and T3, are not distinguishable on the ERS image (Fig. 12; Table 5). Similarly, the many outliers of ordnance debris that are remote from these target core zones but are increasingly well portrayed on the AIRSAR LHV and PHV images (Fig. 4h, i), respectively, are not visible on the ERS image (Fig. 12).

Sections of the access roads running northwest from the vicinity of the Panel Stager targets are recognizable as radar-dark linear features on the ERS image (Fig. 12). These roads, and the other two roads running south and northeast from their intersection just northeast of the Panel Stager targets, are radar-bright on the AIRSAR CVV and CHH images (Fig. 4a,d). This difference is attributed dominantly to the difference in incidence angle between the two SAR datasets (θ=23° for ERS and θ=45° to 55° for AIRSAR).

The only recognizable geologic contact that can be observed on the SRL XVV image is that between the moderately radar-bright Colorado River gravel terrace and the sand-mantled alluvium surface that is radar dark (Fig. 13a, Table 6). Portrayal of the complex pattern of dendritic stream channels that cut the ridge of coarse river gravel is enhanced on the XVV image by the presence of blow sand in the channel floors that absorb the X-band signals, thus returning very weak or no backscatter (radar dark).

The most prominent ordnance-related feature portrayed on the XVV image is the radar-bright spot associated with the concentration of ordnance debris at the core of target T2 (Fig. 13a). The debris core of target T1 is recognizable on this image but it is not as pronounced as that of T2. Discontinuous sectors along the tire-lined perimeter of T1 and T2 are recognizable with some difficulty on the SRL XVV image. This phenomenon is attributed to slightly enhanced backscatter from the healthy vegetation and ordnance debris that are locally concentrated around the tires (See Fig. 9).

The contact between the older Colorado River gravel terrace and sand-mantled alluvium unit is not nearly as distinctive on the SRL CHH image as on the XVV image (Fig. 13a,b). On the AIRSAR CHH image (Fig. 4a), the contact between the radar-bright gravel terrace and the radar-dark sand-mantled alluvium is much more distinctive than on the SRL CHH

image. This could be an effect of the signal-to-noise dynamics and resolution between the two SAR sensors and/or an effect of the differences in the look azimuth and/or incidence angle (θ = 22°) for the SRL image and the AIRSAR image (θ = 45°-55°).

The scald surfaces are reasonably distinctive on the SRL CHH image and appear as moderately radar-dark streaks in comparison to the surrounding sand-mantled alluvium (Figs. 5b, 13b; Table 6). This is in sharp contrast to the scalds on the AIRSAR CHH image described above that appear radar bright compared to their surroundings (Fig. 4a). These differences between the AIRSAR CHH and SRL CHH images in their portrayal of the scald surfaces could be attributable to the differences in the incidence angle between the SRL and AIRSAR images. The C-band Rayleigh transition between radar smooth and radar rough at θ = 22° takes place at 0.77 cm (see Table 4). This value is coincidentally equivalent to the average diameter (0.8 cm) of the 156 gravel pebbles collected and measured from one square meter of one scald surfaces near the Panel Stager site (Figs. 5c, 8). At θ=45° the required standard deviation of surface height for the Rayleigh transition value is 1.01 cm, or 1.3 times higher.

The north-northeast-trending ordnance streaks associated with the T1, T2, and T3 targets are not nearly as well-defined on either the ERS or the SRL SAR images as they are on the frequency- and polarization-equivalent AIRSAR images, as described above. The concentrated debris associated with the core zones (centers) of targets T1 and T2 are about equally well portrayed on the SRL CHH image as they are on the ERS CVV image. However, the vegetation-free zone inside the perimeter of target T1 that is distinctly radar dark on the ERS CVV image is much less prominent as a radar-dark feature on the SRL CHH image (Figs. 12, 13b; Tables 5, 6). There is a subtle indication on the SRL CHH image of the diffuse ordnance streak that extends to the south-southwest of the center of T2. Target T3 and the ordnance streak extending north-northeast from it are marginally visible on the SRL CHH image.

The contacts between the sand-mantled alluvium, scalds, and river gravels are noticeably sharper on the SRL LHH image (Fig. 13c) than they are on the ERS CVV and SRL CHH images described above (Figs. 12, 13b). In fact, these geologic contacts are defined somewhat better on the SRL LHH image than on the higher resolution AIRSAR LHH and LVV images (see Fig. 4b,e). This phenomenon may be attributed in part to the fact that the AIRSAR L-band data contain considerable external microwave interference (discussed above) and the SRL images were acquired at a lower incidence angle (θ =22°) than were the AIRSAR data (θ=45° to 55°). Again, note that the portrayal of the diffuse radar-bright streaks of

ordnance debris discussed here is far superior on the AIRSAR LHH image than it is on the frequency and polarization-equivalent SRL LHH image.

The coarse river gravels are slightly more radar bright than the sand-mantled alluvium on the SRL CHV image, and therefore are better backscatterers of the depolarized return. However, the contact between these two geologic units is poorly defined on the SRL CHV image compared to the SRL XVV and LHH images (Fig. 13a,c). Contacts between the sand-mantled alluvium unit and the scald unit are not recognizable on the SRL CHV image.

Somewhat broader areas of ordnance debris associated with targets T1, T2, and T3 and vicinity are visible on the SRL CHV image compared to the SRL CHH and LHH images (Fig. 13d). The twin mounds of target T3 are just resolvable on the SRL CHV image as is the broad radar-bright ordnance streak extending north-northeast from these mounds. The diffuse zone of ordnance debris located just northwest of target T1 is detectable on the SRL CHV image (see A on Figs. 13d and Figs. 4g,h,i).

Interpretation of the SRL LHV image of the Panel Stager site is severely hampered by the presence of excessive local radar interference (Fig. 13e; Table 6). Nevertheless, all three Panel Stager targets are clearly visible on the SRL LHV image with the ordnance streaks being more extensive than is observed on either the ERS image or any of the SRL images. Despite the microwave interference, the ordnance debris concentration (A) northwest of the Panel Stager targets (T1-T3) is also apparent on the SRL LHV image (Fig. 13e; also see Fig. 13d and Figs. 4g,h,i).

THE WARD TERRACE SAND STREAK

The Ward Terrace sand-penetration site in northern Arizona (35°48.4' N., 111°15.0' W.) is within the southernmost extension of the Great Basin desert in the southern part of the Colorado Plateau physiographic province. The site, in the "Painted Desert" of Arizona, is 75 km north-northeast of Flagstaff and 15 km east of the town of Cameron on the Territory of the Navajo Nation (U.S. Geological Survey, 1969)(Figs. 1; 14-16). Average annual precipitation is less than 150 mm and vegetation is very sparse, consisting of a few desert shrubs and grasses.

The elongated sand sheet or "sand streak" (Breed and Grow, 1979, pp. 281-282) that is the focus of this study crosses a salient of Ward Terrace about 60 m above the flood plain of the Little Colorado River and 240 m below the Moenkopi Plateau (adjacent northeast)(Fig. 15). The Moenkopi Plateau and Ward Terrace are underlain by sedimentary rocks (mostly sandstones) of Mesozoic age that dip gently (1 to 2 degrees) to

the northeast (Billingsley, 1987a,b). Ward Terrace has formed since the Pliocene by the erosional migration of the scarp to the northeast that marks the western border of the Moenkopi Plateau. The terrace is supported by relatively resistant silicious (silcrete) layers within the calcareous siltstones, shales, and limestones of the Owl Rock Member of the Chinle Formation of Triassic age (Ulrich et al., 1984), which are impervious to water and do not support vegetation other than grasses. Even grasses survive on Ward Terrace only where blow sand is present in a mantle sufficiently thick to store moisture from the infrequent rainfall.

The sand streak that is the primary focus of this SAR study is 7 km long and 0.5 km wide; it has a maximum depth of only 2.5 m (Figs. 15, 16a,b). The sand streak dominates the surface of a small (7.5 km X 7.5 km) salient of Ward Terrace between Landmark Wash and Tonahakaad Wash (U.S. Geological Survey, 1969)(Fig. 15). The streak extends downwind (northeastward) across Ward Terrace where it supplies sand to a substantial climbing dune at the base of the scarp at the windward edge of the Moenkopi Plateau (Figs. 15,16d). Laboratory analyses of samples collected from the sand streak show that it is composed of well sorted and unimodal quartz sand (Fig. 17). An average soil moisture content of 2.2% by weight (that is, slightly damp) was measured in the laboratory from sand samples collected in airtight containers from 0.8 m below the surface of the Ward Terrace sand streak during the May 21, 1991, AIRSAR overflight.

The sand streak on Ward Terrace is the main focus of this study. However, the SAR portrayals of the sand sheets and barchan dune fields in Landmark and Tonahakaad Washes and the channel floor of the Little Colorado River are also described below (Fig. 16e,f,g).

AIRSAR Geologic Results

Several sand streaks that extend from the Little Colorado River valley to the Moenkopi Plateau were imaged by AIRSAR on June 9, 1988, and May 21, 1991, during early engineering checkouts of the NASA/JPL AIRSAR platform (DC-8-72)(Figs. 18, 19; Table 7). Two overlapping AIRSAR passes during the May 1991 overflight paralleled the Little Colorado River, Ward Terrace, and the Moenkopi Plateau scarp (Fig. 14). SAR data acquired during these passes were processed at the Jet Propulsion Laboratory into slant range images with incidence angle ranges across the entire image swaths of θ=25° to 65° (hereafter pass A) (Fig. 18) and θ=10° to 60° (hereafter pass B) (Fig.19). Incidence angles across the salient of Ward Terrace that includes the studied sand streak range from θ=30° to θ=47° for pass A and from θ=42° to θ=54° for pass B.

Unfortunately, a highly undesirable level of aircraft motion (image smear) is present on all AIRSAR images acquired over Ward Terrace during the 1991 overflight because of a reported in-flight failure of the navigational computer on the NASA DC-8 aircraft (Mike Kobrick and Jacob van Zyl, JPL- personal communications, 1991). This resulted in processed SAR images that are generally less sharp and locally more distorted than desirable. Fortunately, however, the degree of image smear is not excessive on the specific areas of the images from pass A and pass B that include the discussed sand streak.

The 21 May 1991 SAR images shown here are internally calibrated for radar backscattering cross section to ±2 dB using JPL SAR processor version 3.56 (personal communication- Anthony Freeman and Pascale Dubois, JPL). Three meter L-band corner reflectors were set up for image calibration on an adjacent flightline during the May 1991 overflight of Ward Terrace and vicinity but, unfortunately, were not properly imaged because of a communication error with regard to reflector orientation on the ground. A European Radar Satellite-1 (ERS-1) C-band (VV only) SAR scene that includes the Ward Terrace sand streak site is also described below (see Table 7). Unfortunately, no SRL SIRC/X-SAR images were acquired of the Ward Terrace site for comparison with the AIRSAR and ERS SAR images. [Note: The priority rankings of AIRSAR images of different bands and polarization modes for portrayal of specific geologic features at the Ward Terrace sand streak site are listed in Tables 8 and 9 and should be referred to while reading the following section.]

The Ward Terrace sand streak described here is penetrated to successively deeper levels by signals from the AIRSAR C-band, L-band, and P-band radar sensors, respectively (Figs. 18, 19; Table 1). The streak is sharply-defined on the AIRSAR CHH, CVV, and CHV images acquired during both pass A and pass B (Figs. 18a,d,g; 19a,d,g; Tables 8, 9). The streak on these images is characterized by its unusually weak backscatter that contrasts strongly with the highly backscattering lag-covered bedrock surface of the terrace over which it moves (Fig. 16c). The radar imaging depth of the C-band signals into the sand streak appears to be minimal compared to the two longer wavelength SAR sensors, although it appears to be in line with theoretical estimates for C-band (See Table 1).

The sand streak is also recognizable on the LHH and LVV images acquired during pass B (Fig. 19b,e). It is, however, barely discernible on the LHV image acquired during that same pass (Fig. 19h). More significantly, the streak is virtually impossible to identify as a radar-dark feature on the LHH and LVV images acquired during pass A at an incidence angle range that is only about 20 percent smaller than observed on pass B. (Fig. 18b,e). The apparent penetration of the sand streak on the

co-polarized L-band images from pass A could possibly result from the more favorable signal refraction and penetration in sand at high incidence angles (θ = 50° or so) as reported by Elachi et al. (1984)[6].

The minimum backscatter value or darkest image tone on the LHH and LVV images acquired during pass A does coincide with the area of the streak that includes the maximum sand thickness of 2.5 m. This section of the streak coincides with an incidence angle of about 42° to 43° on the pass A images (See Fig. 18b,e). This observation suggests that the radar imaging depth of the LHH and LVV signals at this particular incidence angle does not quite reach 2.5 m--at least given the physical and electrical properties of the sand streak and underlying surface at the time of the overflight. It appears that only a slight difference in incidence angle might be significant with regard to portraying or not portraying this particular sand streak. A radar imaging depth in blow sand at L-band that is less than 2.5 m is not surprising however given the 1 to 2 m radar imaging depth reported for L-band SIR-A and SIR-B signals (at θ=50°) in blow sand and sandy alluvium in the hyperarid northeastern Sahara (Schaber et al., 1986, 1997).

Significantly, the sand streak appears to be completely "missing" from the Ward Terrace surface on the PHH, PVV, and PHV images acquired during both pass A and pass B (Figs. 18c,f,i; 19c,f,i; Tables 8, 9). At such a long radar wavelength even the maximum 2.5 m depth of the sand streak appears to have been totally penetrated. Subsurface scattering appears to be taking place from the lag-rich terrace surface underlying the thin sand streak (Fig. 16c). At P-band, where the radar penetration depth is estimated to be significantly greater in blow sand than the maximum depth of the Ward Terrace sand streak, the effect of slight differences in incidence angles would be minimal (see Table 1). Theoretically, the P-band SAR imaging depths in loose dry sand with extremely low tanδ values of between 0.007 and 0.005 may approach 4 m to 6 m under optimal conditions. Exactly how much in excess of 2.5 m the P-band radar imaging depth may be in blow sand has yet to be effectively documented in the field.

Flat, lag-covered, erosional surfaces are quite abundant on the salient of Ward Terrace that includes the studied sand streak. These lag

---

[6] Based on the SIR-A results originally reported by McCauley et al. (1982) from the northeastern Sahara, Elachi et al. (1984) showed that the presence of a thin low-loss (dry) sand layer of up to 2/3 of the skin depth (for HH) or 1/4 of the skindepth (for VV) will in effect enhance the capability to radar image the subsurface interface. For a skin depth (attenuation length) of 6 m, for example, they found that this favorable effect will occur for sand layers up to 4 m thick for HH and 1.5 m thick for VV. Elachi et. al (1984) also showed that even though the absolute backscatter cross section decreases as a function of incidence angle (θ), the presence of a dry sand layer and the resulting refraction effect can enhance the capability to image the subsurface, particularly at large incidence angles (about 50° or greater).

surfaces are very well developed near the low scarp that marks the windward, western edge of the terrace. They are characterized by a wide diversity of irregular fragments less than 3 cm in diameter derived from weathering of the local Owl Rock Member of the Chinle Formation, which supports Ward Terrace (Fig. 16c). The rock fragments that form these lags are dominantly amorphous silica (chalcedony, chert) and calcrete ($CaCO_3$). Strong radar backscatter from these lag-covered surfaces on Ward Terrace is the main reason why its surface appears more image-bright at C-band than at L-band or P-band (See ***AIRSAR Geologic Results***; and footnote 5). This is true on images acquired during both AIRSAR pass A and pass B (Figs. 18, 19; Tables 8, 9). The lag-covered areas are mostly radar-dark at P-band (especially PHH and PHV) but are also distinctive on the L-band images. The characterization of these lag surfaces is dominantly a function of the sensitivity of the specific SAR wavelength to the standard deviation of surface relief at a particular incidence angle, as discussed above.

Small intermittent stream channels on the northeast side of the Ward Terrace salient drain northeast toward the scarp of the Moenkopi Plateau. These narrow drainages have channel floors filled with sand and are therefore distinguishable on the CHH, CVV, and CHV images as radar-dark dendritic patterns (Fig. 19a,d,g-see C1; Tables 8, 9). These dendritic features are not easily distinguished on the L-band or P-band images because of the greater radar imaging depth at these larger SAR wavelengths (Fig. 19b,c,e,f,h,i). An older northeast-draining system of radar bright channels, best observed on either side of the sand streak near its southwestern terminus on the Ward Terrace salient, is seen most clearly on the L- and P-band images from both pass A and pass B (Fig. 18; 19-see C2). This clearly is attributed to the generally low level of background backscatter arising from the general surface of Ward Terrace at these SAR wavelengths. The channels appear on these images as diffuse and radar bright dendritic patterns. The C2 channels are rather poorly distinguished on the CHH, and CVV images because of the masking effect of the elevated backscatter from the general surface of the Ward Terrace salient at this SAR wavelength. The C2 channels are portrayed much better on the CHV image than on the CHH and CVV images. This arises because of the noticeable general darkening (decreased backscatter) of the Ward Terrace salient in the cross-polarized mode, especially the flat lag-covered surfaces near the southeastern terminus of the sand streak (Fig. 19g).

The boundaries of the sand streaks that occupy Landmark and Tonahakaad Washes are well defined as radar dark on the CVV images acquired during both pass A and pass B (Figs. 1, 18d, 19d; Tables 8, 9). The boundaries of the sand sheets that fill the washes are also

distinguishable on the pass B CHH image, but to a lesser degree than on the pass B CVV image (Fig. 19a). The C-band signals are clearly not penetrating the sand sheets, except locally where the sand may be dry and limited in thickness to a few tens of centimeters (See Table 1). The radar-dark sand sheets in the washes contrast extremely well at C-band (radar dark) against the lag-covered alluvial and colluvial surfaces that occupy the slightly higher terrain between the washes, and return a moderately radar-bright response. These lag-covered surfaces between the washes are Rayleigh-rough at C-band and backscatter extremely well (See footnote 5 for details).

In contrast to the CVV images discussed above, the boundaries of the sand sheets in Landmark Wash and Tonahakaad Wash are not recognizable as discrete geologic contacts on the L-band and P-band images from either AIRSAR pass A or pass B. Here, the sand sheet itself is no longer radar dark, except locally within the fields of barchan dunes and thicker sand sheet deposits, as discussed below. The absence of the radar-dark response from the sand sheets in Landmark and Tonahakaad Washes on the L- and P-band images suggests that these signals are not being totally absorbed within the low-loss sand sheets, but are indeed penetrating them to a significant degree. If this were not so, the sand sheets would appear radar-dark, like those observed on the C-band images. Thus, the P-band signals appear to be backscattering from some sort of interface or dielectric surface lying below the sand streaks. This surface could be the radar-rough, gravelly alluvium filling the washes underlying the sand streak. Alternatively, the backscatter might also arise from a buried calcic soil horizon or a salts-rich, water-saturated silt and clay interface that marks the top of the capillary zone of the shallow water table in the alluvium of the washes. Both of these types of interfaces are present locally at shallow depths within Landmark and Tonahakaad Washes. Both types of interfaces generally have a high dielectric conductivity and would backscatter effectively--especially at P-band (compare, for example, Fig. 19d,f; footnote 2).

The increasingly greater penetration with decreasing SAR frequency of the sand sheets in Landmark and Tonahakaad Washes is also well documented using the CVV, LVV and PVV images acquired during pass A (Fig. 19d,e,f). On the CVV image, for example, it is clear that the small-to-moderately large barchan dunes present on the sand sheets in the washes are totally surrounded by the radar-dark sand sheet (Fig. 16e). Thus, the sand sheet lying between the dunes is too thick to be penetrated at this SAR wavelength. On the LVV image, however, the sand sheet is significantly less pronounced as a radar-dark blanket. Where the intradune sand sheet is thickest within the field of barchans, it is slightly more radar dark than is the sand sheet farther away from the

field (Fig. 18e). This is caused by the general thicknening of the sand sheet in the intra-dune area and the fact that where the sand sheet depth exceeds about 1.5 or 2.0 m, it is not being penetrated by the L-band signals.

On the P-band image, the radar-dark sand sheet itself is no longer apparent as a radar dark deposit, even in the intradune flats within the dune fields. At P-band, the surfaces lying either below the sand sheet or interfaces within it are responsible for the moderately radar-bright returns. On the PVV image from pass A, for example, the individual barchans lying within the sand sheet are recognizable solely by their morphologic shape and the ubiquitous specular reflection that arises from their slipfaces (Figs. 16e; 18f).

The portrayal of the most recent drainage channels within the broader Landmark Wash is excellent on the CVV image from pass A (Fig. 18d; Table 8). Here, the youngest, narrow braided channels are radar bright compared to their surroundings. This results from the favorable (scattering) size of the gravels that fill the floors of those channels and the reduced amount of sand in these active runoff channels. These presently active radar-bright channels are inset within the broader extent of the wash which, as mentioned above, is mostly choked by the blow sand deposits and is radar-dark on the CVV image.

The trees and other vegetation along both banks of the Little Colorado River are seen on the SAR images from pass A as extremely radar bright, especially on the LVV and PVV SAR images that are most sensitive to vertically-oriented structures such as tree trunks, branches, plant stems, etc. The many different types and scales of roughness within the floor of the usually dry river channel are, as would be expected, portrayed very differently on the C-, L-, and P-band SAR images. Desiccation polygons of different sizes composed of fine silt and clay are abundant on the floor of the river channel (Fig. 20). The extremely smooth polygon surfaces themselves may appear radar-smooth (i.e., specular reflectors- image dark) at the shorter C-band wavelength while appearing quite radar-rough (diffuse scatterers-image bright) at L-, and/or P-band. This can be attributed to the sensitivity of the two longer wavelength SAR sensors to a scale that is larger than a single polygon. Thus, L-band and especially the P-band signals are strongly affected by the fractures with consistent angular relationships that bound the polygons, as well as by dielectric contrasts associated with the salt-rich water and void spaces between and below the polygons. Such parameters were found to strongly affect SAR returns in early L-band SAR studies of Death Valley (Schaber et al., 1976, 1993).

Quantitative Analyses of AIRSAR Backscatter Data

The relationship between the polarimetric radar backscatter coefficient (σ^o) values for the Ward Terrace sand streak and the general surface of the terrace away from the sand streak is shown in Figure 21a. As strongly suggested from the qualitative radar-photogeologic study of the AIRSAR images, the largest contrast in radar backscatter between these two surfaces is at C-band. The differences in the backscatter coefficient values for CVV, LVV, and PVV, for example, are 5 dB, 4 dB, and 1.5 dB, respectively. The differences in HH mode are similar at 5.5 dB, 3.0 dB, and 2.0 dB, respectively. Similarly, Figure 21b shows the polarimetric σ^o values for the general surface of the terrace away from the streak and the lag surfaces described above. Again, these quantitative results confirm those qualitative observations from analysis of the SAR images that showed that the lag surfaces are much more contrasted with the general terrace surface at lower SAR frequencies. The differences in the value of σ^o for CVV, LVV, and PVV, for example, are ~0 dB, 4 dB, and 5.5dB, respectively. The differences in the value of σ^o for CHH, LHH, and PHH are 2 dB, 5 dB, and 6.8 dB, respectively.

ERS SAR Image

Although characterized by considerably more radar speckle than the higher resolution AIRSAR CVV image of the same frequency and polarization mode discussed above, an enlarged part of an ERS SAR scene (CVV) of the Ward Terrace site and vicinity (Fig. 22) shows the same sharp contrast between the radar dark sand streak and the overall radar bright surface of Ward Terrace (Figs. 18d, 19d; Table 4). The sand that occupies Landmark Wash and Tonahakaad Wash is also radar-dark compared to the surrounding lag-covered surfaces that are radar bright on the ERS image. These backscatter responses are in excellent agreement with those reported above for the AIRSAR CVV image.

CONCLUSIONS

The Arizona SAR studies reported here further document the ability of SAR images acquired at diverse wavelengths and transmit/receive polarizations to be a valuable tool for surface and shallow subsurface geologic studies in sand-rich arid environments. The detection of military ordnance both at the surface and shallowly buried by blow sand at the Barry M. Goldwater Bombing and Gunnery Range near Yuma has been shown to be optimal on AIRSAR P-band images processed in the cross-polarized mode (HV). These results suggest that the application of the state-of-the-art NASA/JPL AIRSAR, or a similar multifrequency,

polarimetric aircraft SAR facility should be evaluated as an "operational" tool for cleanup of such military ordnance sites--at least in desert regions.

The reversal in image contrast described above for several geologic surfaces on C- and P-band images of the Yuma site certifies the important role of radar imaging depth in geologic studies of deserts. These results also emphasize the importance of using at least two SAR sensors that cover as wide a spread in frequency as possible for geologic investigations and potential cleanup (or monitoring) of military ordnance training sites in arid environments.

The wavelength- and incidence angle-dependence of radar imaging depth described at the Ward Terrace sand streak site in north-central Arizona also emphasizes the need for carefully matching SAR sensor parameters for specific types of geologic and other investigations. In both sites described here, Yuma and Ward Terrace, the C- and P-band SAR sensors proved to be the most complementary. The discrimination of geologic surfaces or shallow subsurface features on the L-band images is found, as would be expected, to be intermediate to those of the C- and P-band images. Therefore, when restricted to only two SAR sensors, the C- and P-band SARs would be preferable, especially those in desert environments where an otherwise obscuring thin sand mantle creates a problem for more conventional visible-wavelength sensors such as those carried by LANDSATand SPOT.

The results described here are in excellent agreement with those reported from Shuttle Imaging Radar (SIR-A, SIR-B, SIR-C) investigations by the authors and others working in the Eastern Sahara. This similarity is especially noticeable with regard to the significance of disseminated caliche (CaC03) nodules in blow sand as volume-scatterers of long wavelength SAR signals, and the relative magnitude of radar imaging depths with increasing SAR wavelength.

As suggested by Matzler (1998) "Quantitative information of the electromagnetic properties of arid surfaces over a broad frequency range is largely missing." The effects of common sand contaminants (e.g., hematite, CaC03, salts, etc.) on microwave permittivity of sand clearly need to be addressed in both the laboratory and field contexts. This is especially true now that significant microwave signal penetration of sand has been documented by our own radar-geologic investigations, as well as those of other researchers. We propose that a priority be considered among the radar geologic community to design relevant quantitative (calibrated) tests both in the laboratory and field settings to precisely determine the radar imaging depth (i.e., the two-way penetration depth into and out of a penetrated medium) of long

wavelength radar signals from airborne and spaceborne alitudes in sandy and other fine-grained, dry to wet sediments.

Acknowledgments

Special thanks are due the radar engineers, pilots, aircraft maintenance crews, mission planning teams and radar-program managers at JPL (Pasadena CA) and NASA/AMES (Mountain View CA), and to Dr. Miriam Baltuck of the Solid Earth Branch at NASA HQ (Washington DC) for their many contributions to the very successful AIRSAR Program. We also acknowledge the various Commander(s) and staff personnel of the Yuma Marine Corps Air Station at Yuma for their outstanding cooperation, logistical support, and special access to the Barry Goldwater Bombing And Gunnery Range. Special thanks are also due to John F. McCauley and Graydon L. Berlin for reviewing the manuscript, and to David "John" Chadwick for his able assistance during field work and in digital processing of some of the SAR data presented. We also recognize Hugh Thomas for his superior work in the photolab, Darlene Casebier for preparation of selected illustrations, and David Allerton (USGS-Denver) for chemical and petrological analyses of the caliche nodule samples collected from the Yuma site. This research was made possible by SIR-C funding to G. Schaber from NASA /JPL to the U.S. Geological Survey (Contract WO8864) and to Northern Arizona University, Flagstaff AZ (Contract # 960529).

REFERENCES

Avery, T,E., and Berlin, G.L., 1992, *Fundamentals of Remote Sensing and Airphoto Interpretation*, 5th edition, 472 p., MacMillan, New York, NY.

Beckmann, P., and Spizzichino, A., 1963, *The Scattering of Electromagntic Waves From Rough Surfaces*, Macmillan, New York.

Berlin, G.L., Tarabzouni, M.A., Al-Naser, A., Sheikha, K.M., and Larson, R.W., 1986, SIR-B subsurface imaging of a sand-buried landscape: Al Labbah Plateau, Saudi Arabia. *IEEE Trans. on Geoscience and Remote Sensing*, GE-24:595-602.

Billingsley, G.H., 1987a, Geologic map of the southwestern Moenkopi Plateau and southern Ward Terrace, Coconino County, Arizona; U. S. Geological Survey Misc. Invest. Series Map I-1793; scale 1:31,680.

Billingsley, G.H., 1987b, Geology of the southwestern Moenkopi Plateau and southern Ward Terrace, Arizona, *U.S. Geological Survey Bulletin* 1672, 18 p.

Blom, R.G., Crippen, R.E., and Elachi, Charles, 1984, Detection of subsurface features in Seasat radar images of Means Valley, Mojave Desert, California. *Geology*, 12:346-349.

Breed, C.S., 1998 (?), Monitoring surface changes in desert areas: In Breed, C.S., and Reheis, M. (eds.), The Desert Winds Project: Monitoring wind-related surface processes at desert sites in Arizona, New Mexico, and Californiua: *U.S. Geol. Survey Prof. Paper 1598.*

Breed, C.S. and Grow, Teresa, 1979, Morphology and distribution of dunes in sand seas obeserved by remote sensing:, In McKee, E.I. (ed.), A study of global sand seas, *U.S. Geol. Survey Prof. Paper 1052.* pp. 253-302.

Breed, C.S., McCauley, J.F., and Davis, P.A., 1987, Sand sheets of the Eastern Sahara and ripple blankets on Mars, In Frostick, L., and I. Reid (Eds.). *Desert Sediments: Ancient and Modern.* Geol. Sci. Special Publ. 35,:337-359 London.

Breed, C.S., Schaber, G.G., McCauley, J.F., Grolier, M.J., Haynes, C.V., Elachi, Charles, Blom, Ron, Issawi, Bahay, and McHugh, W.P., 1983, Subsurface geology of the Western Desert in Egypt and Sudan revealed by Shuttle Imaging Radar (SIR-A): First Spaceborne Imaging Radar Symposium, Jet Propulsion Laboratory Pub. 83-11, Pasadena, Calif., pp. 10-12.

Cole, K.L.,1986, The Lower Colorado River Valley: A Pleistocene desert, *Quaternary Research*, 25:392-400.

Davis, P.A., Breed, C.S., McCauley, J.F., and Schaber, G.G., 1993, Surficial geology of the Safsaf region, south-central Egypt, derived from

remote-sensing and field data: *Remote Sensing of Environment*, 46:183-203.

Delliwig, L.F., 1969, An evaluation of multifrequency radar imagery of the Pisgah Crater Area, California, *Modern Geology*, 1:65-73.

Dobson, M.C., Ulaby, F.T., Hallikainen, M.T., and El-Reyes, M.A., 1985, Microwave dielectric behavior of wet soils-Part II: Dielectric mixing models: *IEEE Trans. on Geoscience and Remote Sensing*, GE-23:35-46.

Elachi, Charles, Roth, L.E., and Schaber, G.G., 1984, Spaceborne radar subsurface imaging in hyperarid regions: *IEEE Trans, Geosci. and Remote Sensing*, v. GE-22:383-388.

Elachi, Charles, Kuga, Y., McDonald, K.C., Sarabandt, Senior, T.B.A., Ulaby, F.T., van Zyl, J.J., Whitt, M.W., and Zebker, H.A., 1990, *Radar polarimetry for geoscience applications*, F.T. Ulaby and C. Elachi editors, Artech House, Inc.

Ellermeier, R.D., Simonett, D.S., and Dellwig, L.F., 1967, The use of multi-parameter radar imagery for the discrimination of terrain characteristics: *IEEE Intern. Convention Record, part 2*, pp. 127-135.

Evans, D.L., Farr, T.G., Ford, J.P., Thompson, T.W., and Warner, C.L., 1986, Multipolarization radar images for geologic mapping and vegetation discrimination: *IEEE Trans. on Geoscience and Remote Sensing*, 24:246-257.

Evans, D.L., Farr, T.G., van Zyl, J.J., and Zebker, H.A., 1988, Radar polarimetry: Analysis tools and applications: *IEEE Trans. on Geoscience and Remote Sensing*, 26:774-789.

Farr, T.G., Elachi, Charles, Hartl, P.H., and Chowdhury, K., 1986, Microwave penetration and attenuation in desert soil: A field experiment with the Shuttle Imaging Radar, *IEEE Trans. on Geoscience and Remote Sensing*, GE-24:590-594.

Freeman, A., 1992, SAR Calibration: An Overview, *IEEE Trans. on Geoscience and Remote Sensing*, 30:1107-1121.

Guo, Haudong, Schaber, G.G., and Breed, C.S., 1986, Shuttle imaging radar response from sand and subsurface rocks of Alashan Plateau in north-central China, Intern. Symp. on Remote Sensing For Resources Development and Environmental Management, 7th, Proceedings ISPRS Comm. VII, pp. 137-143, Enschede, Netherlands, Balkema, Boston.

Hallikainen, M.T., Ulaby, F.T., Dobson, M.C., El-Reyes, M.A., and Wu, Lin-Kun, 1985, Microwave dielectric behavior of wet soil-Part I: Empirical models and experimental observations: *IEEE Trans. on Geoscience and Remote Sensing*, GE-23:25-34.

Henning, D., and Flohn, H., 1977, Climate aridity index map, United Nations Environment Programme: Nairobi.

Huffman III, A.C., 1992, Chararacterization of Three-dimensional Geological Heterogeneities Using Ground Penetrating Radar, Master of Science Thesis (Geophysical Engineering), Colorado School of Mines, Golden, Colorado, 189 p.

Issawi, Bahay, and McCauley, J.F., 1992, The Cenozoic Rivers of Egypt: The Nile problem: In Friedman, R., and Adams, B. (Eds.), *Followers of Horus: Studies in Ancient Egypt* dedicated to M.A. Hoffman. Oxbow, Oxford: pp.1-18.

Matzler, Christian, 1998, Microwave permittivity of dry sand, *IEEE Transactions on Geoscience and Remote Sensing*, 36:317-319.

McCauley, J.F., Schaber, G.G., Breed, C.S., Grolier, M.J., Haynes, C.V., Issawi, Bahay, Elachi, Charles, and Blom, R., 1982, Subsurface valleys and geoarchaeology of the Eastern Sahara revealed by Shuttle Imaging Radar: *Science*, 218:1004-1020.

McCauley, J.F., Breed, C.S. and Schaber, G.G., 1986a, The megageomorphology of the radar rivers of the eastern Sahara, in *The Second Spaceborne Imaging Radar Symposium* (28-30 April 1986), JPL Pub. 86-26, Jet Propulsion Laboratory, Pasadena, Calif., pp. 25-35.

McCauley, J.F., Breed, C.S., Schaber, G.G., McHugh, W.P., Issawi, Bahay, Haynes, C.V., Grolier, M.J., and El-Kilani, A., 1986b, Paleodrainages of the eastern Sahara- The radar rivers revisited: *IEEE Trans. on Geoscience and Remote Sensing*, GE-24, pp. 624-648.

Olhoeft, G.R., 1984, Applications and limitations of ground penetrating radar: In expanded abstrs. Soc. Explor. Geophys., 54th Ann. Int. Meet. Expos. (Atlanta, GA, Dec. 2-9, 1984), pp. 147-148.

Peake, W.H., and Oliver, T.L., 1971, The response of terrestrial surfaces at microwave frequencies, Ohio State Univ. Electroscience Lab. 1440-7, Tech. Rept. AFAL-TR-70-301, Columbus, Ohio.

Robinson, W.C., 1954, Analogs of Yuma climate in northeast Africa, Research Study Rept., U.S. Army Corps of Engineers Environmental Analog Project, Rept. no. (7-83-03-005A).

Roth, L.E. and Elachi, Charles, 1975, Coherent electromagnetic losses by scattering from volume inhomgeneities: *IEEE Trans. Antennas and Propog.*, AP-23:674-675.

Sabins, F.F., 1997, *Remote Sensing-Principles and Interpretation*, Third Edition, 494 p., W.H. Freeman and Company, New York.

Sarabandi, K., Pierce, L.E., Oh, Y., Dobson, M.C., Ulaby, F.T., Freeman, A., and Dubois, P., 1994, Cross-calibration experiment of JPL AIRSAR and truck-mounted polarimetric scatterometer, *IEEE Trans. on Geosc ience and Remote Sensing*, GE-32:975-985.

Schaber, G.G., Berlin, G.L., and Brown, W.E., Jr., 1976, Variations in surface roughness within Death Valley, California: Geologic evaluation of

25-cm wavelength radar images, *Geol. Soc. America Bull. 87*, pp. 29-41.

Schaber, G.G., and Berlin, G.L., 1993, Death Valley, California: Surface micro-relief statistics and radar scatterometer data: *U.S. Geol. Surv. Open-File Report 93-272*, 43 pages, 54 figures, and 30 tables.

Schaber, G.G., and Breed, C.S., 1993, Subsurface mapping with imaging radar in deserts of Africa and Arizona, *Geoscientific Research in Northeast Africa*, In U. Thorweihe, and H. Schandelmeier (Eds.); pp. 761-765; Balkema, Rotterdam.

Schaber, G.G., Breed, C.S., and Chadwick, D.J., 1993, Location of surface and shallow subsurface ordnance at the Barry M. Goldwater (Luke Air Force) Range (Yuma, Arizona) using airborne synthetic aperture radar (AIRSAR), *Proceedings of the Range Cleanup Workshop*, Vol. II, Naval Postgraduate School, Monterey, Calif. (March 23-25, 1993), Advanced Technology Division., Yuma Proving Ground STEYP-MT-I, Yuma, Arizona.

Schaber, G.G., McCauley, J.F., and Breed, C.S., 1997, The use of multifrequency and polarimetric SIR-C/X-SAR data in gelogic studies of Bir Safsaf, Egypt, Remote Sens. Environ. 59:337-363.

Schaber, G.G., McCauley, J.F., Breed, C.S., and Olhoeft, G.R., 1986, Shuttle imaging radar: Physical controls on signal penetration and subsurface scattering in the eastern Sahara: *IEEE Trans. on Geoscience and Remote Sensing*, GE-24:603-623.

State of Arizona, 1960, Normal Annual Precipitation in Inches, (1931-1960), U.S. Department of Commerce, Environmental Science Services Administration Weather Bureau, Western Region, WR-1210-A, Salt Lake City, UT.

Ulaby, F.W., Moore, R.K., and Fung, A.K., 1982, Microwave Remote Sensing-Active and Passive, vol. II-Radar Remote Sensing and Surface Scattering and Emission Theory: Addison-Wesley, Reading, Mass., Chapter 11 (Physical mechanisms and empirical models for scattering and emission), pp. 816-921.

Ulrich, G.E., Billingsley, G.H., Hereford, Richard, Wolfe, E.W., Nealey, L.D., and Sutton, R.L., 1984, Map showing geology, structure, and uranium deposits of the Flagstaff 1 degree X 2 degree quadrangle, U. S. Geological Survey Misc. Invest. Ser. Map I-1446 (1), 1:250,000.

U. S. Geological Survey, 1969, The Landmark Quadrangle, Arizona, Coconino Co., 7.5 Minute Series (topographic), scale 1:24,000.

U.S. Department of Commerce, 1960, Normal Annual Precipitation in inches, 1931-1960, State of Arizona, U.S. Weather Bureau Map of Normal Annual Precipitation: WR1210A.

Von Hippel, Arthur,(Ed.), 1954, *Dielectrics and Waves, p. 26-37,* New York, John Wiley. and Sons.

Van Lopik, J.R., Kolb, C.R., and Shamburger, J.H., 1965, Analogs of Yuma terrain in the northwest African desert, U. S. Army Engineer Waterways Experiment Sta. Tech. Rept. 3-360, Vicksburg, Mississippi.

van Zyl, J.J., 1990, Calibration of polarimetric radar images using only image parameters and trihedral corner reflector responses: *IEEE Trans. on Geoscience and Remote Sensing*, 28:337-348.

van Zyl, Zebker, H.A., and Elachi, Charles, 1990, Polarimetric SAR applications, chapter 7 in F. Ulaby and C. Elachi (Eds.) *Radar Polarimetry for Geoscience Applications*, Artech House, Inc., Norwood MA, 364 p.

Zebker, H.A., van Zyl, J.J., Durden, S.L. and Norikane, L., 1991, Calibrated imaging radar polarimetry- Technique, examples, and applications, *IEEE Trans. Geoscience and Remote Sensing*, 29:942-961.

LIST OF TABLES

FIGURE CAPTIONS

Figure 1-Index map of Arizona showing the location of the Yuma and Ward Terrace radar study sites (see Figs. 2 and 14 for additional details on sites); north at top of figure.

Figure 2- General location map of the study area south of Yuma, Arizona, showing the location of the Panel Stager target sites (T1, T2, and T3) on the Barry M. Goldwater Bombing and Gunnery Range (BGBGR) (See Fig. 1). Rectangle (Yuma Study Site) corresponds to identical footprints for the Landsat TM (Fig. 2), AIRSAR, ERS SAR and SRL (SIR-C/X-SAR)(Figs. 3-5) SAR images shown in paper; north at top of figure.

Figure 3-Part of SPOT panchromatic scene showing the Panel Stager target site on the BGBGR. SPOT Image 27 acquired June 1988. The location of sand-mantled alluvium, scalds and coarse older river gravels are indicated. The area shown is the same as that shown on Figs. 4, 12, and 13 below. Note the portrayal of targets T1, T2 and T3 (compare with portrayal on Figs. 4; 12). Image 17.6 km across; north at top of image.

Figure 4-AIRSAR slant-range images from flightline 290-1 (March 26, 1990) showing the Panel Stager target area of the BGBGR described in the text: (a) CHH, (b) LHH, (c) PHH, (d) CVV, (e) LVV, (f) PVV, (g) CHV, (h) LHV, (i) PHV (see Fig. 1, Table 3). Incidence angles (degrees) across slant range image swath indicated on left edge of image (a) only but also apply to images (b)-(i). Locations of the terrace of older coarse river gravels, ordnance targets T1, T2 and T3, access roads, and fence lines are indicated on some images. See (b) for identification of sand-mantled alluvium and scald surfaces described in text. Examples of radar interference patterns identified on images (b) and (h). Increasingly greater amounts of ordnance located remote from targets T1, T2, and T3 are identifiable with increasing SAR wavelength on the HV images (g, h, and i); A, (on g, h and i) locates a major northeast-trending older ordnance target northwest of target T1. Dotted radar-bright boundary fence line (metal) prominent in the northwest quadrant of the PHV image (i). Images 17.6 km across. North at top of image. [For definition and geometry of slant range projection of SAR images see Sabins (1997, pp. 181-182).]

Figure 5- (a) Typical sand-mantled alluvium surface at site of backhoe trench 2 (BHT-2 in text) with sparse, but living creosote bushes (*Larrea tridentada*), bursage (a desert shrub), and bunch grass (*Hilaria*), (b) Lag-covered scald at the site of backhoe trench-3; surface formed by wind deflation of sand from the adjacent sand-mantled alluvium surfaces shown in (a) above; (c) closeup of the lag gravel on scald shown in (b) (See Fig. 8); (d) outcrop showing the very coarse grained ancestral Colorado River gravels; meter stick in foreground (see Fig. 4).

Figure 6- (a) Backhoe excavating sand-mantled alluvium unit at the Yuma study site on May 7, 1991; (b) wall of backhoe trench number 3 (BHT-3) showing disseminated caliche nodules and lower calcrete horizon in semi-consolidated, reworked (oxidized-reddish) sand sheet; (c) close-up of caliche nodules from BHT-1 that are similar to those shown in (b).

Figure 7- Correlation of percent by weight and grain size (in mm) for samples from backhoe trenches (BHT) excavated within the Panel Stager study site near Yuma (See Fig. 2 for location) [Note-grain sizes >0.1 mm and >0.7 mm are listed as single percentage values]; (a) upper 25 cm thick blow sand at BHT-2 (2 m deep) excavated in a sand-mantled alluvium surface; (b) upper caliche zone from 50 cm to 1 m depth in blow sand from BHT-2; (c) gravelly alluvium from base (~2 m) of BHT-2 [Note->40% of sample weight is from gravels that exceeds 0.7 mm in diameter; (d) upper 0.5 m sandy matrix (not including surface lag gravel) from BHT-3 excavated in a scald surface (i.e., very flat, lag-covered surface, no blow sand) (see Figs. 5b,c; 8); sand-sized material (0.1 mm -0.6 mm) is distinctly bi-modal.

Figure 8- The number of gravel of a given diameter (mm) collected from a 1 m by 1 m square near BHT-3 on the scald surface shown in Figure 5b,c.

Figure 9- (a) Partial ground-level photographic pan of target circle T1; (b) closeup of ordnance debris within target circle T1.

Figure 10-(a) Twin-mound ordnance target T3 at the Panel Stager site (See Fig. 4); (b) Line of automobile tires extending north of twin-mound ordnance target T3 (shown in a) to mark the military bombing and gunnery approach azimuth.

Figure 11- Comparisons of measured radar backscatter coefficient (σ^o) values at HH, VV and HV for various combinations of the three discussed geologic surface units and the ordnance streak from target T1; (a) sand-mantled alluvium and scald; (b) sand-mantled alluvium and older river gravels; (c) sand-mantled alluvium and ordnance streak.

Figure 12- Subscene from European Remote Sensing Satellite-1 (ERS-1) PRI SAR image (CVV) showing the same area of the Yuma study site shown in Figures 3 and 4 above. Image CCT ID:1792 (Canadian Radar Data Centre); orbit 4466, track 317; scene center: 32° 44' 13" N., 114° 29'00" W. Date of acquisition May 23, 1992; north at top of image. The ERS satellites (1 and 2) are designed, constructed and managed by the European Space Agency-esa (see Fig. 2, Table 5). Image 17.6 km across; north at top of image.

Figure 13-SRL1 X, C, and L-band SAR images (SIR-C/X-SAR) showing the same area that is shown in Figs. 1-4; (a) XVV, (b) CHH, (c) LHH, (d) CHV, and (e) LHV (see Fig. 2; Table 6). [Note scalds indicated on (b) are radar-dark, not radar-light as on the AIRSAR CHH image shown in Fig. 4a (see text discussion on incidence angle effects)). [Note: significant radar interference patterns on the LHV image (e).] Ordnance site northwest of targets T1, T2 and T3 discussed in text is shown at A on image (e)(see Fig. 4g,h,i). The SRL1 X-SAR data were acquired in VV polarization mode only; SIR-C1 SAR images were acquired only in HH and HV polarization during data take 56.30 and have an incidence angle of 22° (see Table 2). SAR data acquired in April 1994. Images 17.6 km across. North at top of images.

Figure 14-Index map and geologic sketch map of the Ward Terrace site in north-central Arizona. Ground footprints of AIRSAR and ERS-1 SAR images shown in figures 18, 19 and 22 are indicated by rectangles. Contour interval 200 feet.

Figure 15- U-2 aerial photograph (from 20,000 m altitude) showing an oblique view (looking northeast) across the Little Colorado River and Ward Terrace in the Territory of the Navajo Nation in north-central Arizona (See Figs. 1, 14). The studied sand streak, Ward Terrace, the Little Colorado River, Landmark and Tonahakaad Washes, and the Moenkopi Plateau are labeled. Image 22.5 km across base. Inset image- handheld aerial photograph showing the climbing dune (see Fig. 16d) and the associated sand streak described here on Ward Terrace (photograph courtesy of John F.

McCauley-Sedona, Arizona). U-2 photograph courtesy of the U. S. Air Force (Image ID: 374R-001, Sept. 6, 1968).

Figure 16- Ground photographs of the sand streak study site on Ward Terrace: (a) low-relief sand streak (arrows) observed from ground level. Note person (height 1.88 m) standing on the highest point of the sand streak (2.5 m above the photo station), (b) closeup of the sand streak surface showing the abundance and type of vegetation (mostly grasses); (c) closeup of lag-covered surface near the windward scarp of the Ward Terrace adjacent to the sand streak described here. Note the small size of lag fragments (mostly light-colored amorphous silica, or silcrete, and caliche-$CaCO_3$)(large divisions on meter stick are 10 cm)(see Fig. 11); (d) climbing dune rising to just a few meters below the near-vertical cliff forming the scarp of the Ward Terrace salient containing the studied sand streak (see Fig. 15). Such sand ramps are presently being eroded from the cliff head (also see Fig. 15); (e) barchan sand dunes (background) in Landmark Wash (foreground). Similar dune fields are also present in Tonahakaad Wash south of Landmark Wash (see Figs. 14; 15; 18f; 19).

Figure 17- Correlation between percent (by weight) and sand grain size (mm) for the Ward Terrace sand streak. Sample collected May 21, 1991, from crest of sand streak ~60 m from where it surmounts the Ward Terrace scarp.

Figure 18- Multifrequency and fully polarimetric SAR images from AIRSAR flightline Moenkopi 340-2 (here referred to as pass A) over the studied Ward Terrace sand streak in north-central Arizona on May 21, 1991; (a) CHH, (b) LHH, (c) PHH, (d) CVV, (e) LVV, (f) PVV, (g) CHV, (h) LHV, (i) PHV (See Figs. 14,15; Table 8). Typical lag surfaces on studied salient of Ward Terrace indicated on LHH image (b). Contacts of sand sheet deposits in Landmark and Tonahakaad Washes indicated on CVV image (d); dunes indicated on PVV image (f). Slant range image format (for description of slant range geometry see Sabins, 1997, p. 181). Range in incidence angles across swath and north arrow common to all of the images are shown on image (a). Image width is ~12 km (See Figs. 1, 14, 19; Table 1); north indicated on (a).

Figure 19- Multifrequency and fully polarimetric AIRSAR images from flightline Moenkopi 340-6 (May 21, 1991)(here referred to as pass B) showing the studied Ward Terrace sand streak and a segment of

the Little Colorado River in north-central Arizona; (a) CHH, (b) LHH, (c) PHH, (d) CVV, (e) LVV, (f) PVV, (g) CHV, (h) LHV, (i) PHV (See Figs 14, 15; Table 9). Slant range image format. Radar-dark dendritic channels (C1) and radar-light dendritic channels (C2) described in text are labeled on CHH image (a). Range in incidence angle and north arrow shown on image (a). Image width is ~12 km; north arrow shown on (a) (See Figs. 1; 14; 18; Table 1).

Figure 20- Ground photograph showing (a) general view across the dry bed of the Little Colorado River that exhibits variable surface roughness; (b) close-up photo of the silt and clay desiccation polygons that characterize the section of the river bed included in the pass A images; 10 cm rule on surface; photographs acquired in December 1989.

Figure 21- Comparisons of measured radar backscatter coefficient (σ^o) values at HH, VV and HV for various combinations of the geologic units described on Ward Terrace; (a) terrace surface and sand streak; (b) terrace surface and lag surface.

Figure 22- Subscene from European Remote Sensing Satellite-1 (ERS-1) PRI SAR image (CVV) showing the Ward Terrace sand streak site and the region between the Little Colorado River and the Moenkopi Plateau (see Figs. 1, 14, 15, 18; 19). Image CCT ID is S0005744 (work order No. S043380) (Canadian Radar Data Centre); orbit 4881, track 227; scene center: 35° 36' 54" N., 110° 51'16" W. Date of acquisition June 21, 1992; north at top. [The ERS-1 and ERS-2 satellites are designed, constructed and managed by the European Space Agency-esa] Image is 18.5 km across (see Table 7).

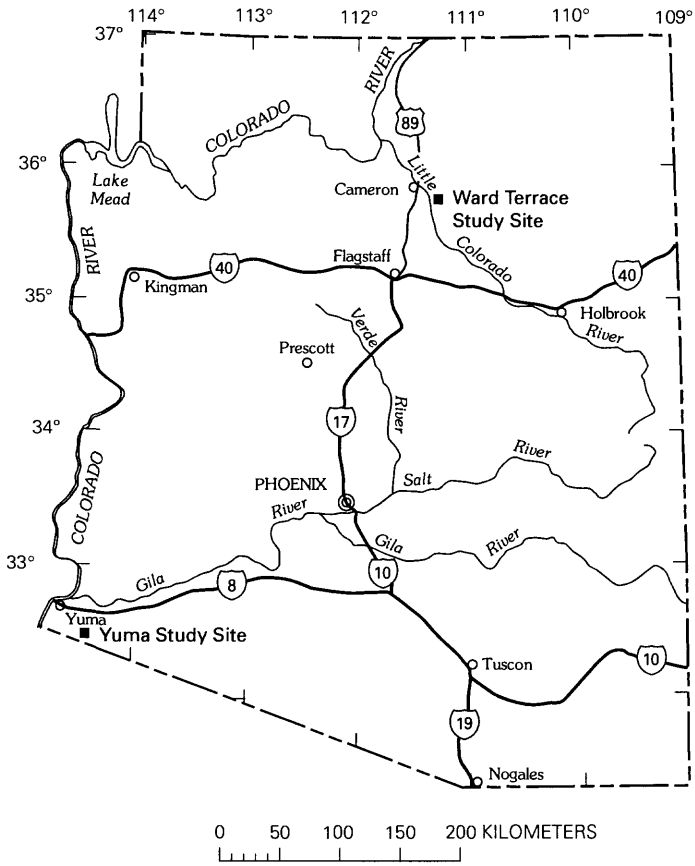
114°
113°
112°
111°
110°
109°
37°
36°
35°
34°
33°
COLORADO
RIVER
Little
Colorado
River
Lake
Mead
RIVER
COLORADO
Cameron
Ward Terrace
Study Site
Flagstaff
Kingman
Holbrook
Prescott
Verde
River
Salt
River
PHOENIX
River
Gila
River
Gila
River
Yuma
Yuma Study Site
Tuscon
Nogales
89
40
40
17
10
8
10
19
0 50 100 150 200 KILOMETERS

Figure 1

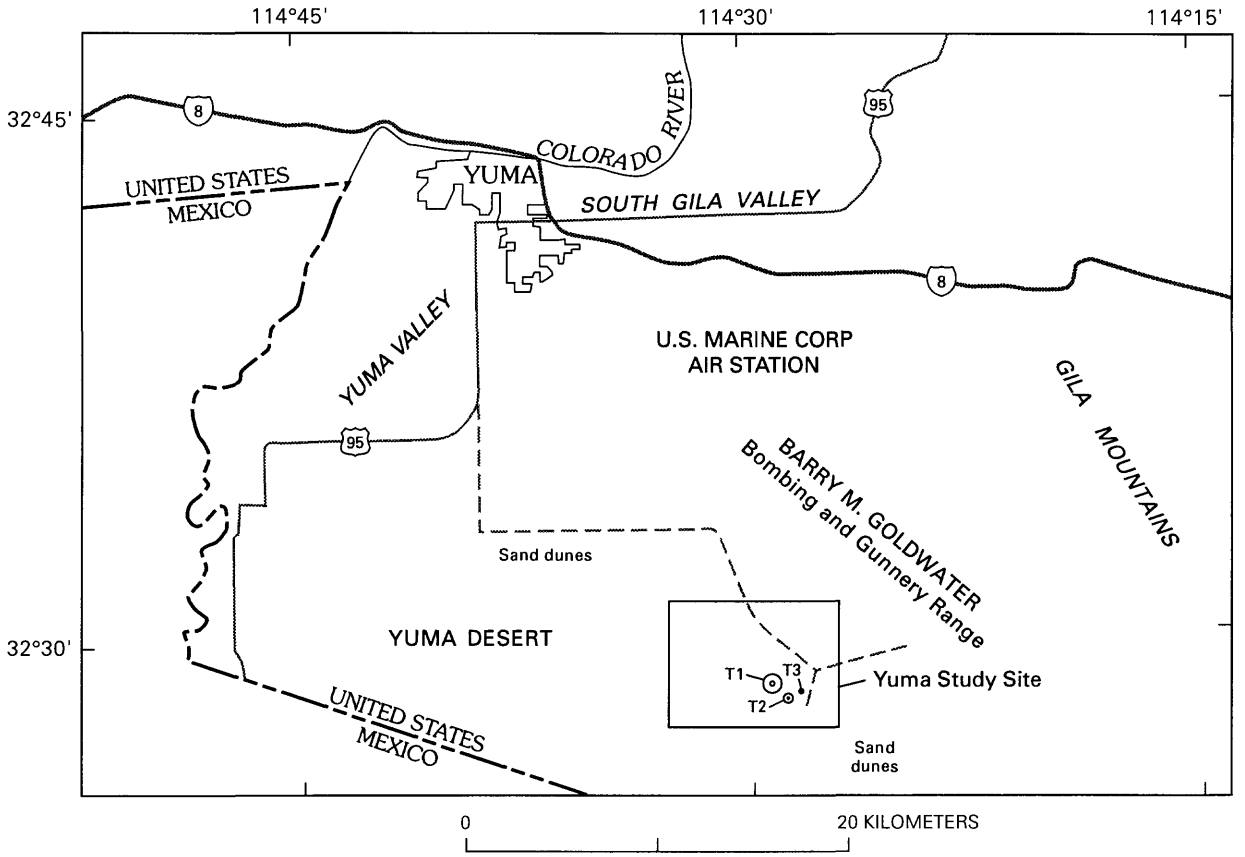
114°45'
114°30'
114°15'
32°45'
32°30'
8
95
COLORADO RIVER
YUMA
UNITED STATES
MEXICO
SOUTH GILA VALLEY
YUMA VALLEY
U.S. MARINE CORP
AIR STATION
GILA MOUNTAINS
BARRY M. GOLDWATER
Bombing and Gunnery Range
Sand dunes
YUMA DESERT
T1
T2
T3
Yuma Study Site
Sand
dunes
0
20 KILOMETERS

Figure 2

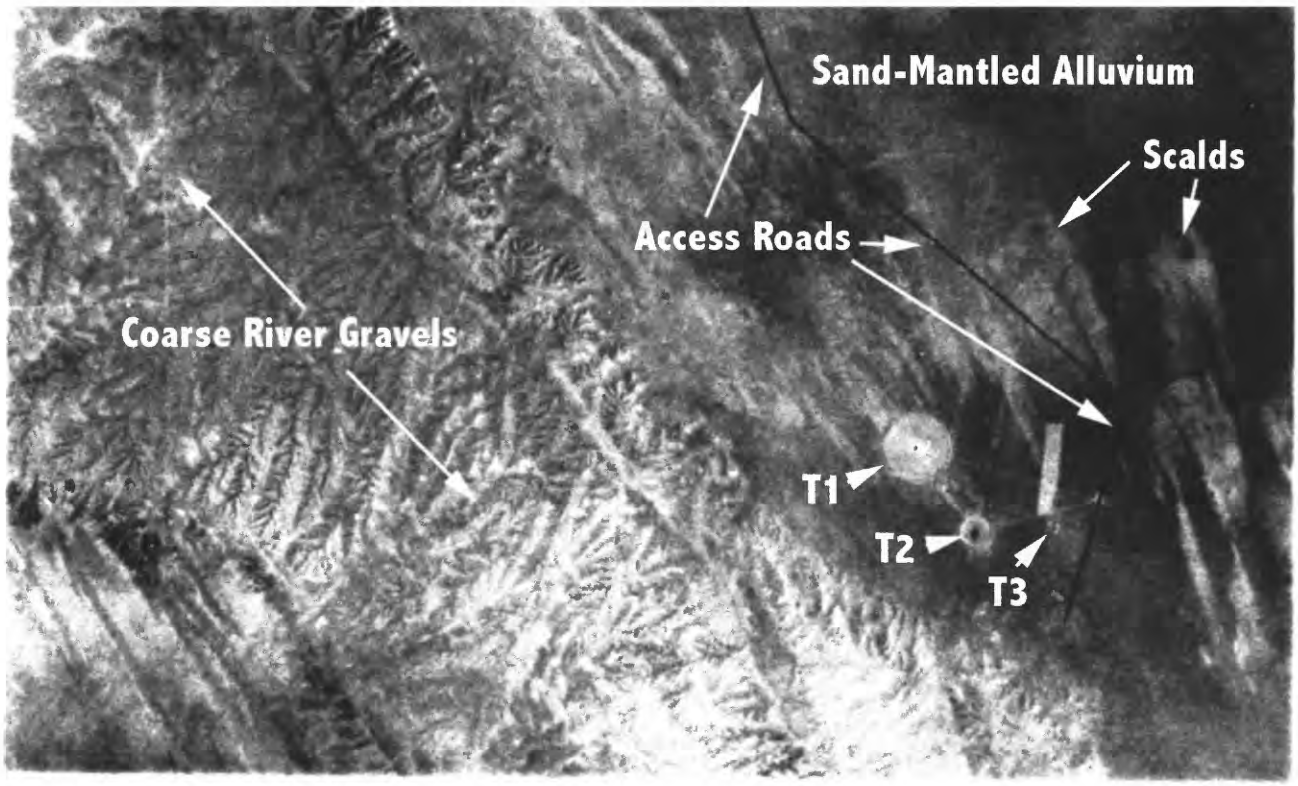
Sand-Mantled Alluvium
Scalds
Access Roads
Coarse River Gravels
T1
T2
T3

Figure 3

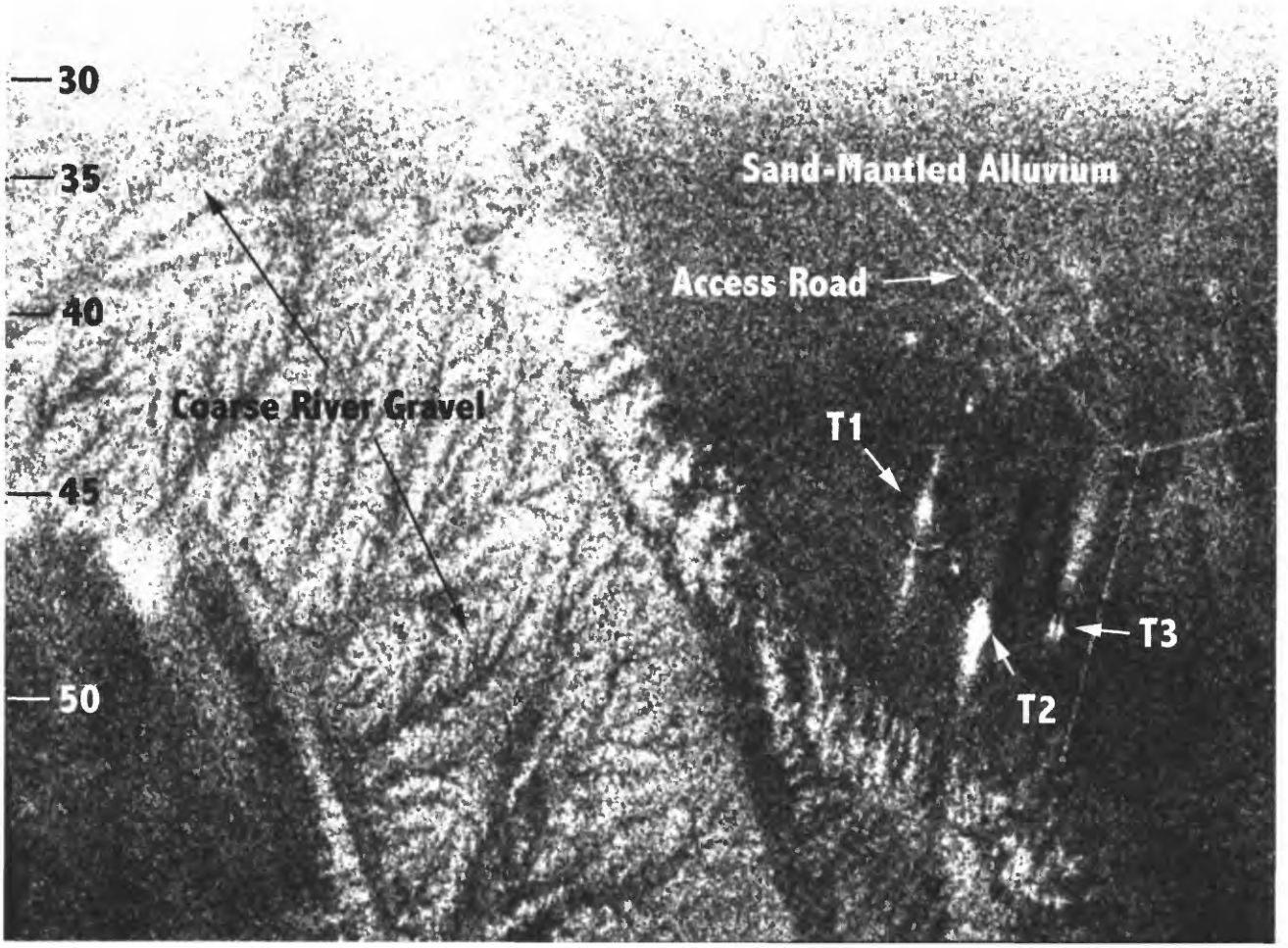
30
35
40
45
50
Sand-Mantled Alluvium
Access Road
Coarse River Gravel
T1
T2
T3

Figure 4a

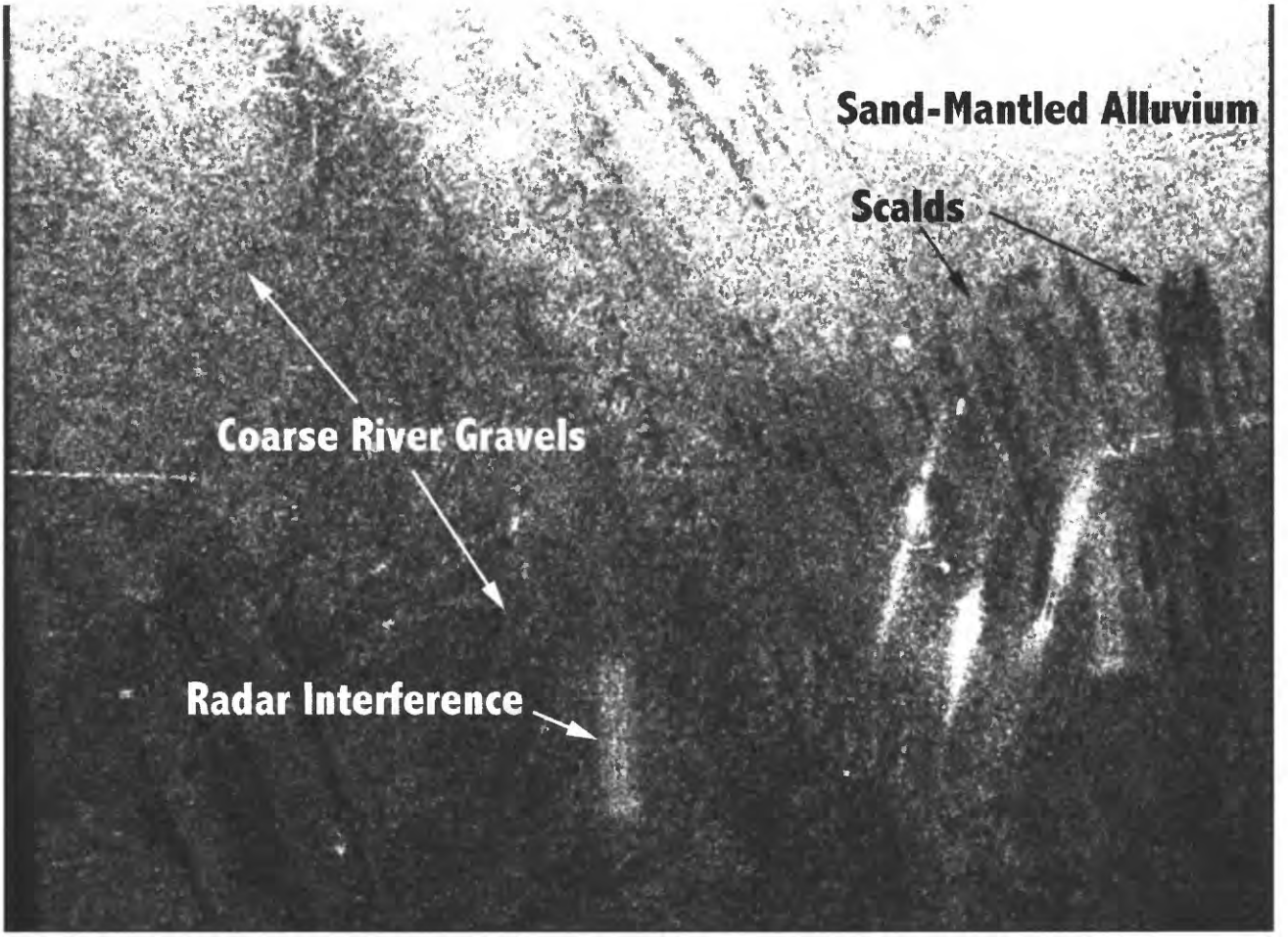
Sand-Mantled Alluvium
Scalds
Coarse River Gravels
Radar Interference

Figure 4b

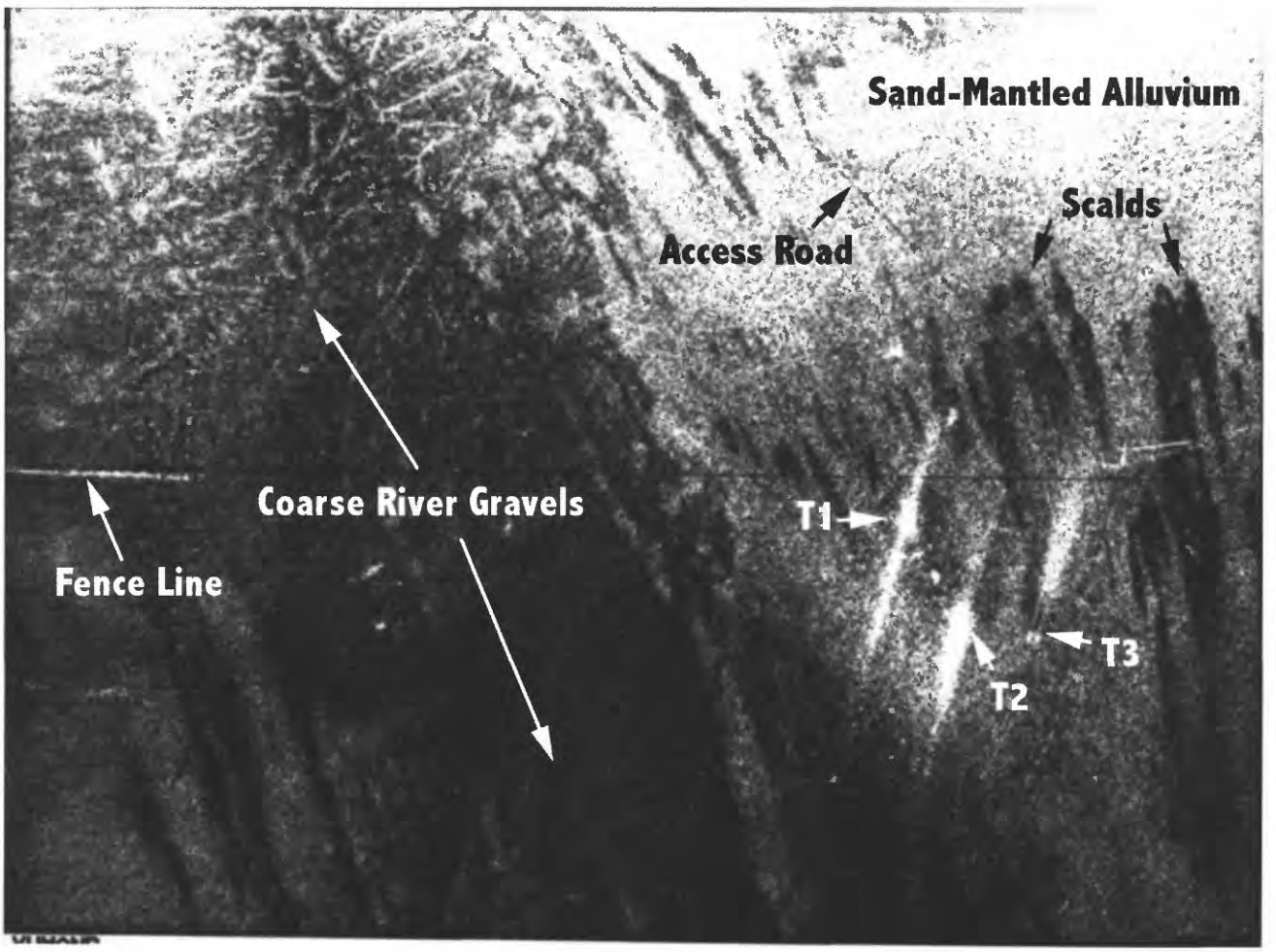
Sand-Mantled Alluvium
Access Road
Scalds
Coarse River Gravels
T1
Fence Line
T3
T2

Figure 4c

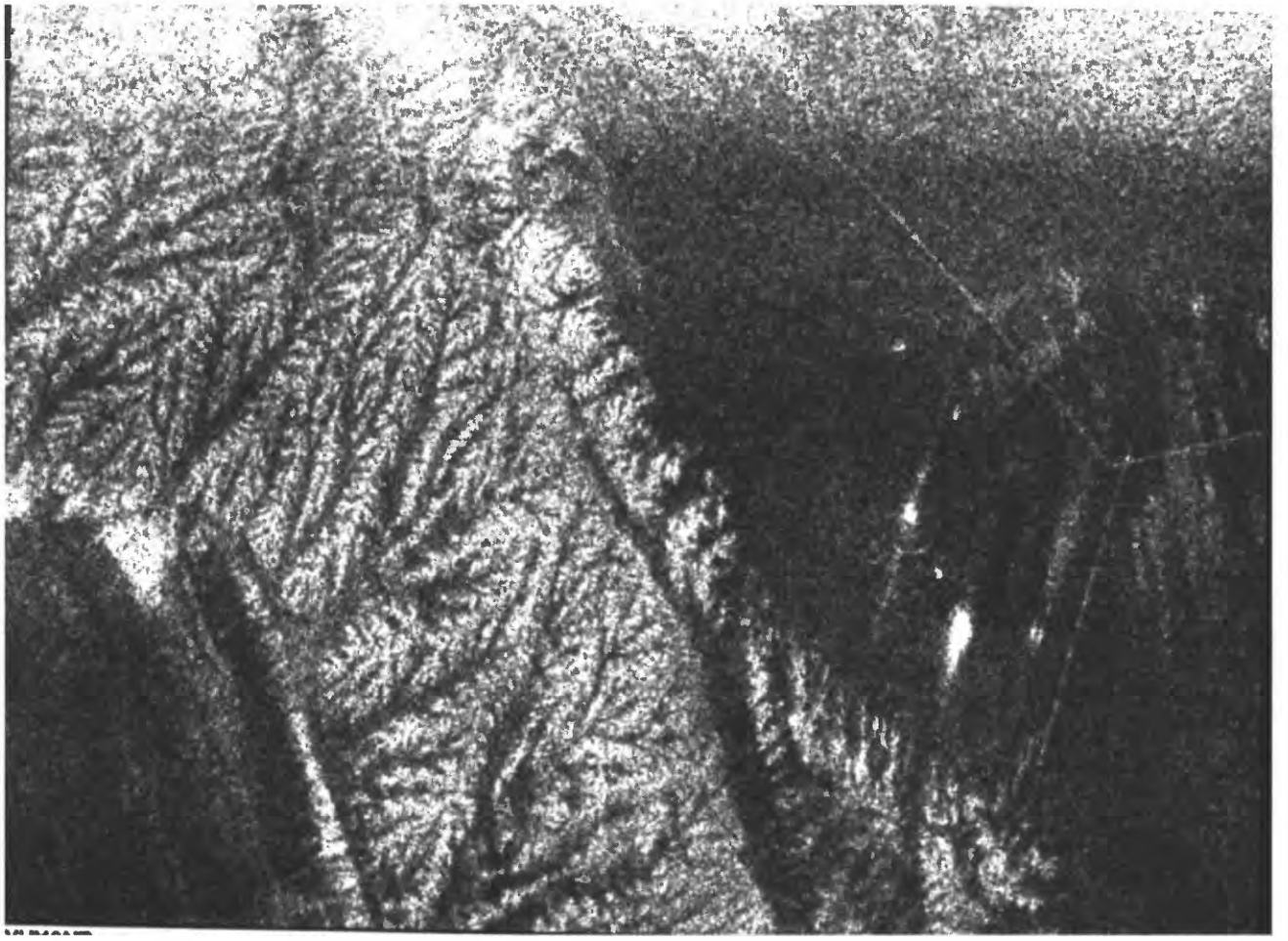

Figure 4d

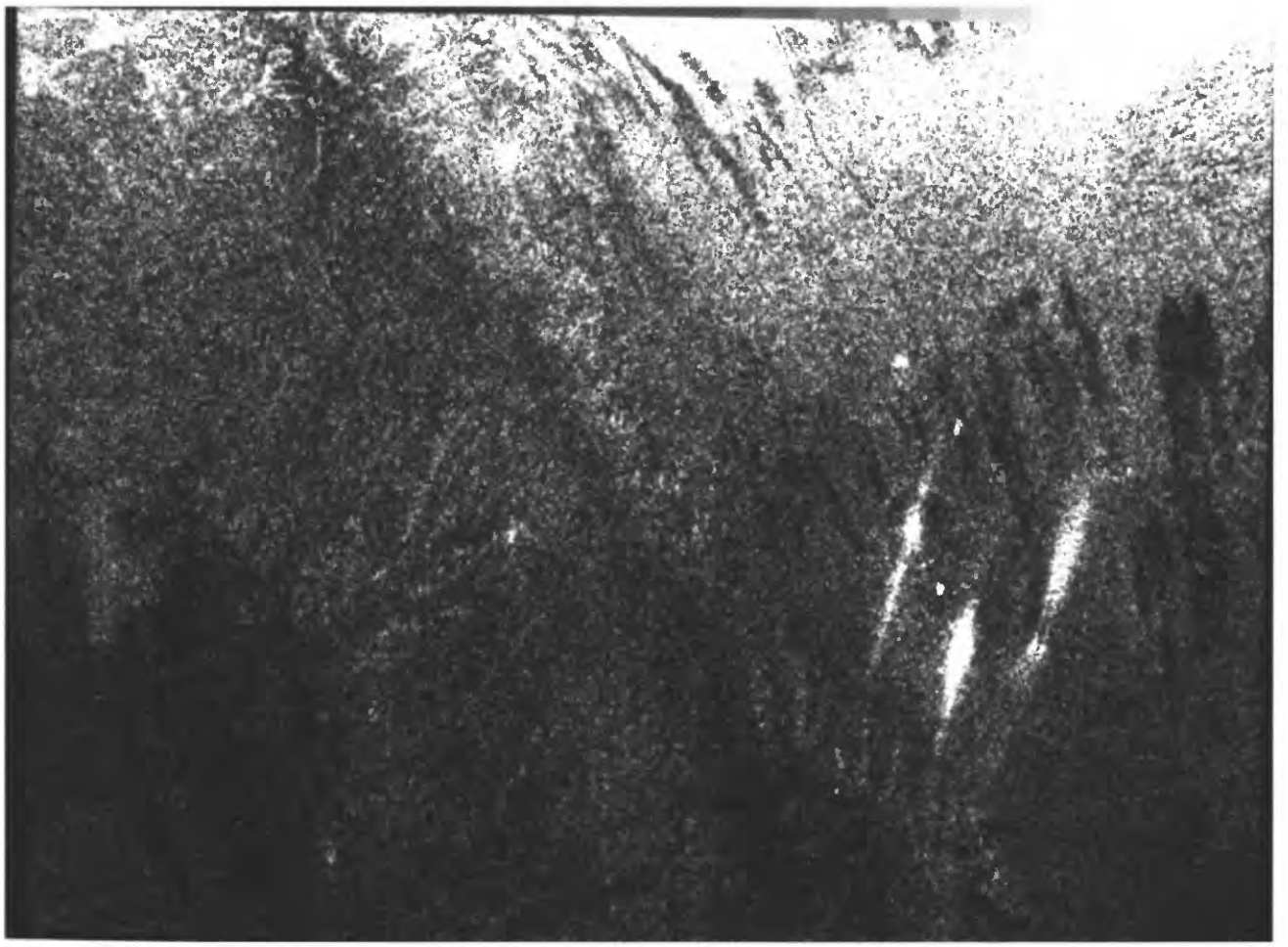

Figure 4e

Figure 4f

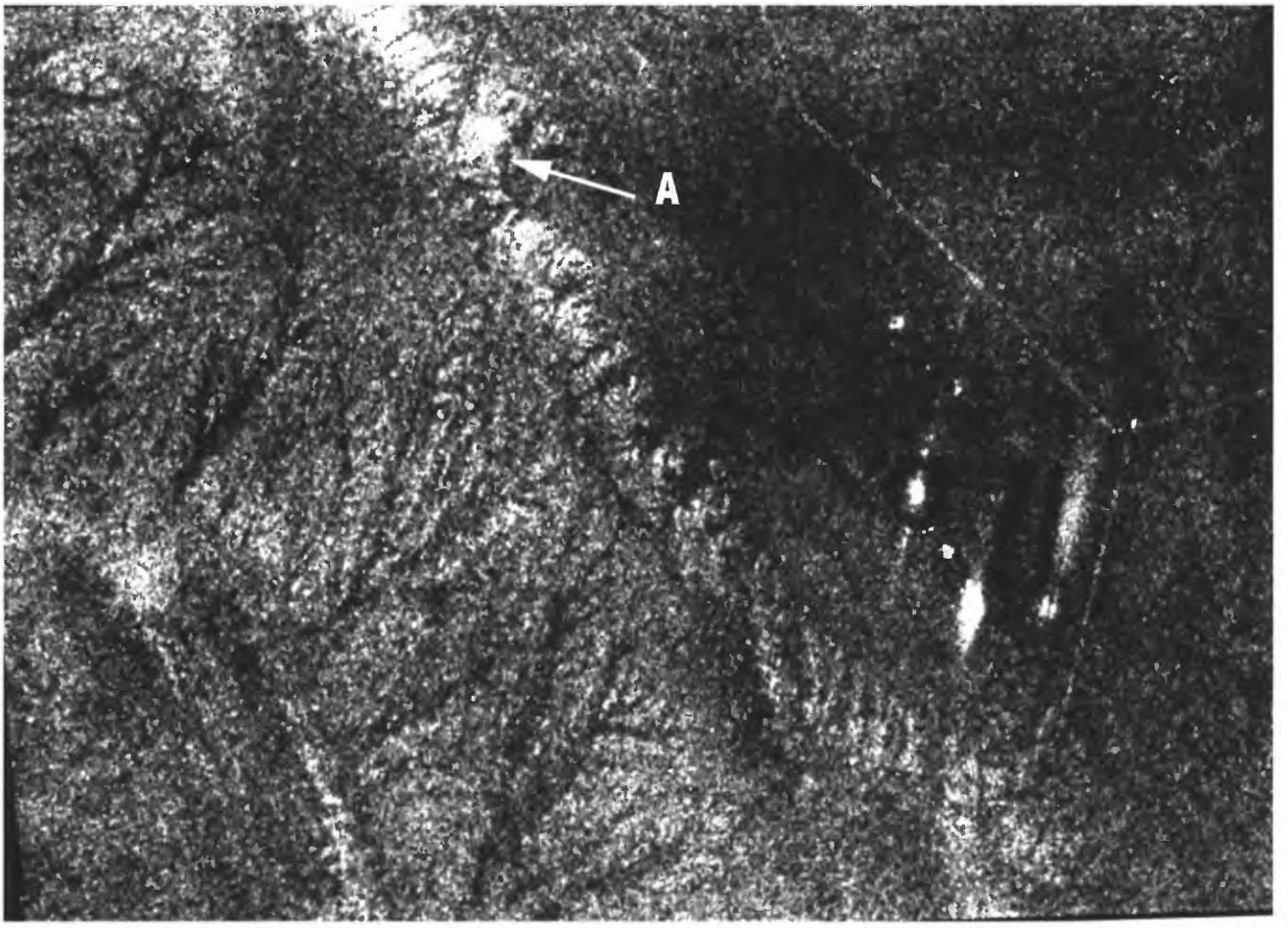

Figure 4g

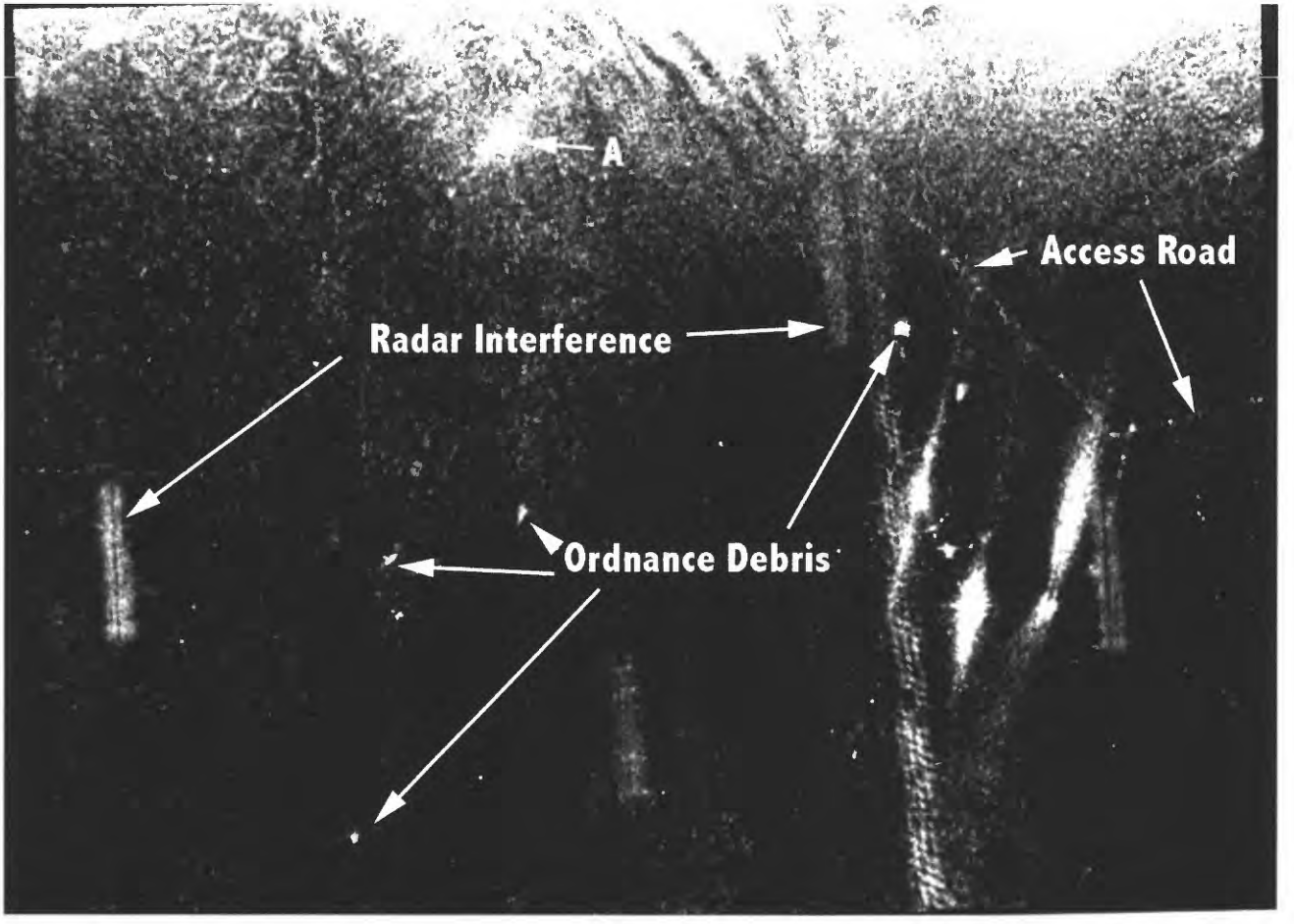

Figure 4h

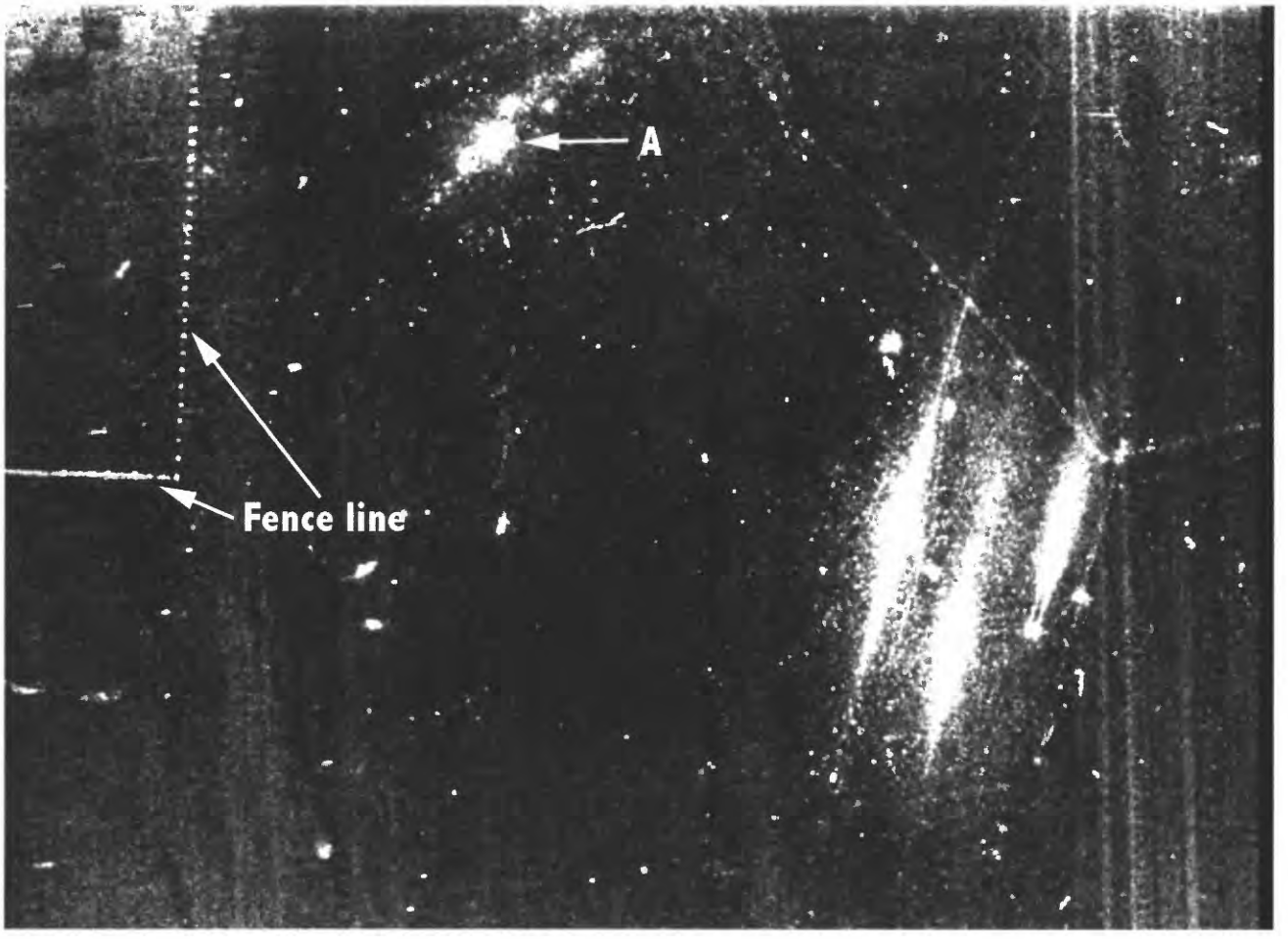

Figure 4i

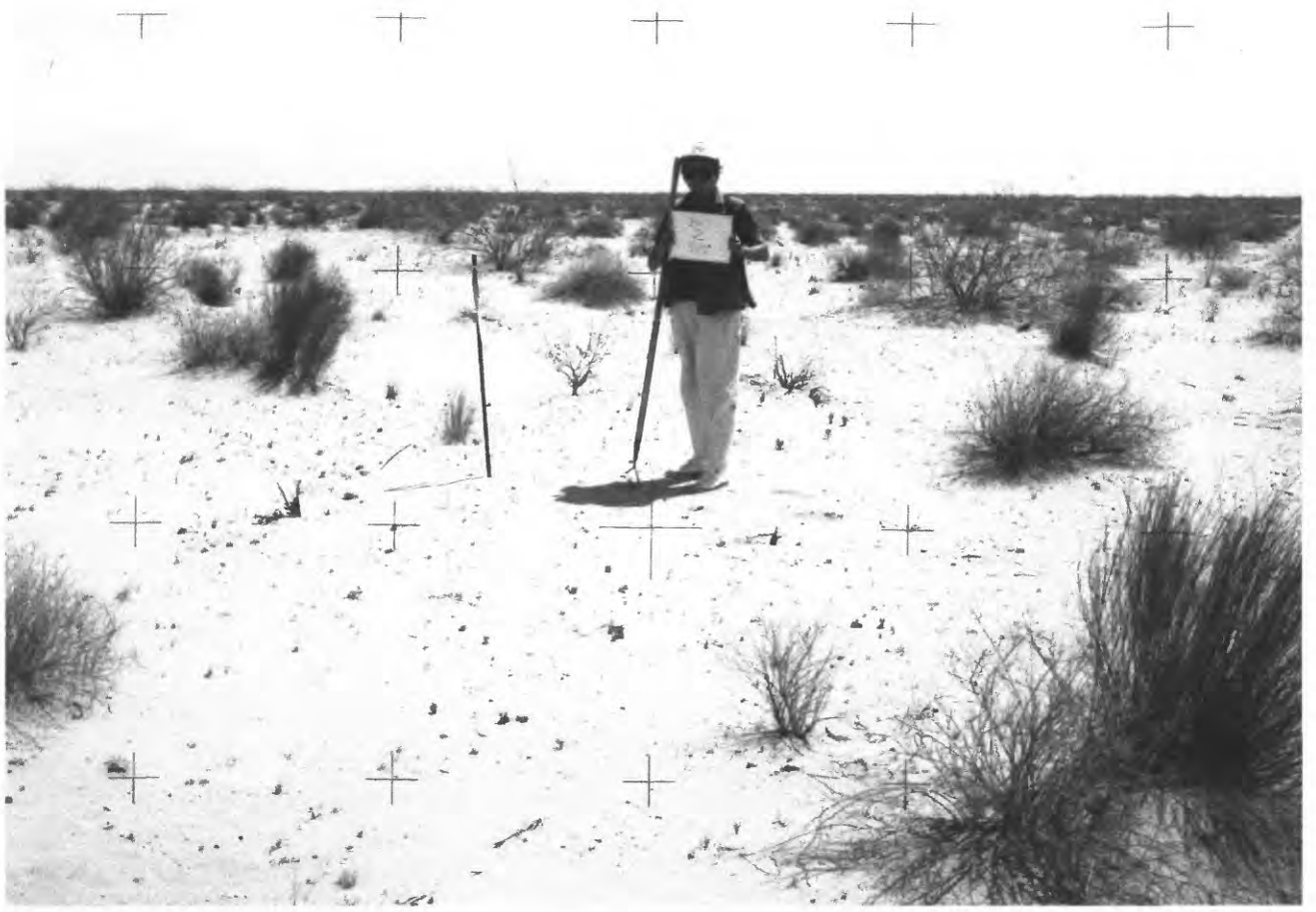

Figure 5a

Figure 5b

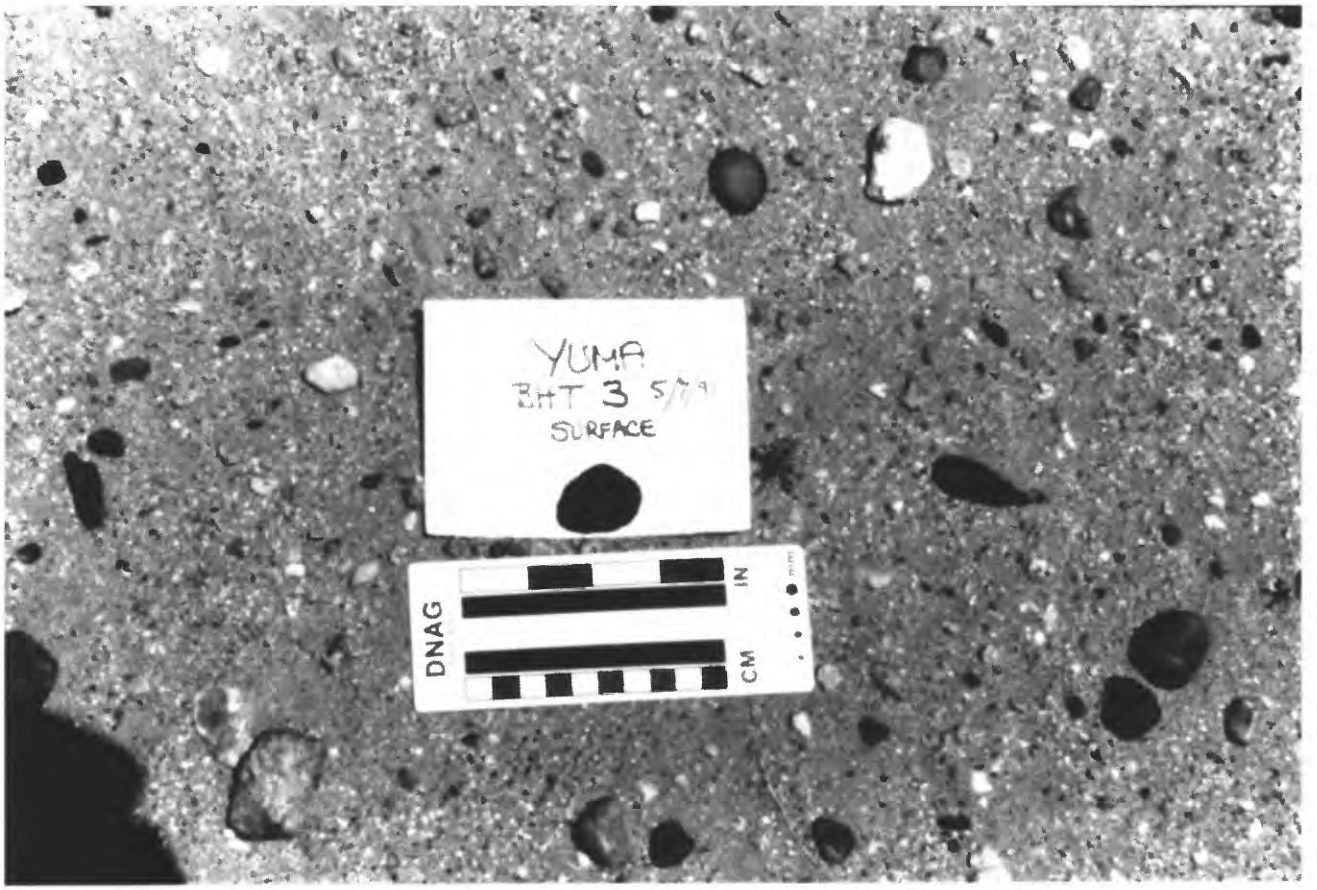

Figure 5c

Figure 5d

Figure 6a

Figure 6b

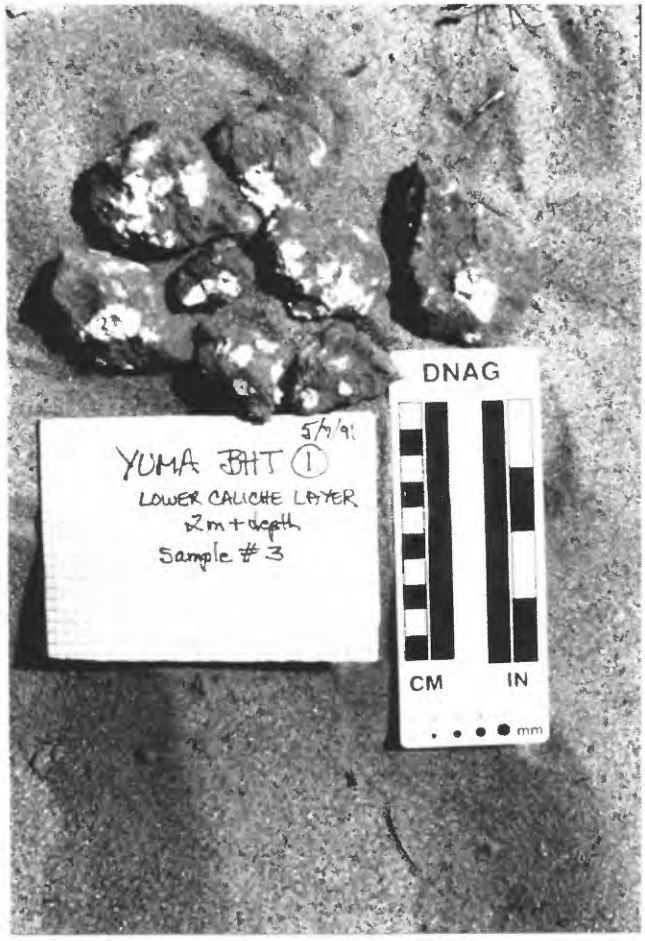
DNAG
5/9/91
YUMA BHT (1)
LOWER CALICHE LAYER
2m + depth
Sample # 3
CM
IN
mm

Figure 6c

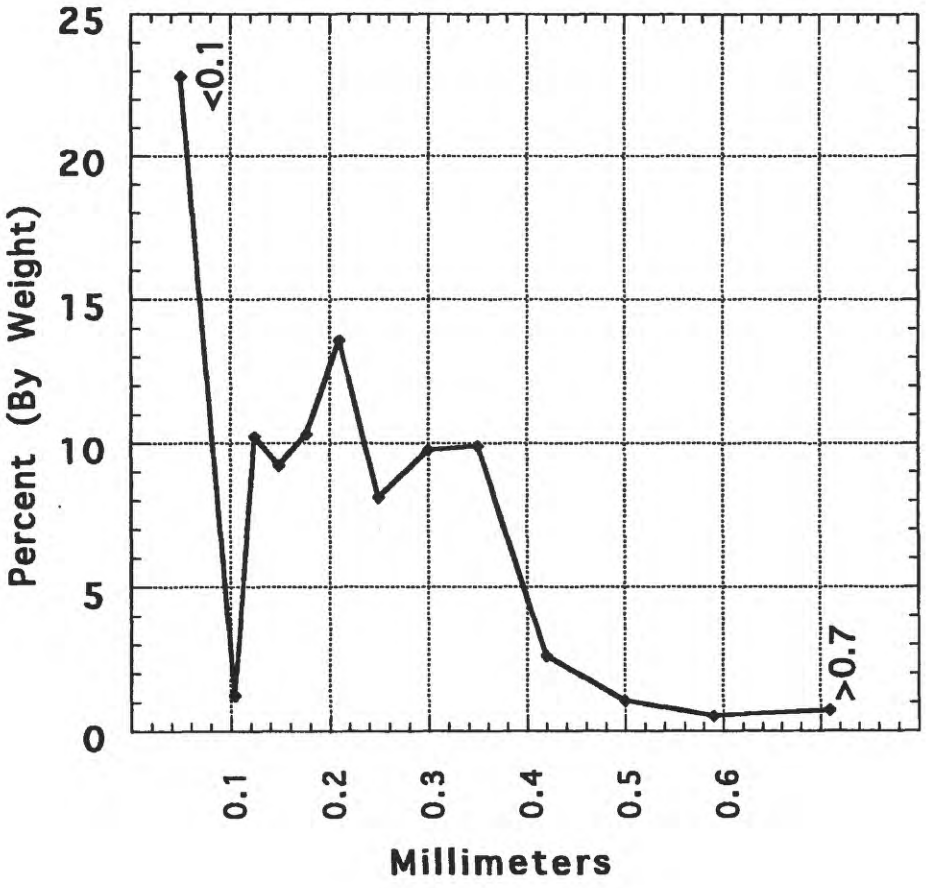
25
20
15
10
5
0
Percent (By Weight)
<0.1
>0.7
0.1
0.2
0.3
0.4
0.5
0.6
Millimeters

Figure 7a

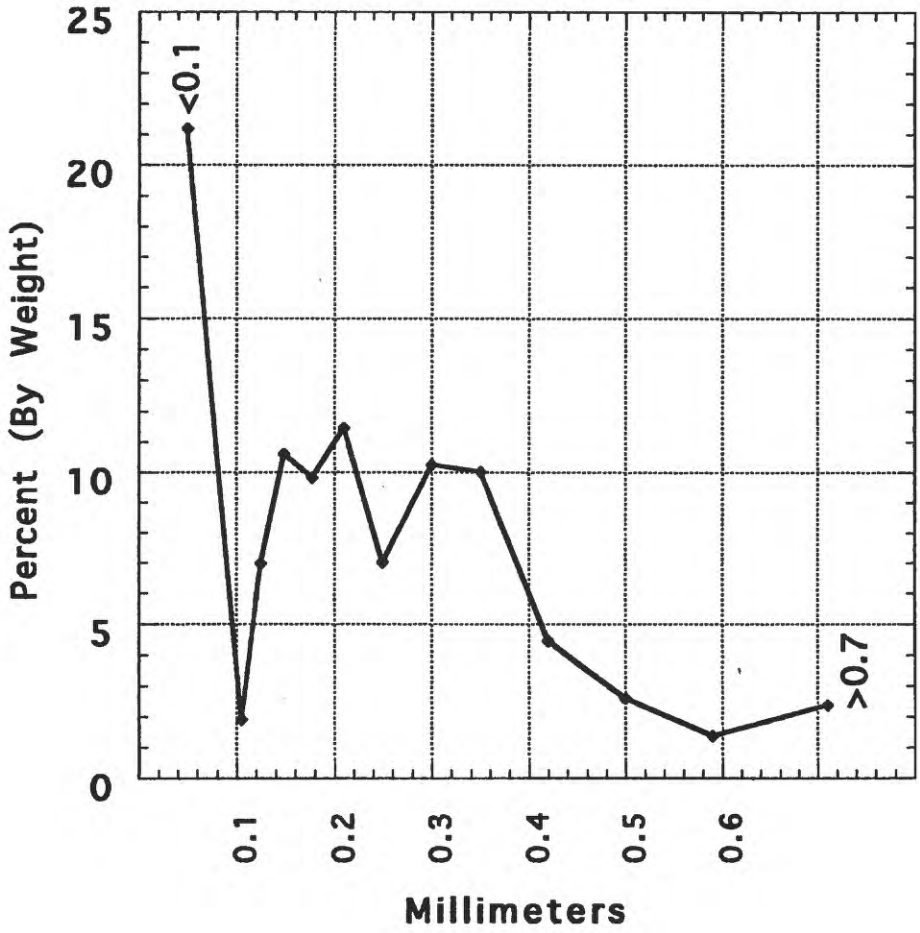
25
20
15
10
5
0
Percent (By Weight)
<0.1
>0.7
0.1
0.2
0.3
0.4
0.5
0.6
Millimeters

Figure 7b

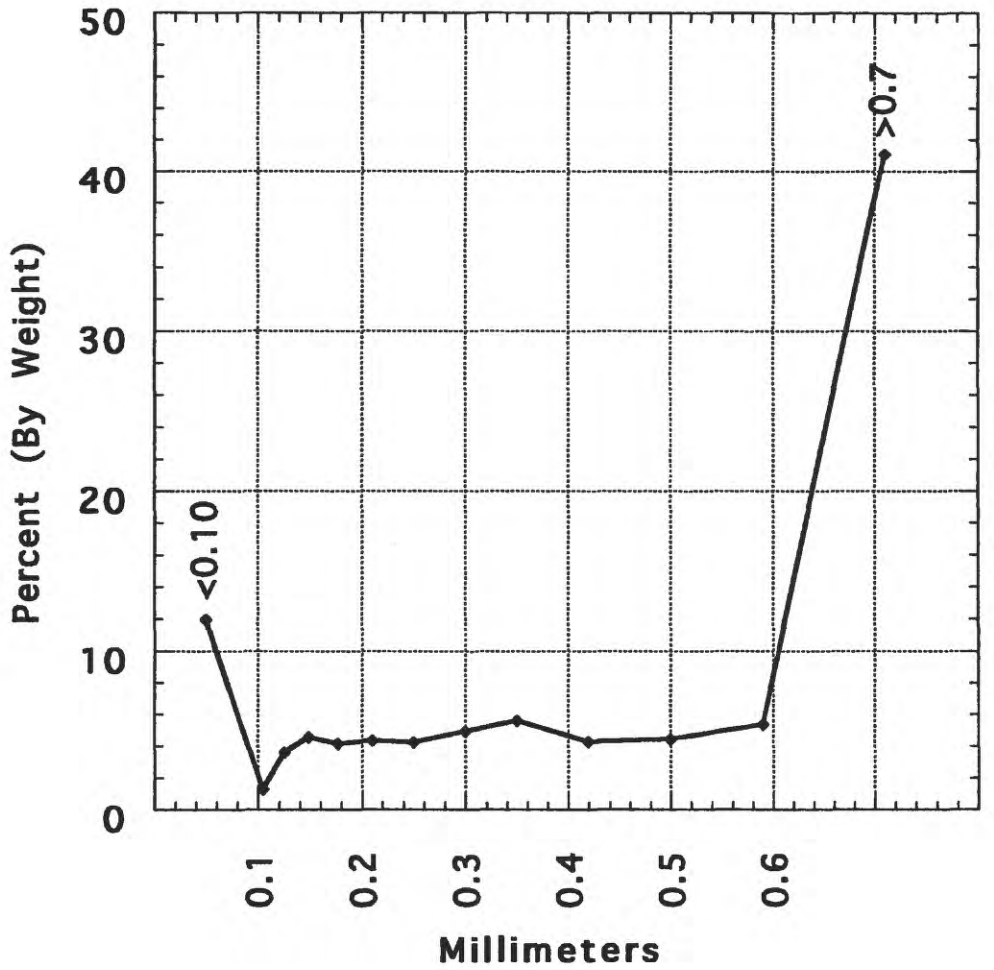
50
40
30
20
10
0
Percent (By Weight)
<0.10
>0.7
0.1
0.2
0.3
0.4
0.5
0.6
Millimeters

Figure 7c

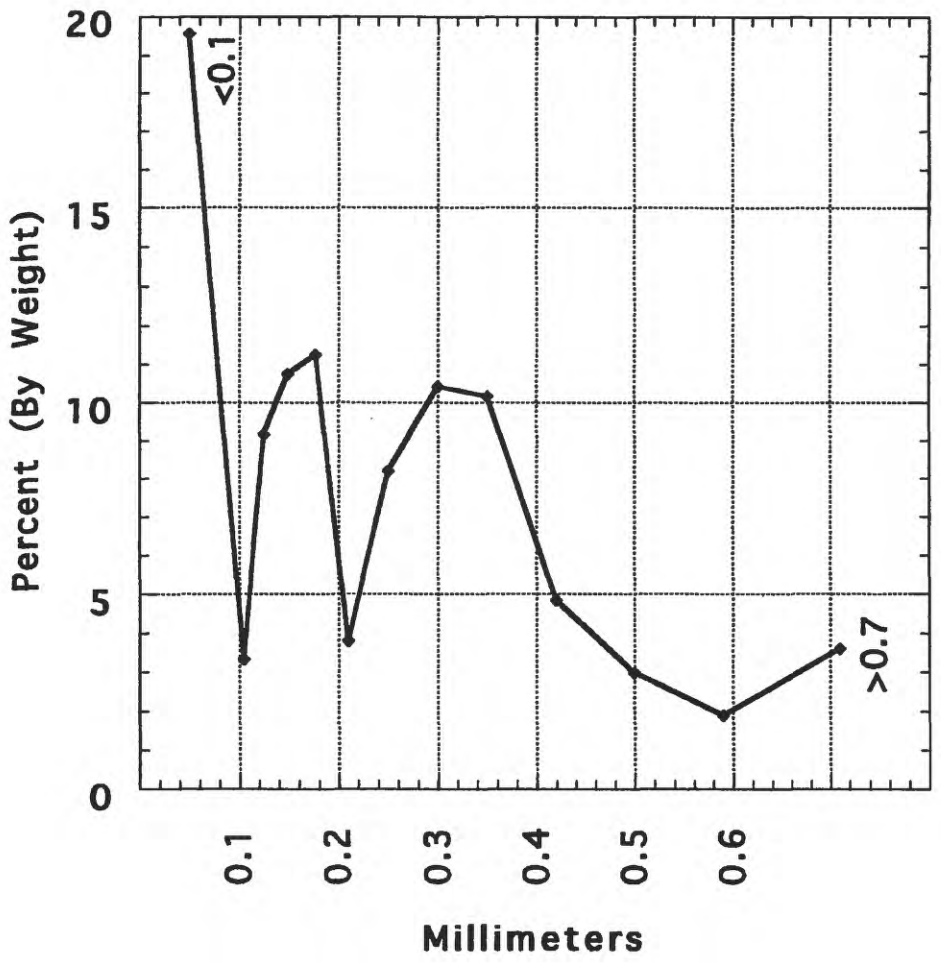
20
15
10
5
0
Percent (By Weight)
<0.1
>0.7
0.1
0.2
0.3
0.4
0.5
0.6
Millimeters

Figure 7d

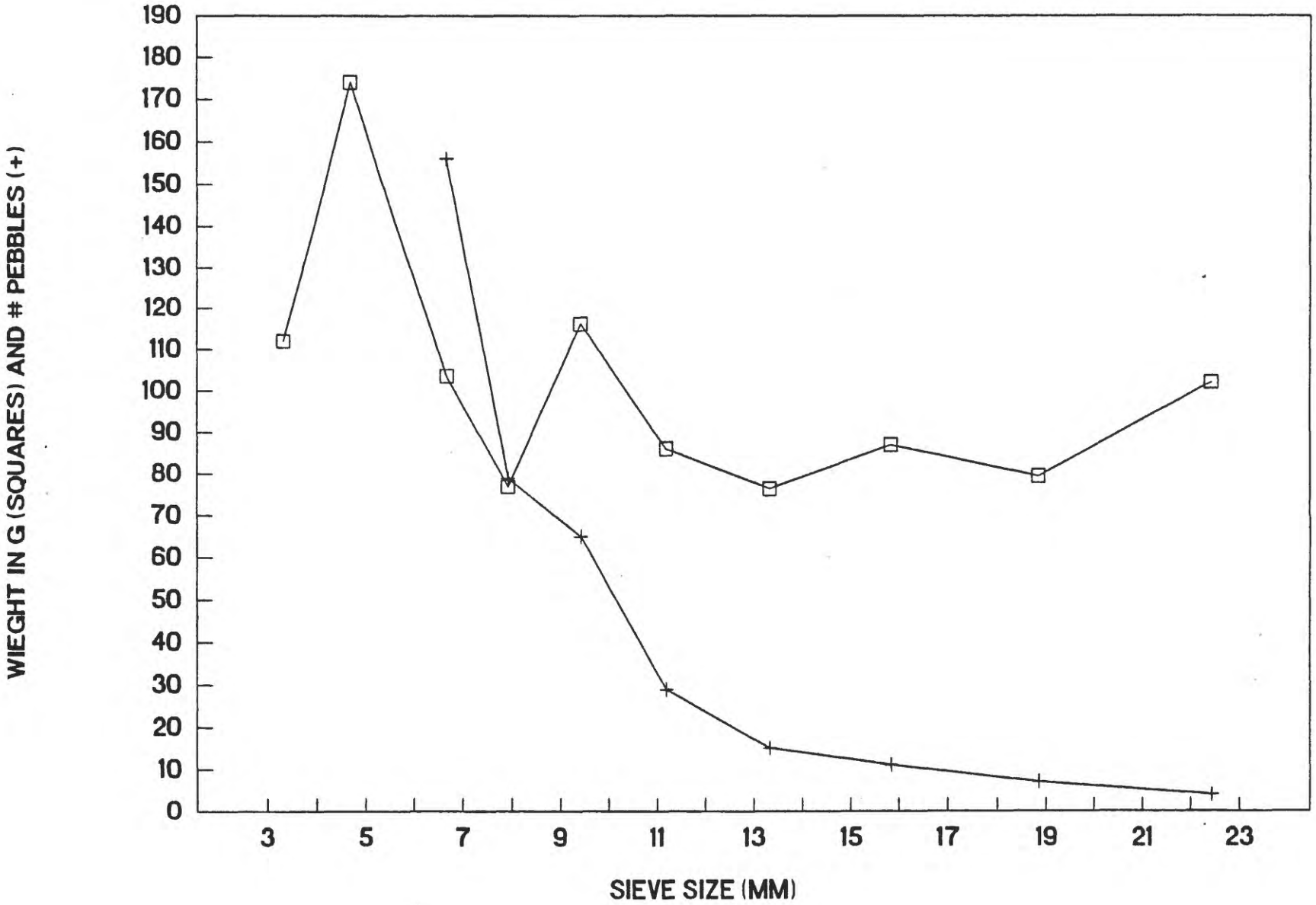
WIEGHT IN G (SQUARES) AND # PEBBLES (+)
190
180
170
160
150
140
130
120
110
100
90
80
70
60
50
40
30
20
10
0
3
5
7
9
11
13
15
17
19
21
23
SIEVE SIZE (MM)

Figure 8

Figure 9a

Figure 9b

Figure 10a

Figure 10b

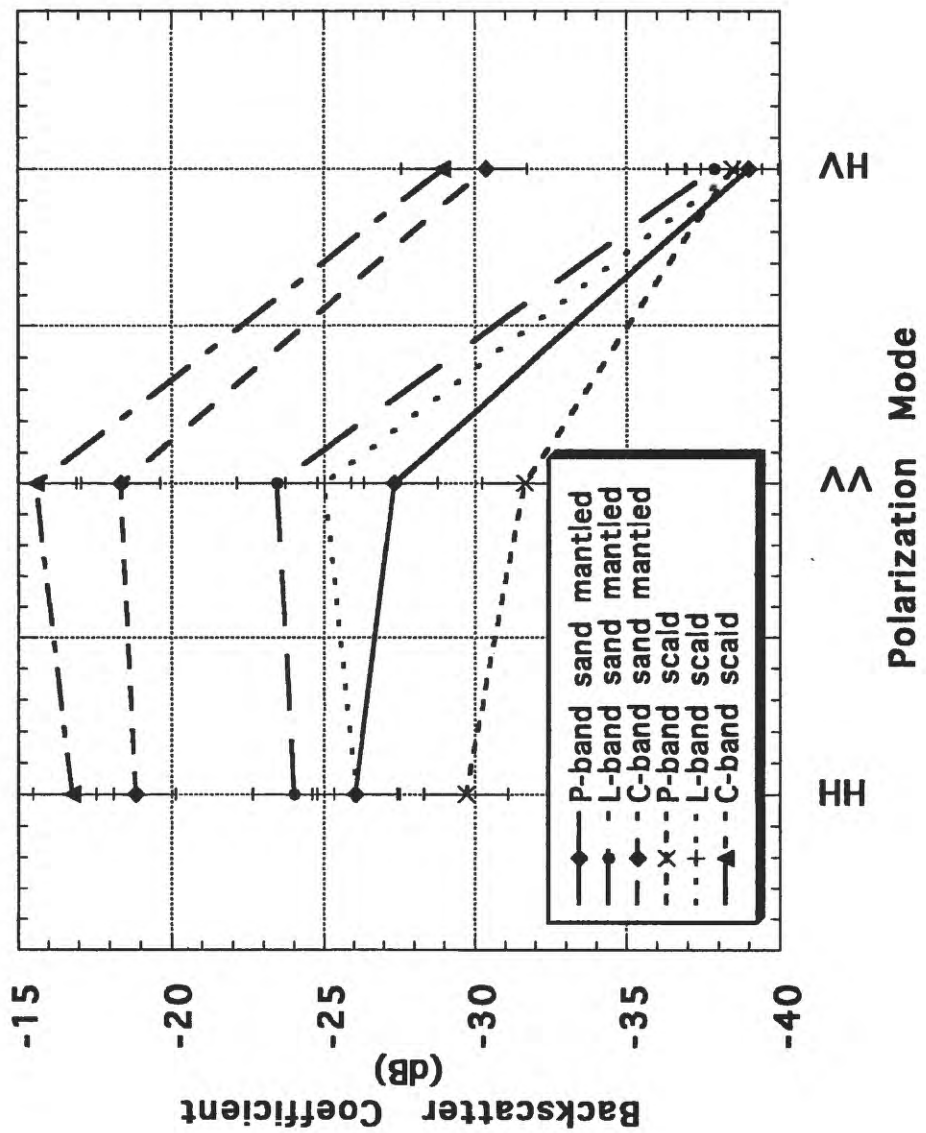
Backscatter Coefficient (dB)
-15
-20
-25
-30
-35
-40
HH
VV
HV
Polarization Mode
P-band sand mantled
L-band sand mantled
C-band sand mantled
P-band scald
L-band scald
C-band scald

Figure 11a

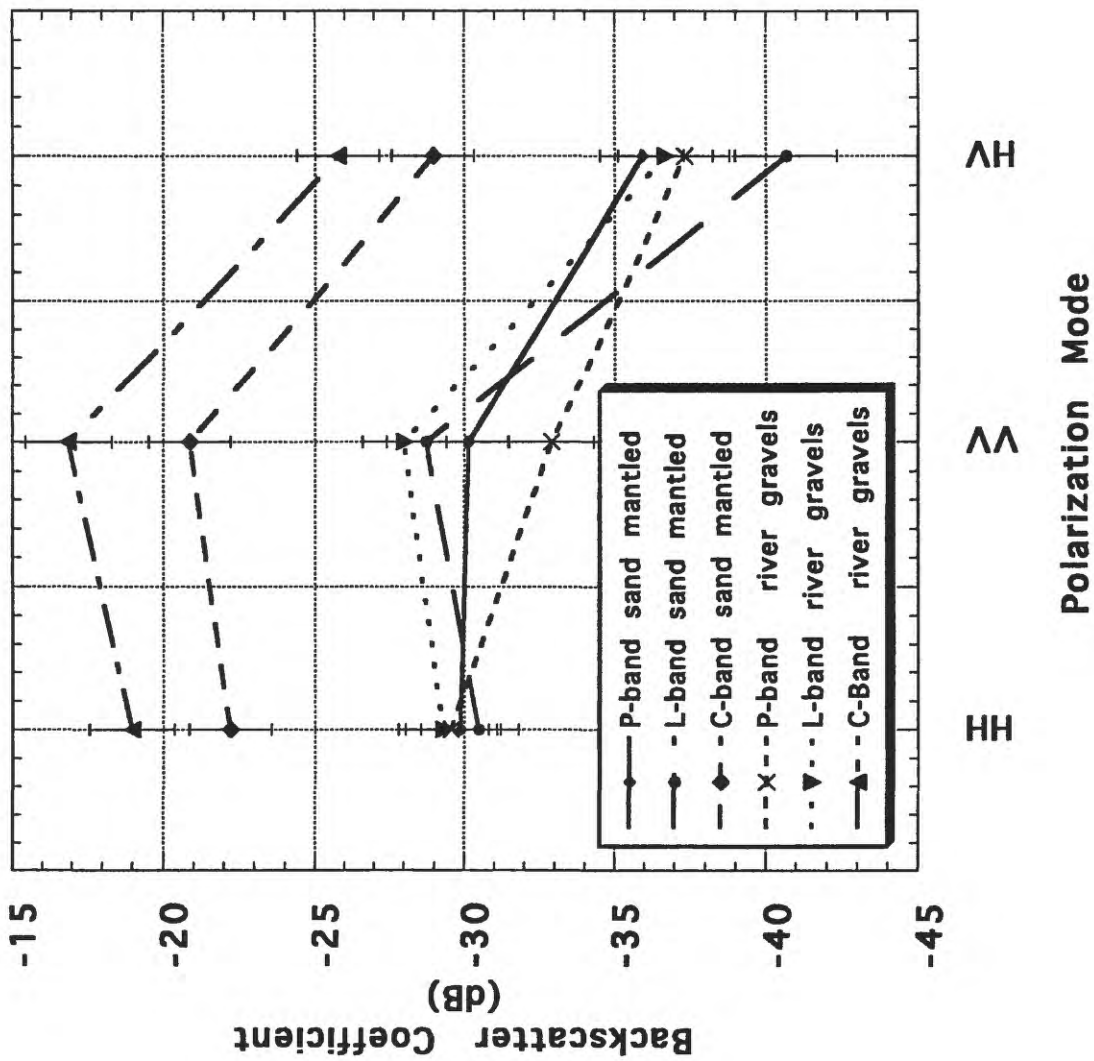
Backscatter Coefficient (dB)
-15
-20
-25
-30
-35
-40
-45
HH
VV
HV
Polarization Mode
P-band sand mantled
L-band sand mantled
C-band sand mantled
P-band river gravels
L-band river gravels
C-Band river gravels

Figure 11b

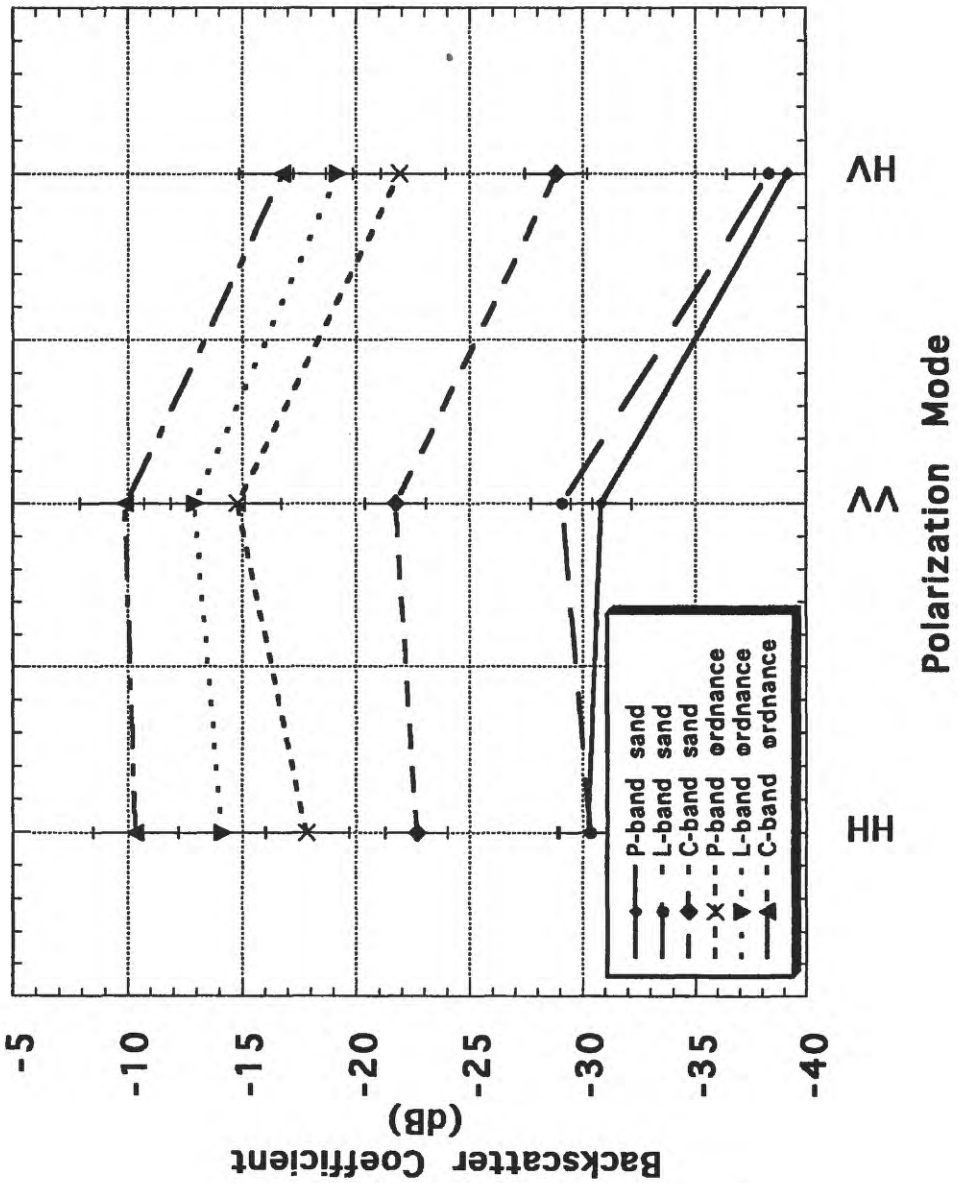
Backscatter Coefficient
(dB)
-5
-10
-15
-20
-25
-30
-35
-40
HH
VV
HV
Polarization Mode
P-band sand
L-band sand
C-band sand
P-band ordnance
L-band ordnance
C-band ordnance

Figure 11c

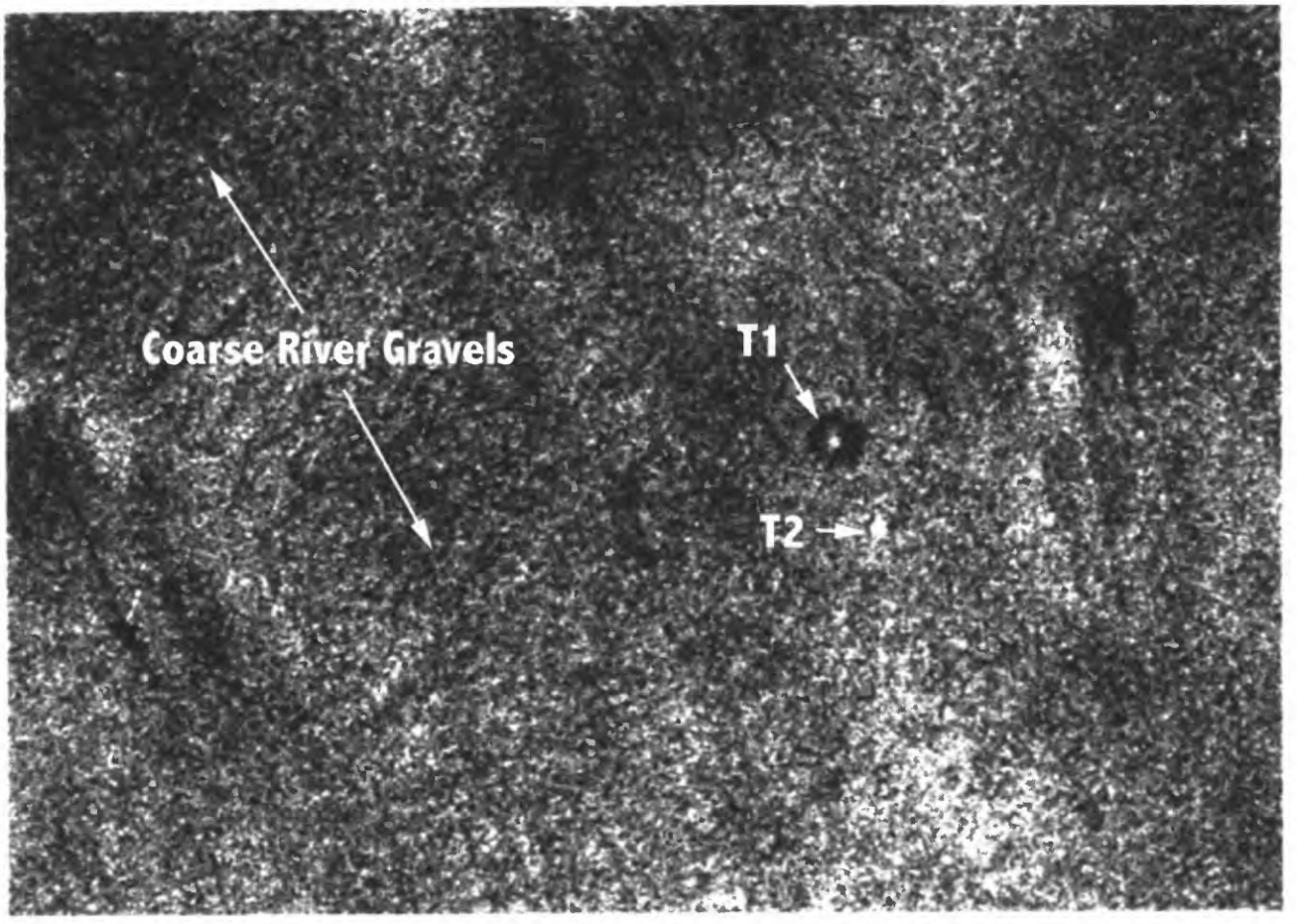

Figure 12

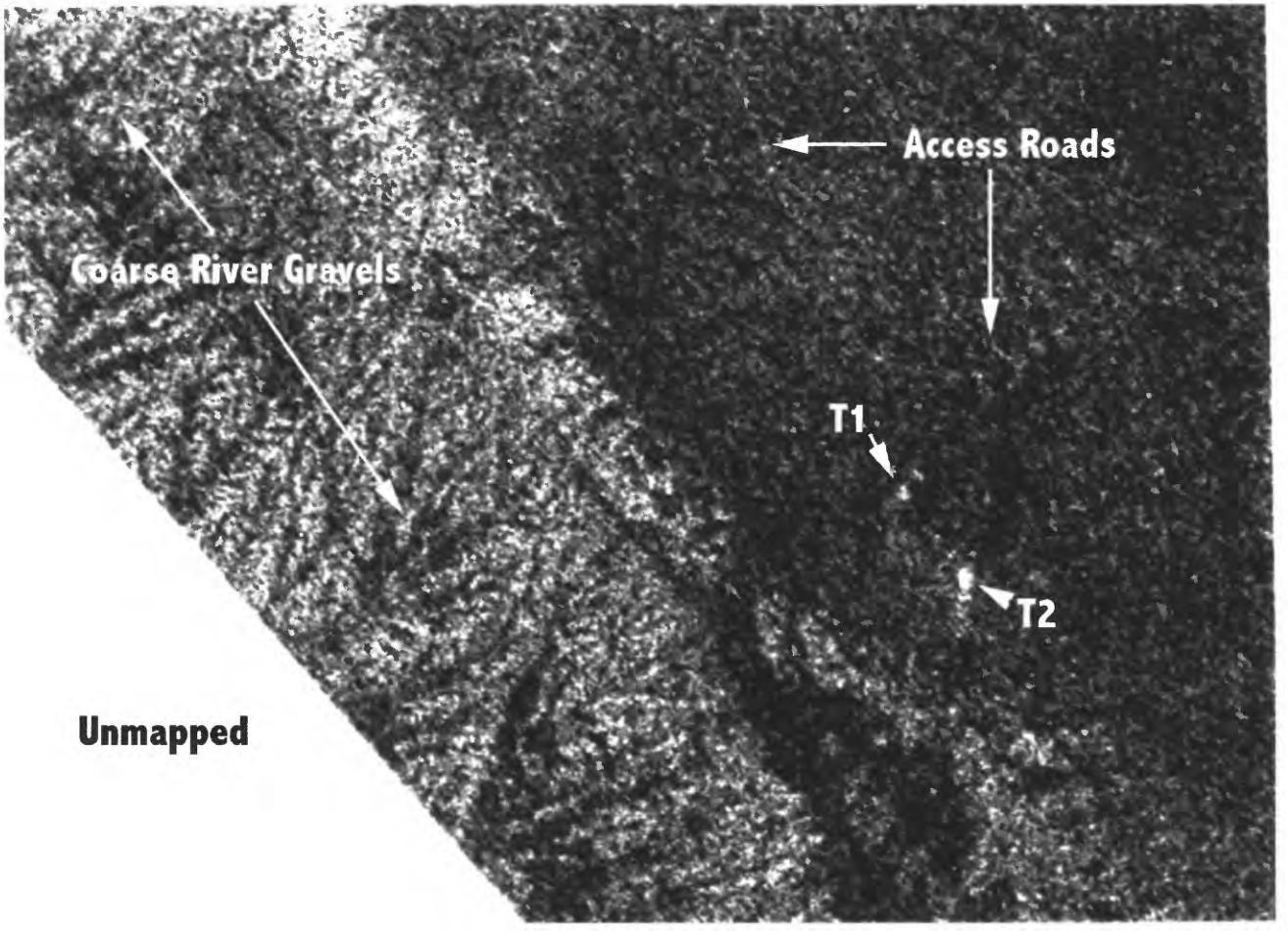

Figure 13a

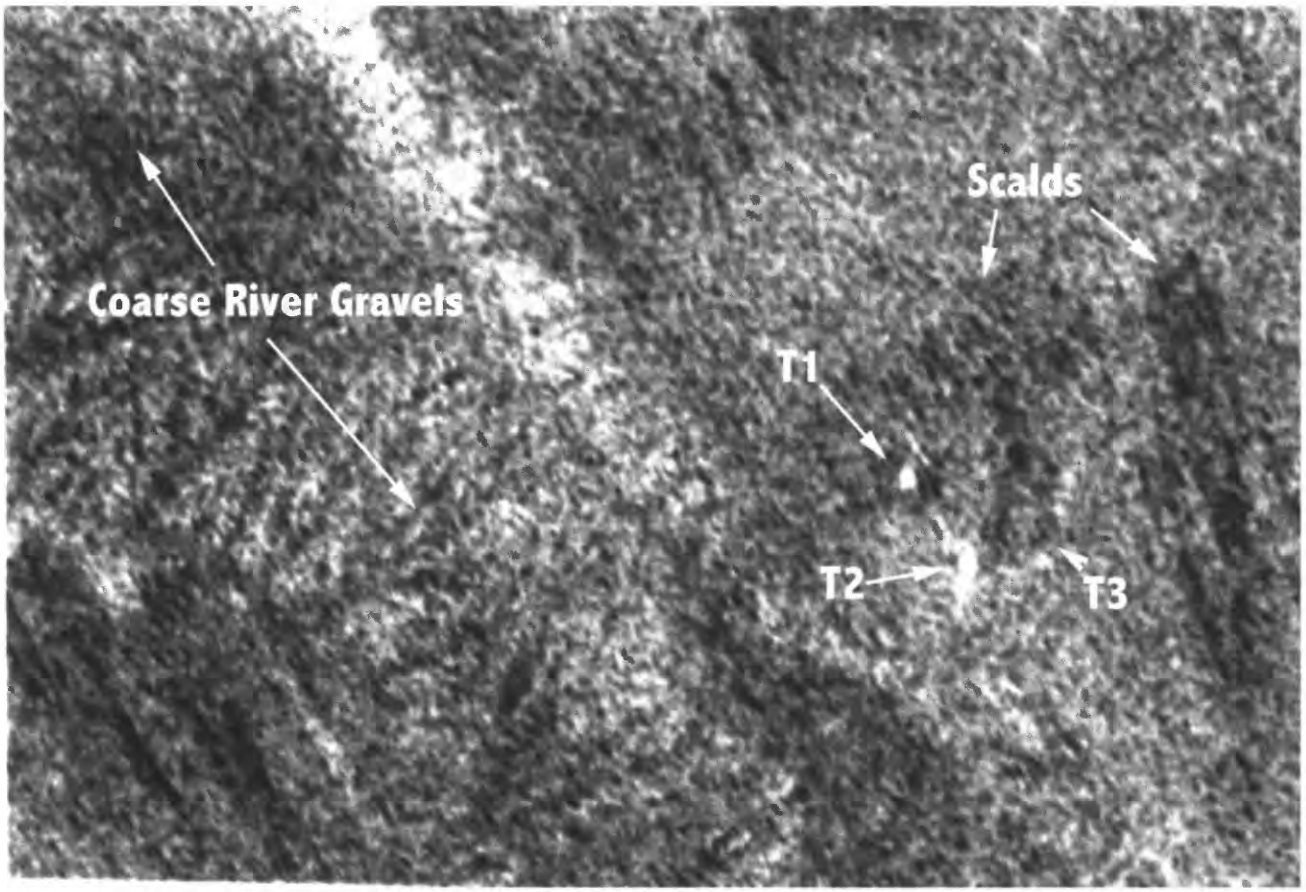

Figure 13b

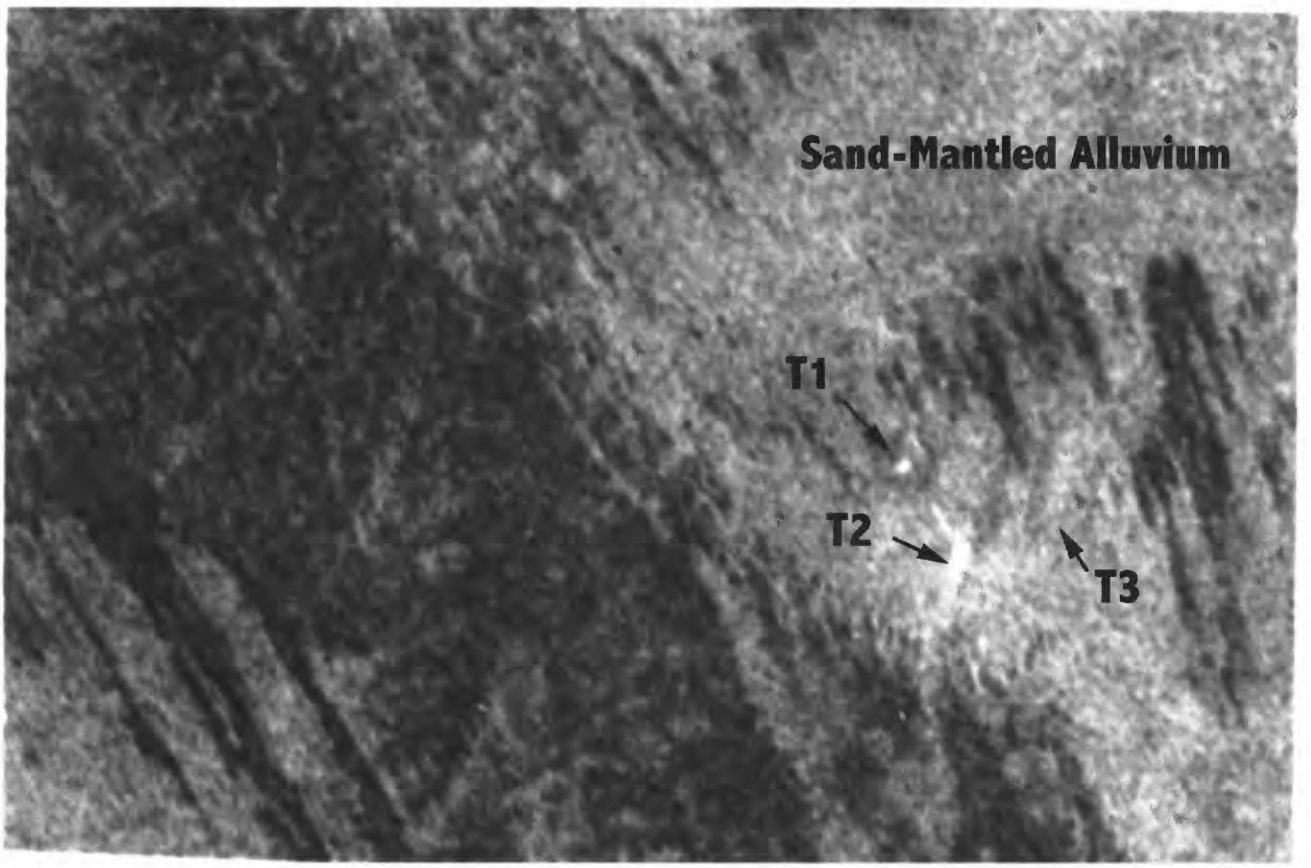

Figure 13c

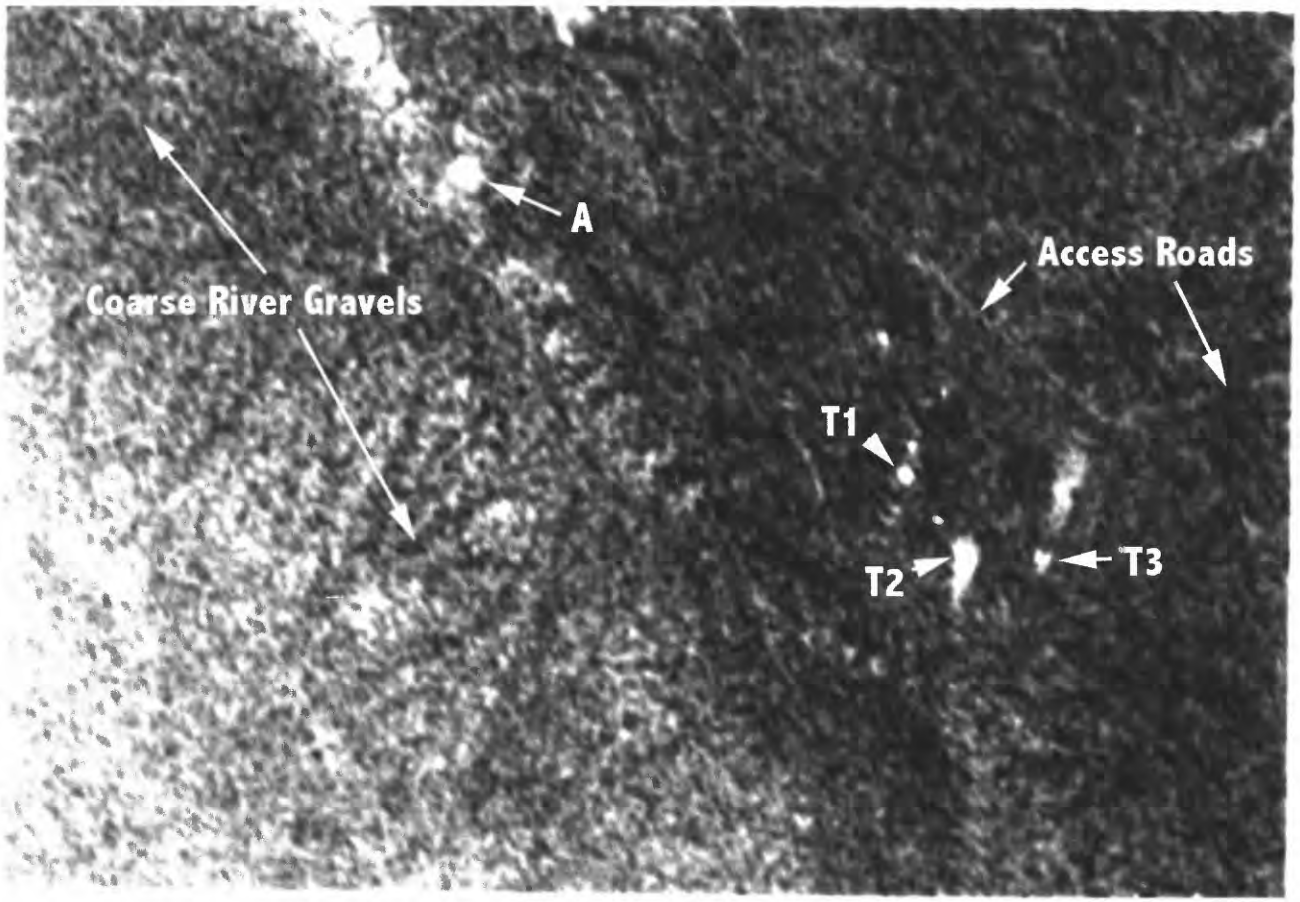

Figure 13d

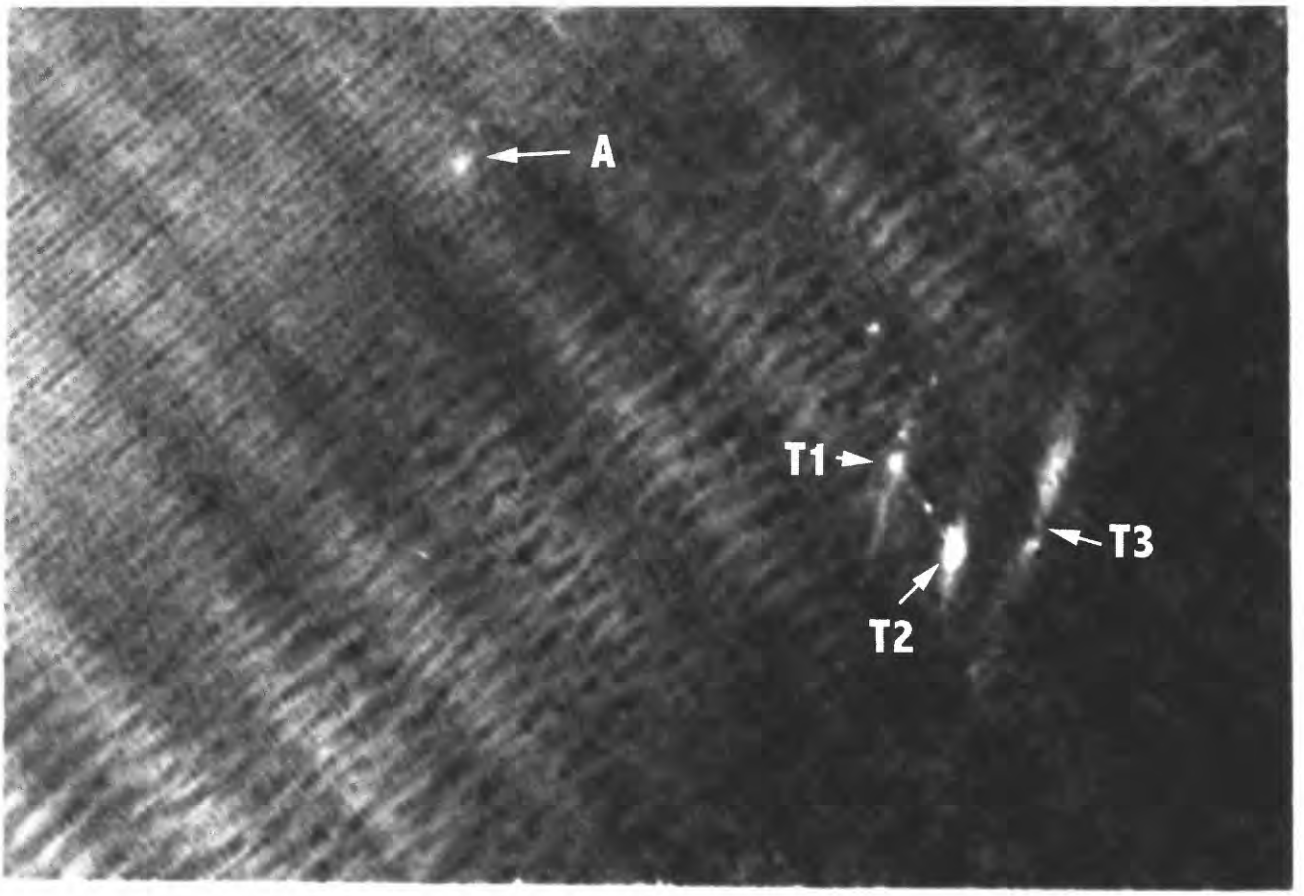

Figure 13e

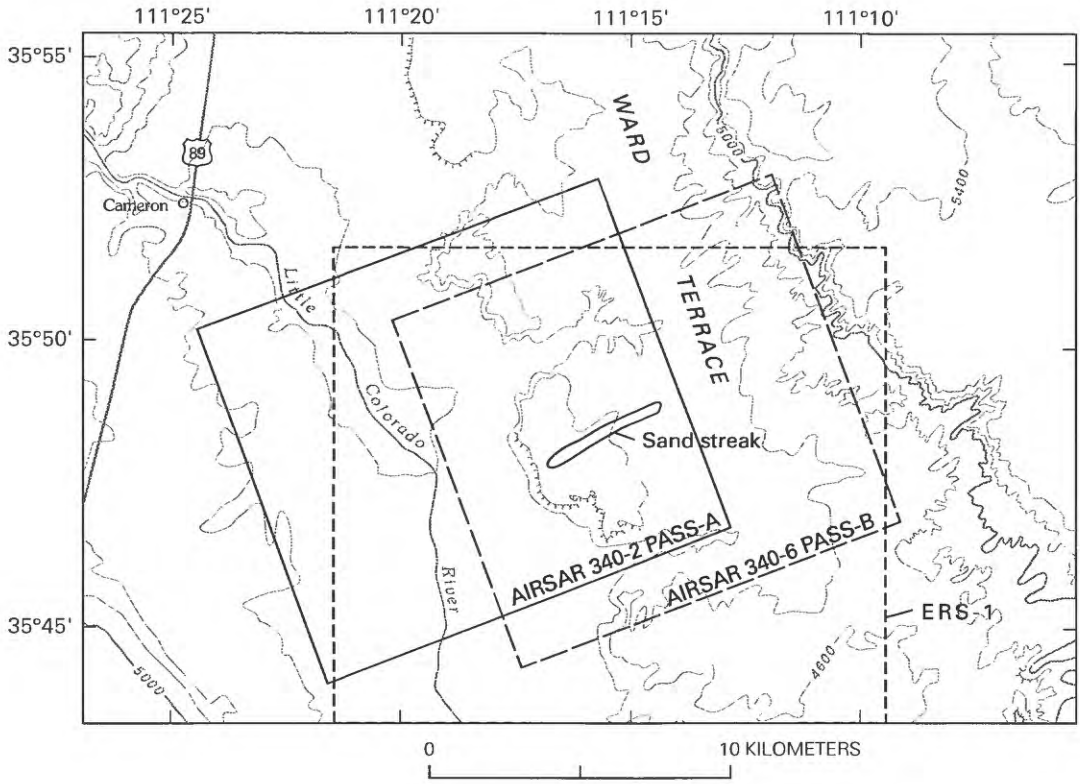

Figure 14

Schaber and Breed

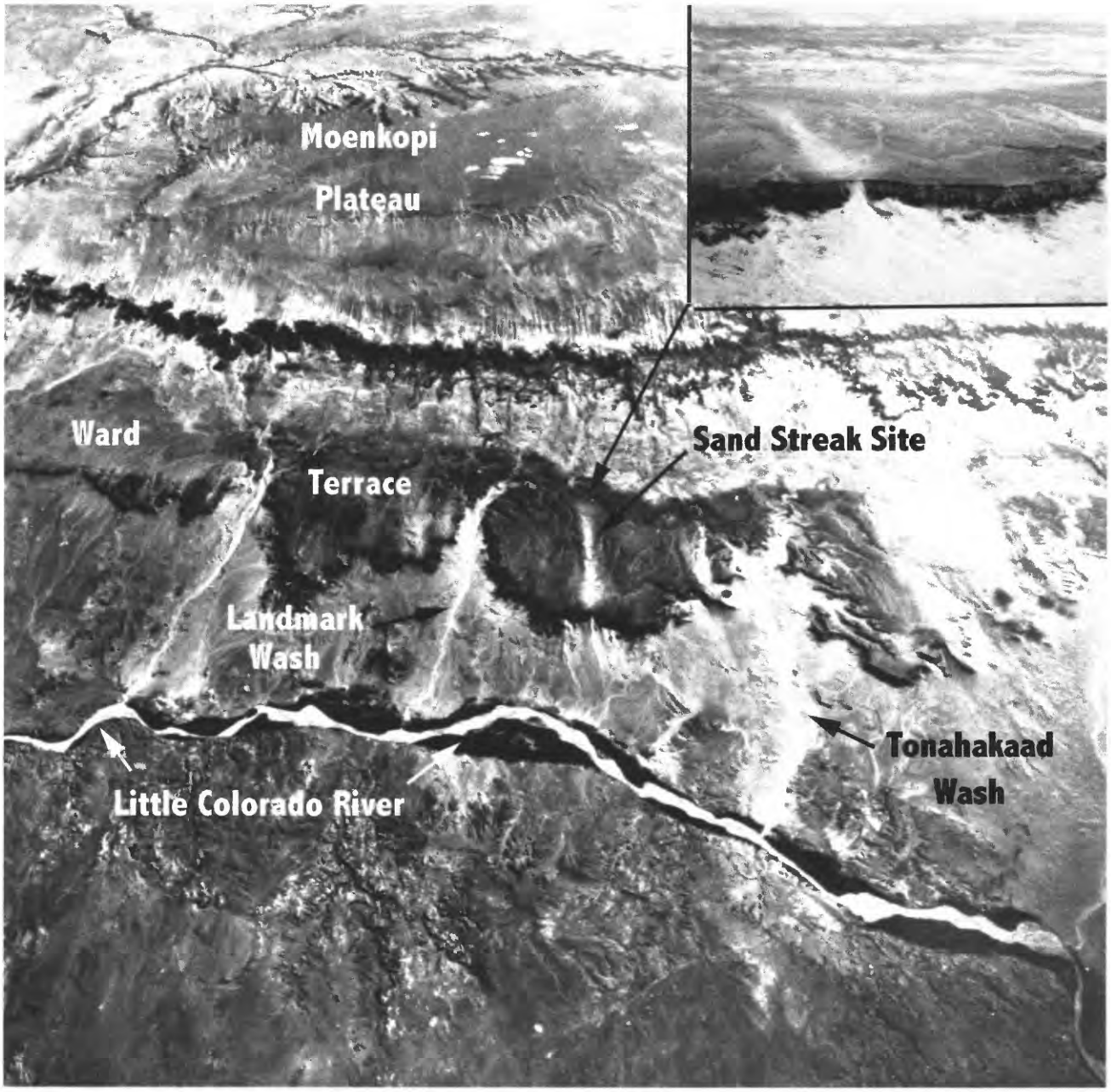
Moenkopi
Plateau
Ward
Terrace
Sand Streak Site
Landmark
Wash
Little Colorado River
Tonahakaad
Wash

Figure 15

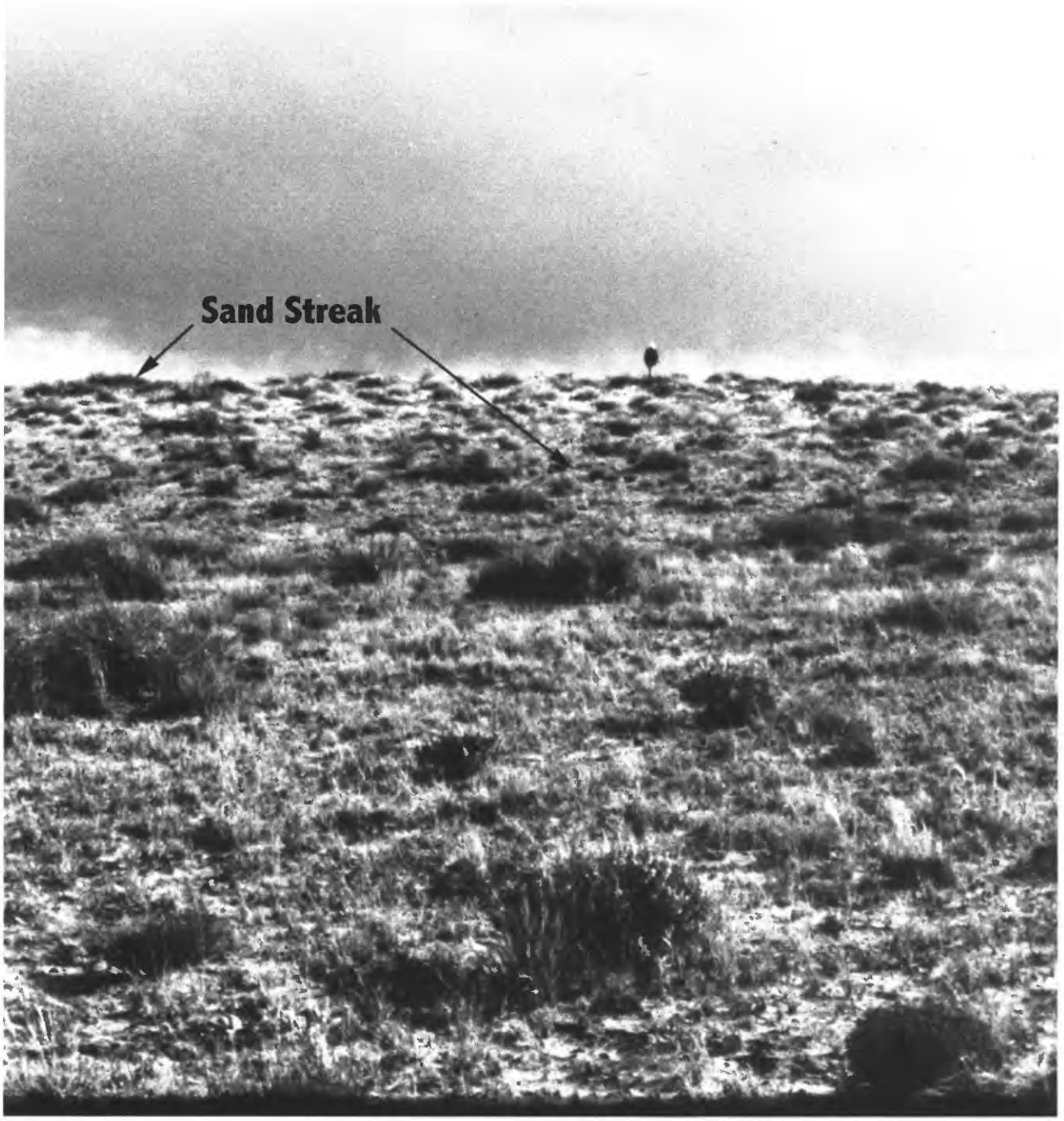

Figure 16a

Figure 16b

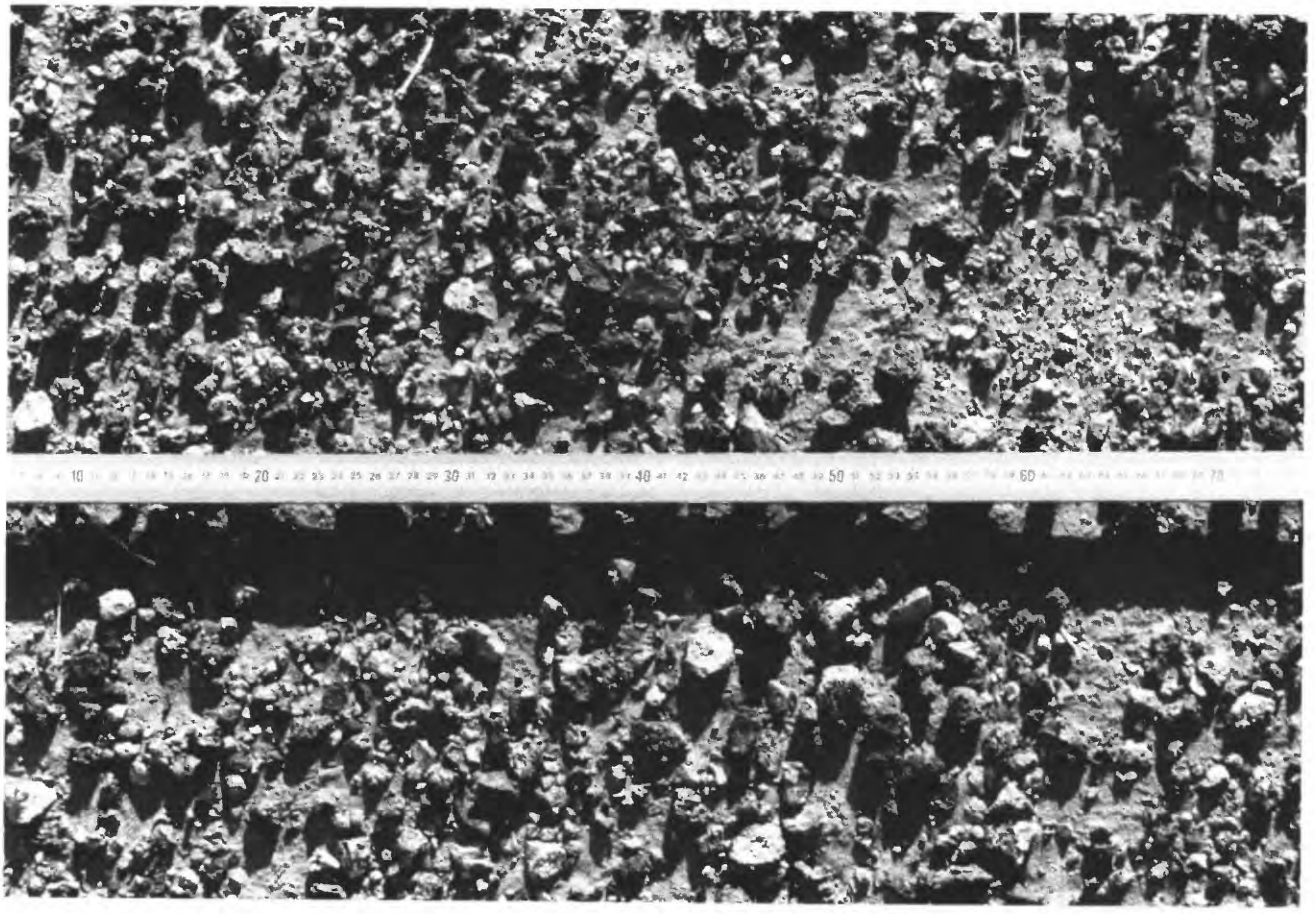

Figure 16c

Figure 16d

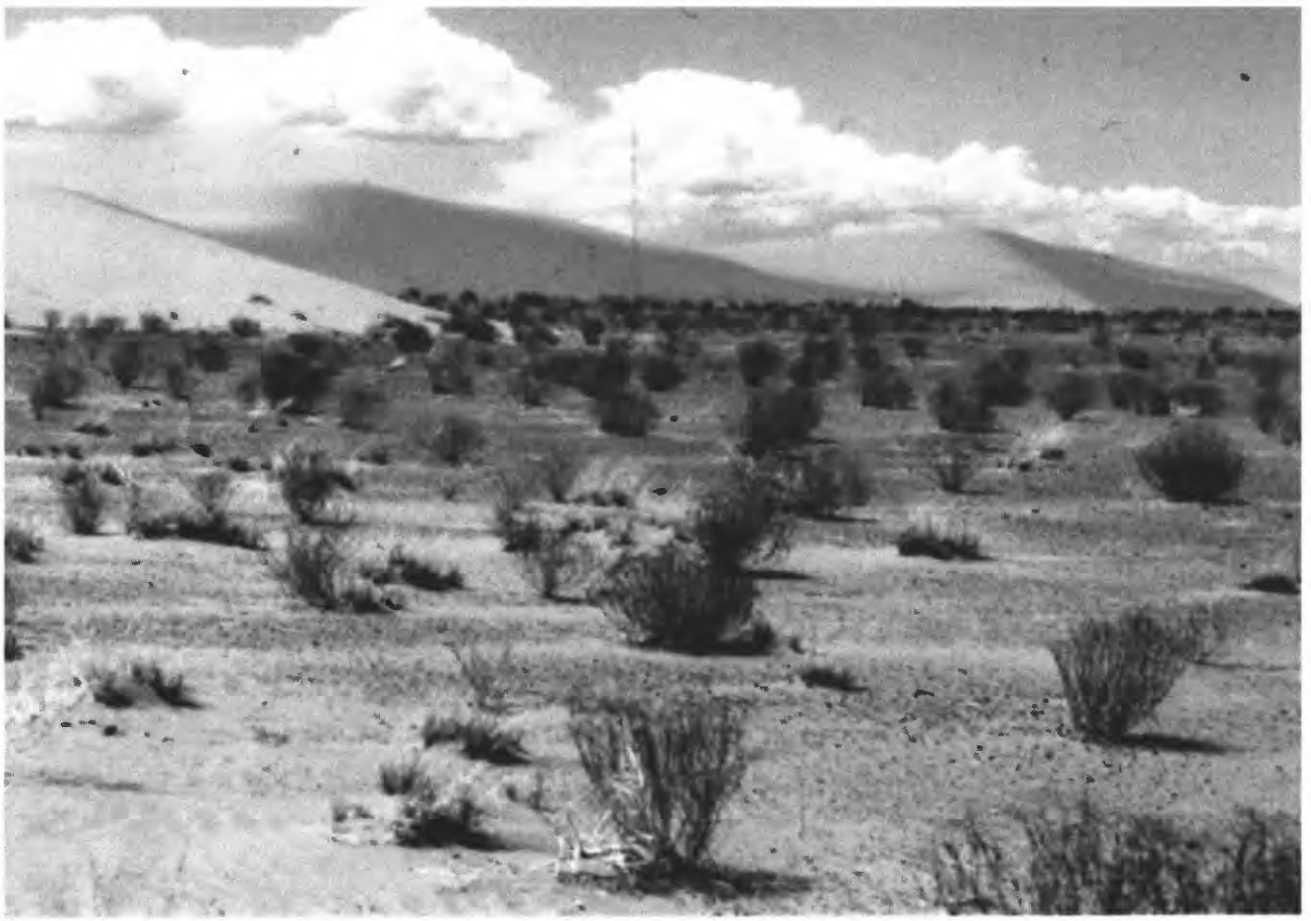

Figure 16e

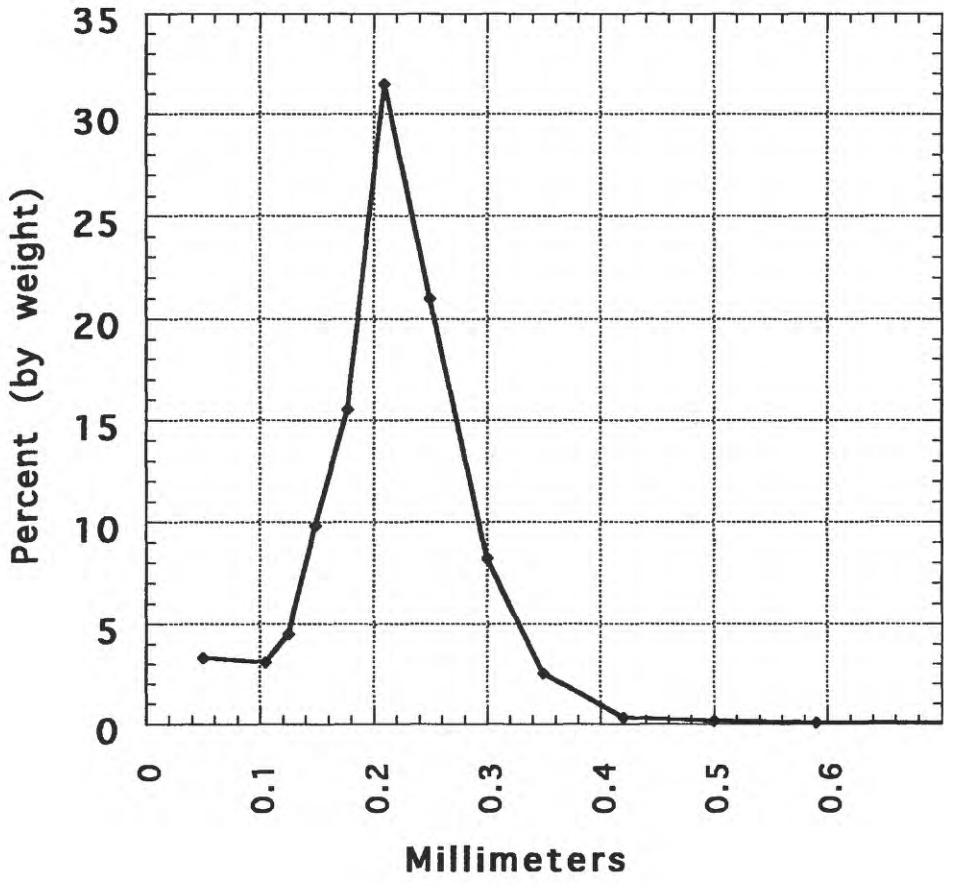

Figure 17

Schaber and Breed

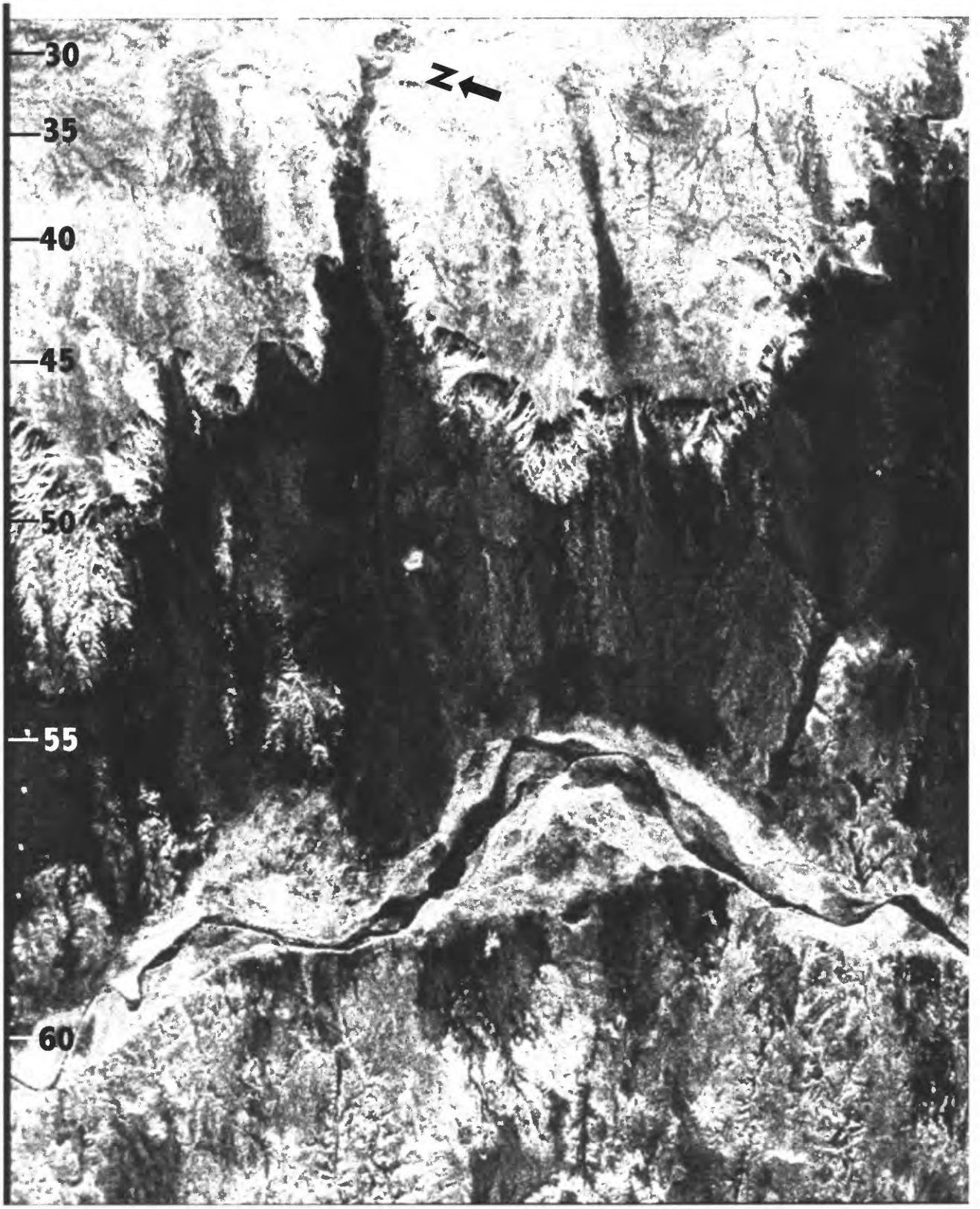

Figure 18a

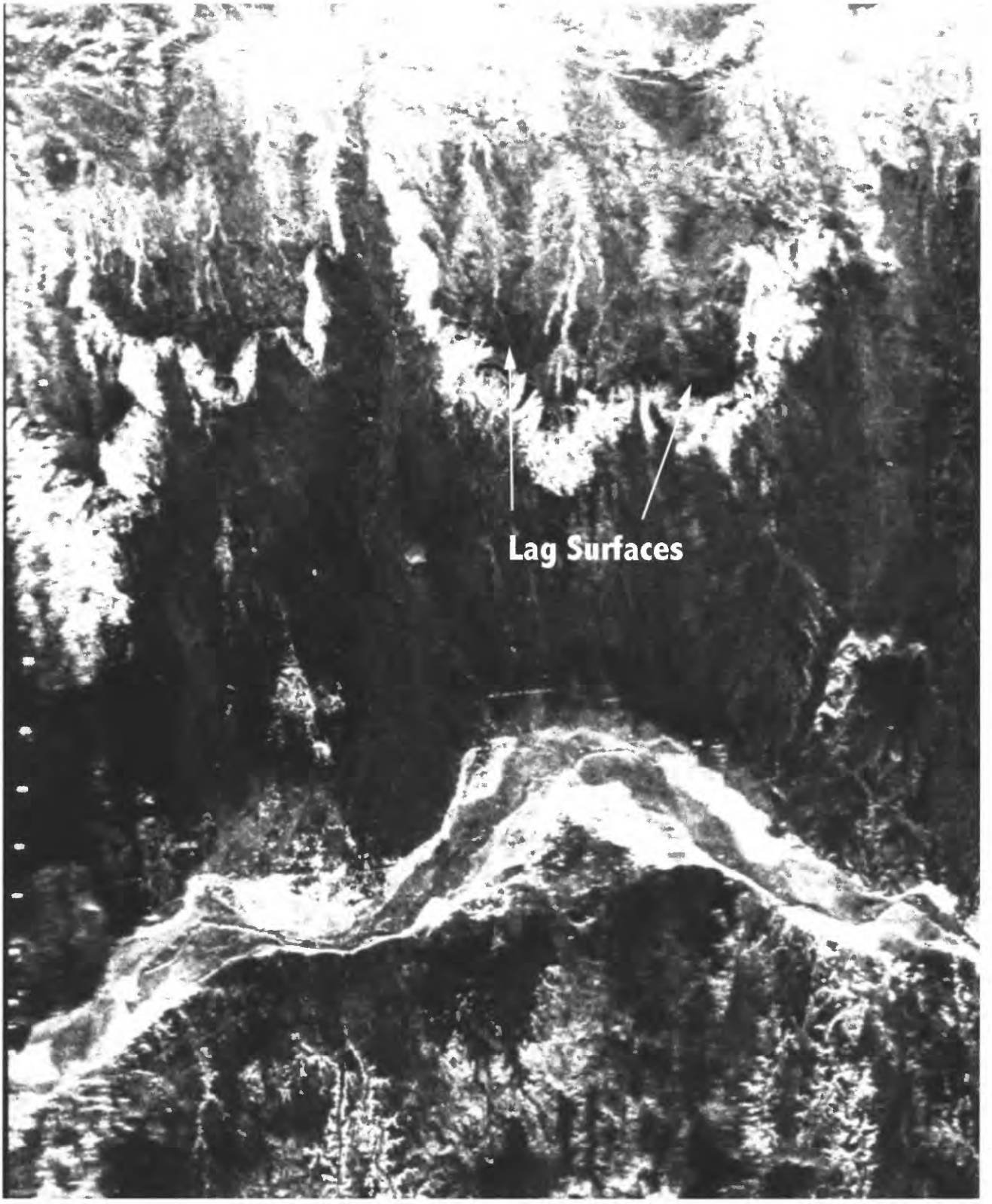

Figure 18b

Schaber and Breed

Figure 18c

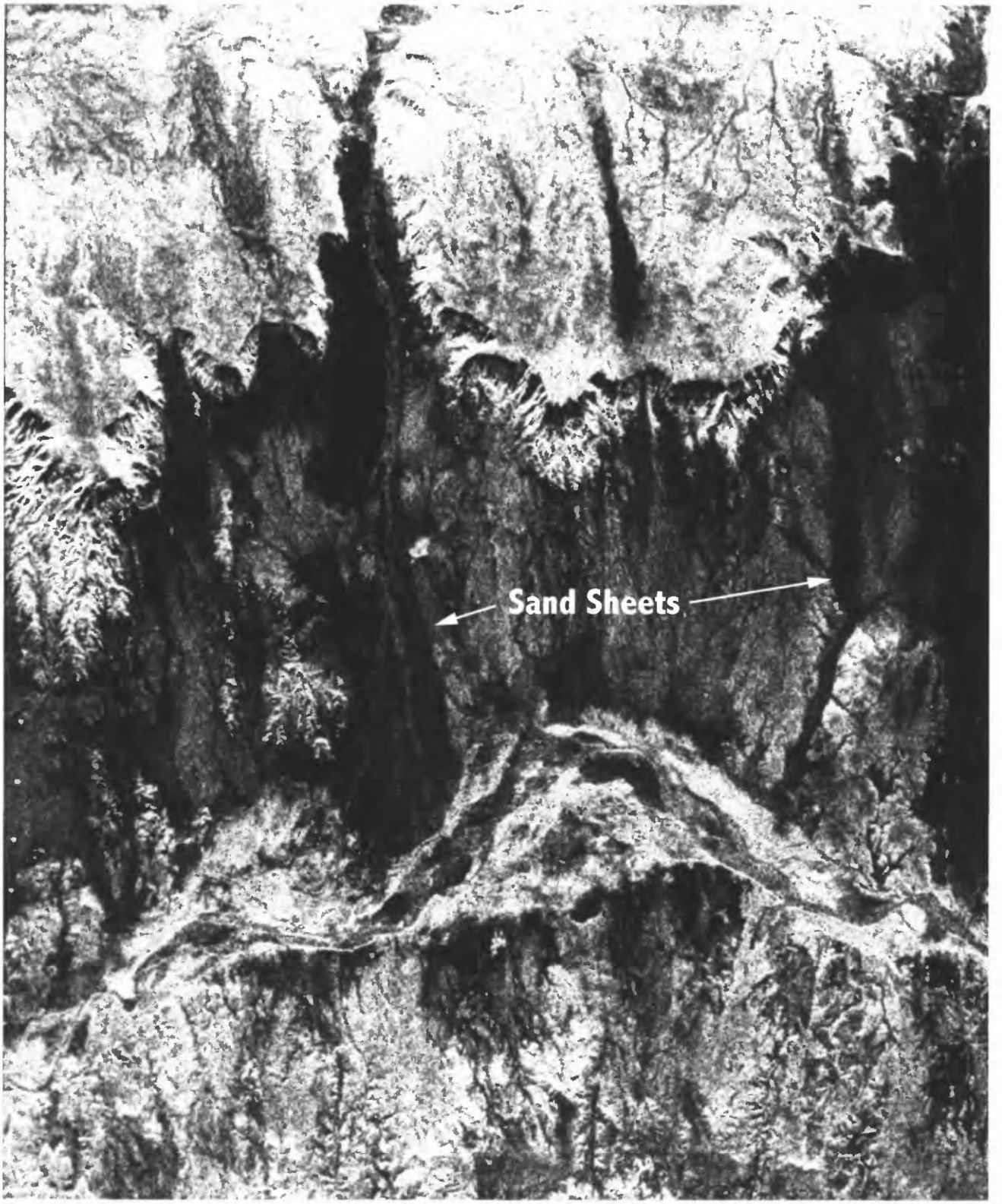

Figure 18d

Figure 18e

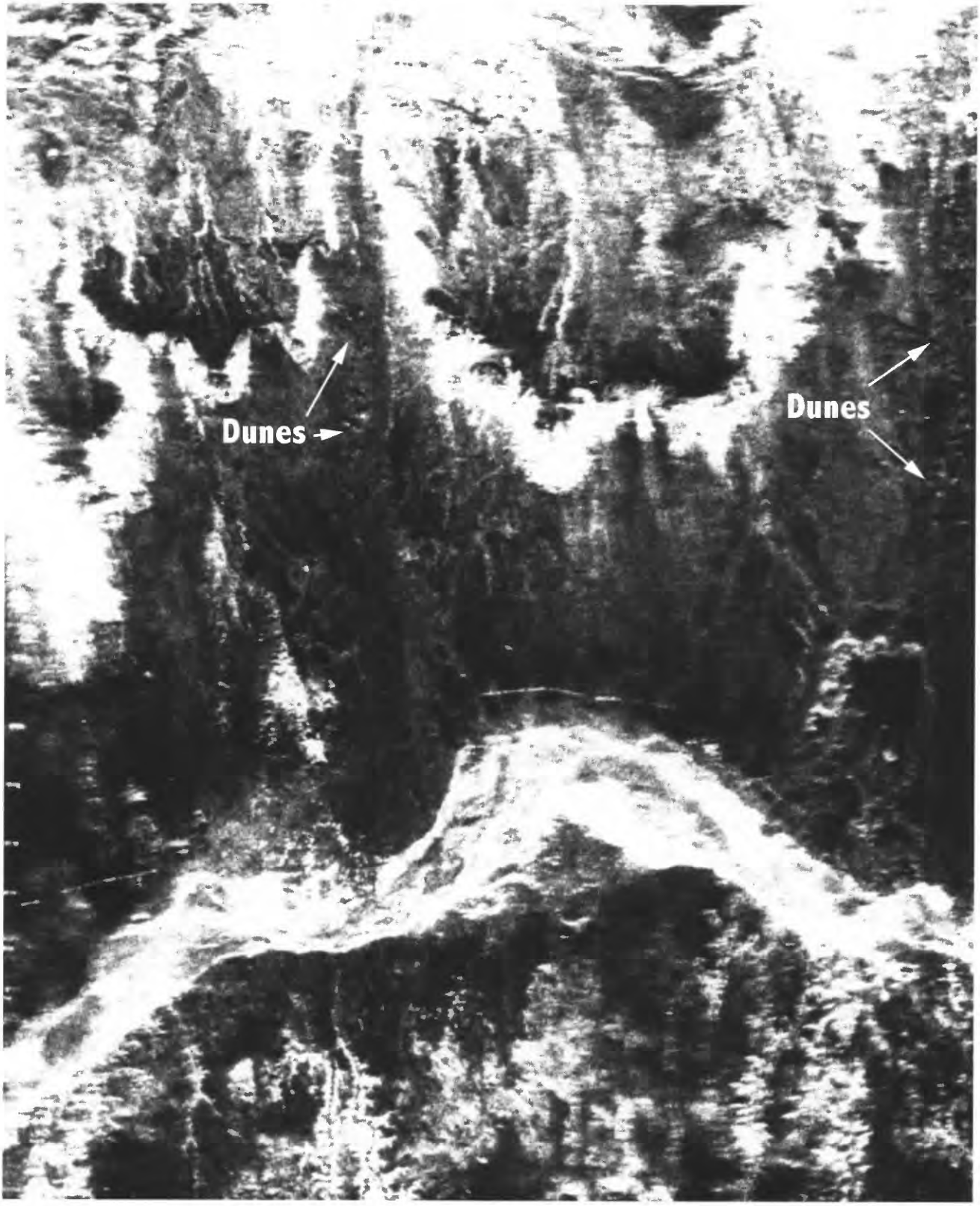

Figure 18f

Figure 18g

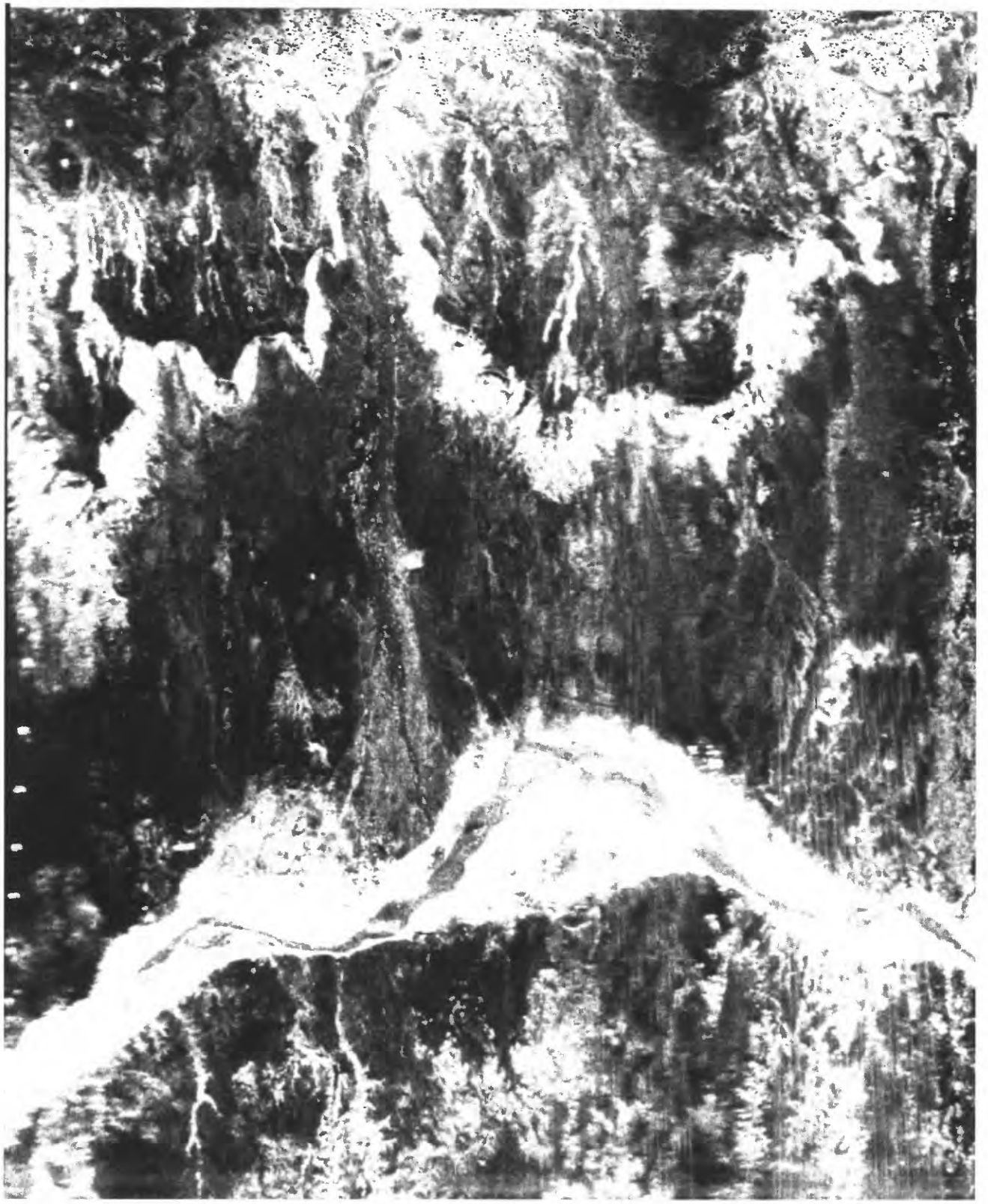

Figure 18h

Figure 18i

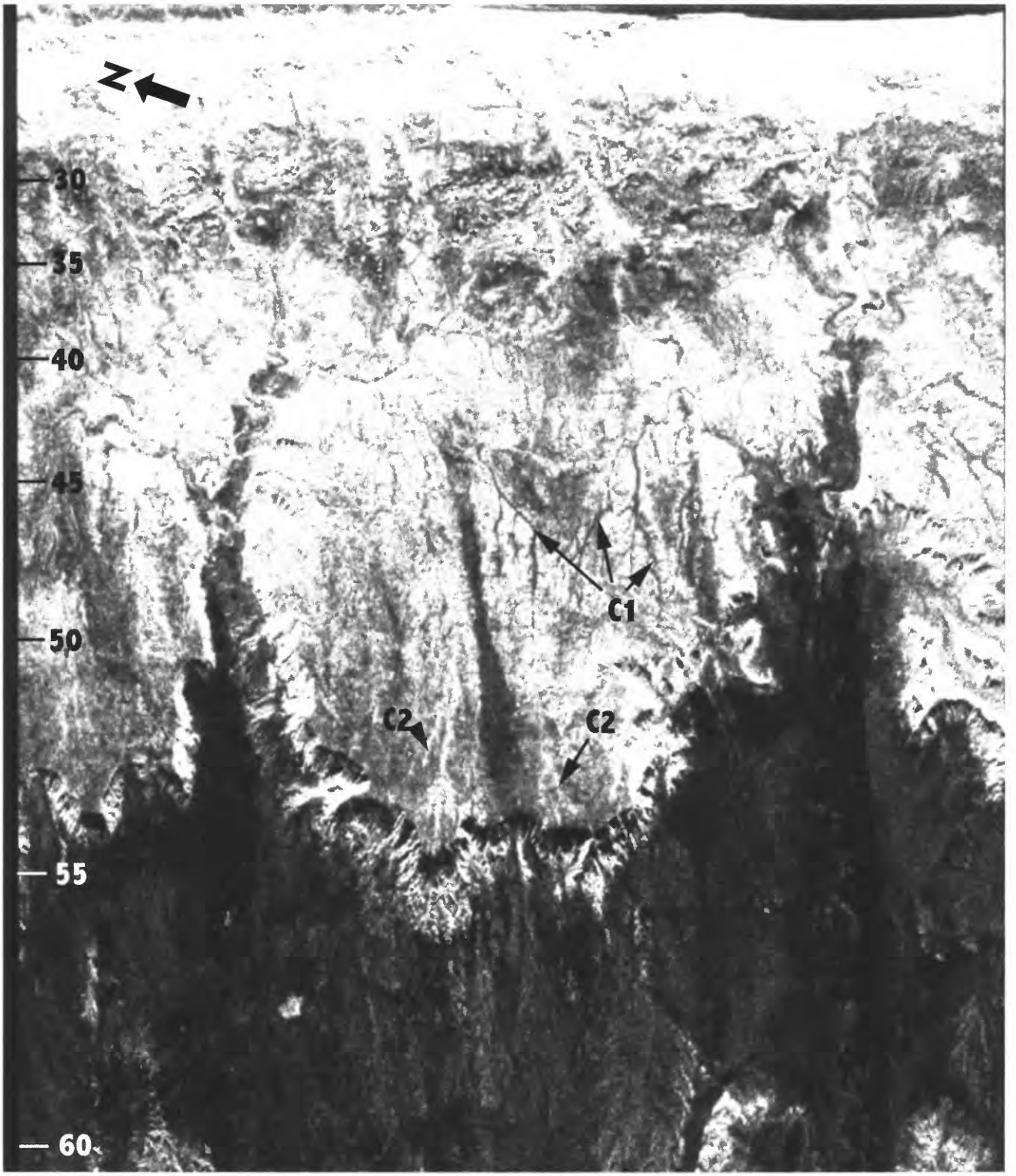

Figure 19a

Figure 19b

Figure 19c

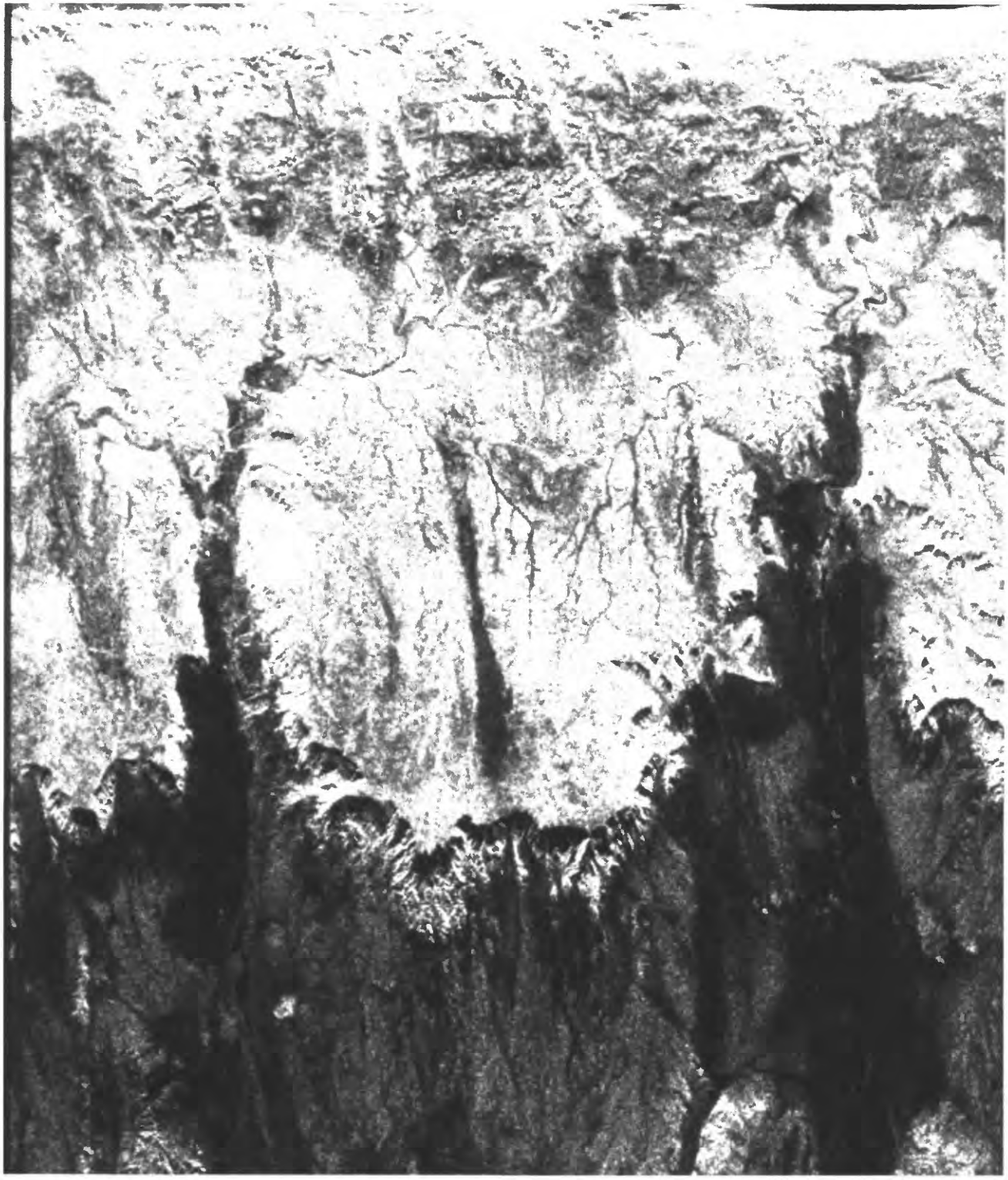

Figure 19d

Figure 19e

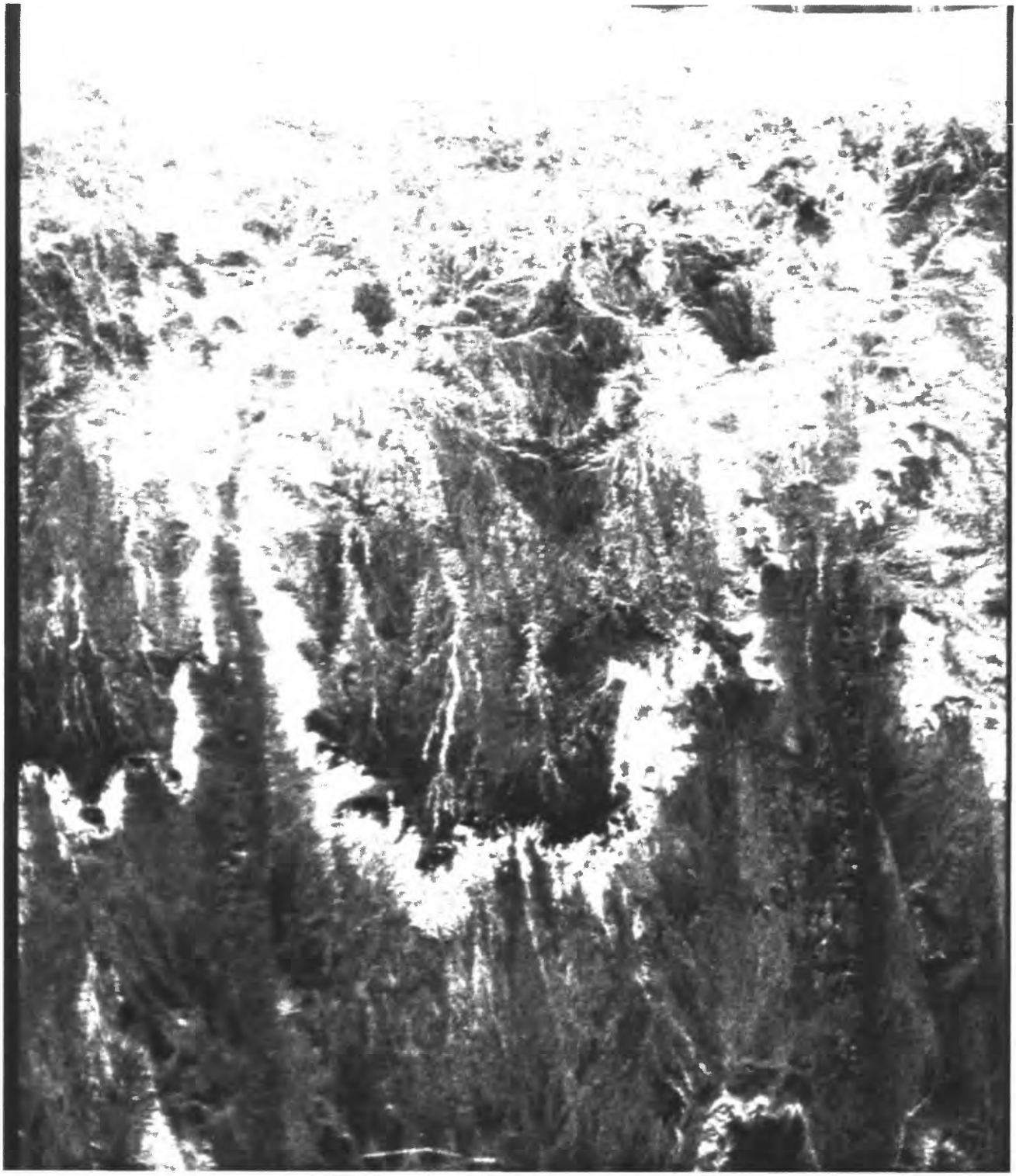

Figure 19f

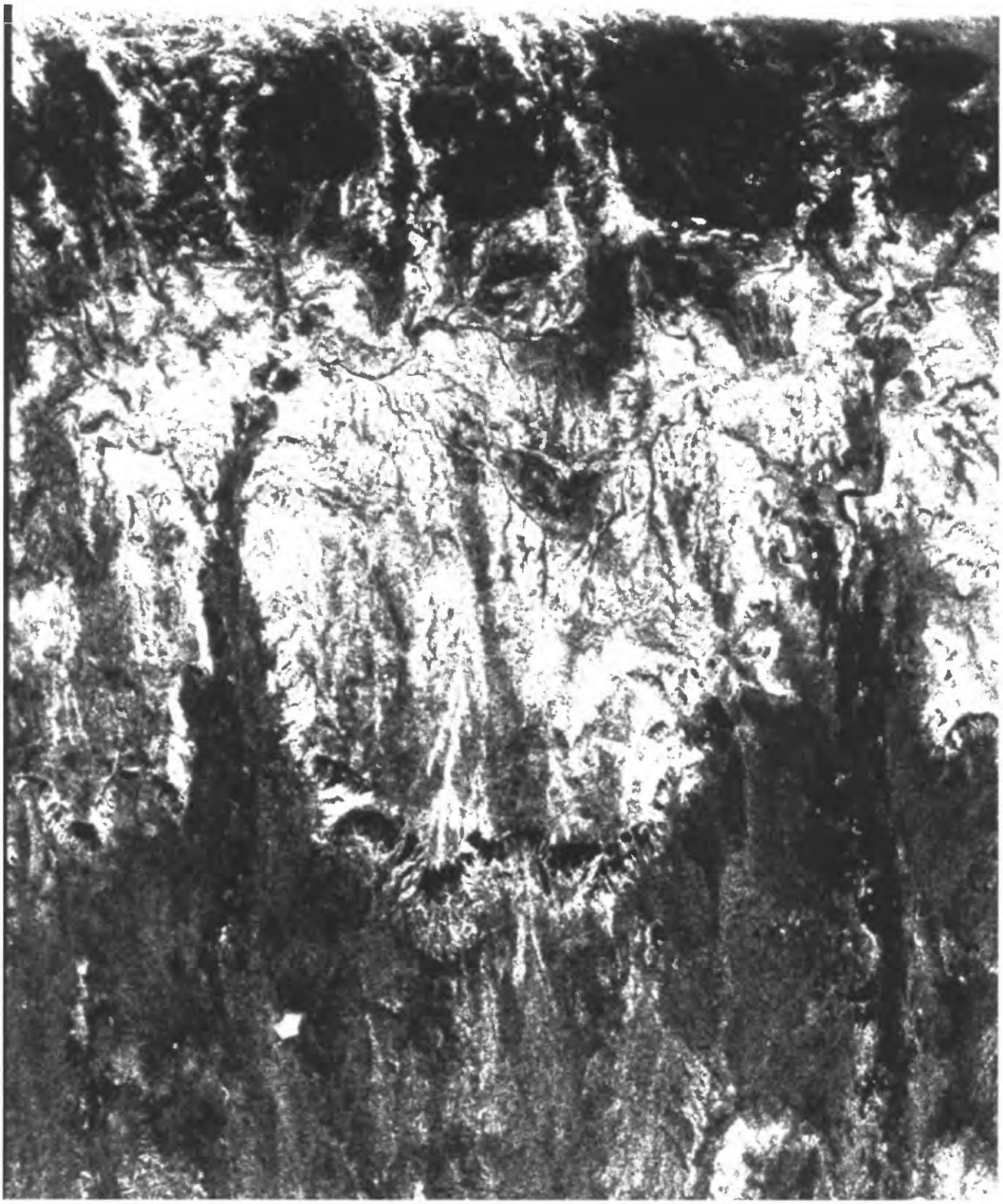

Figure 19g

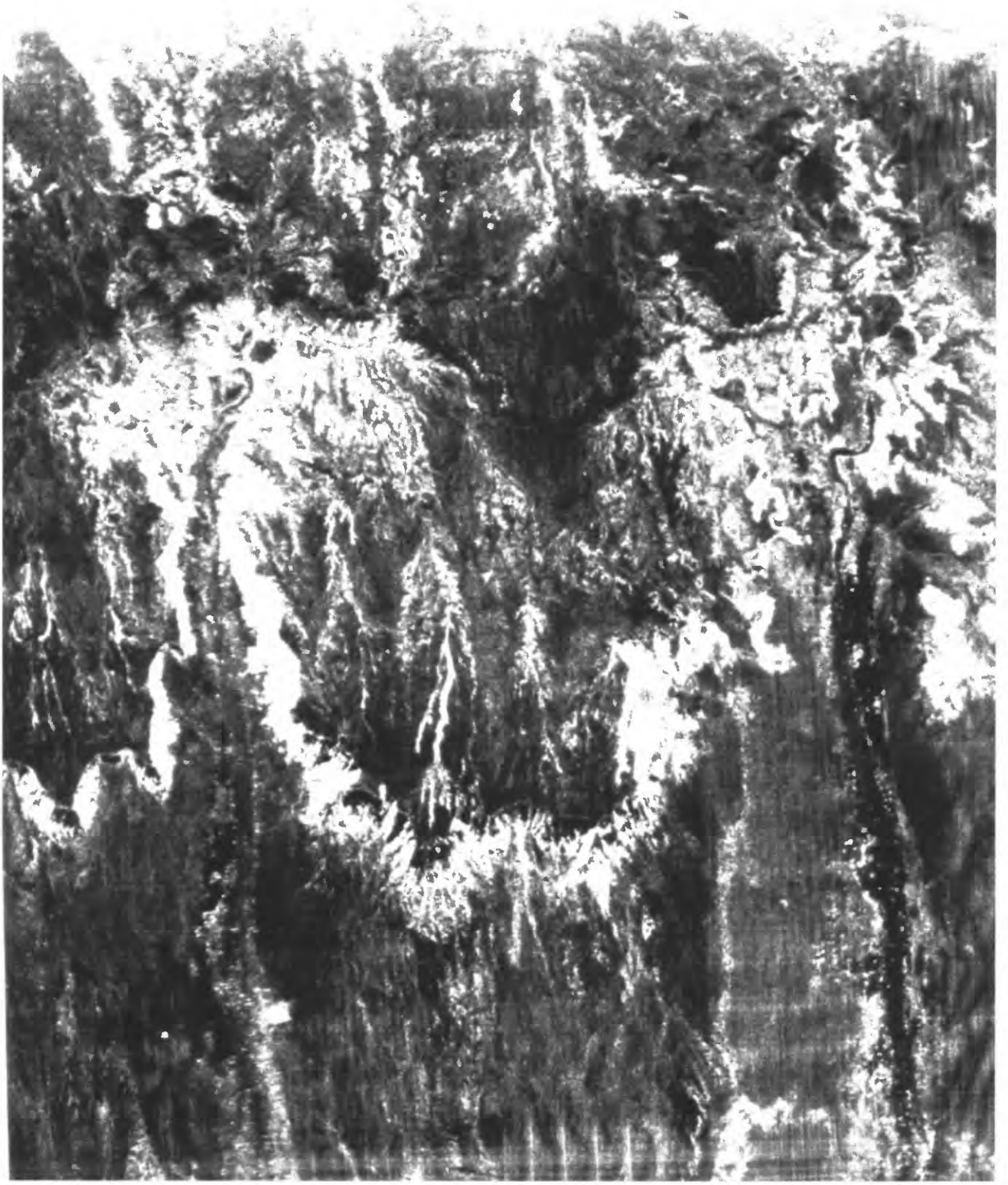

Figure 19h

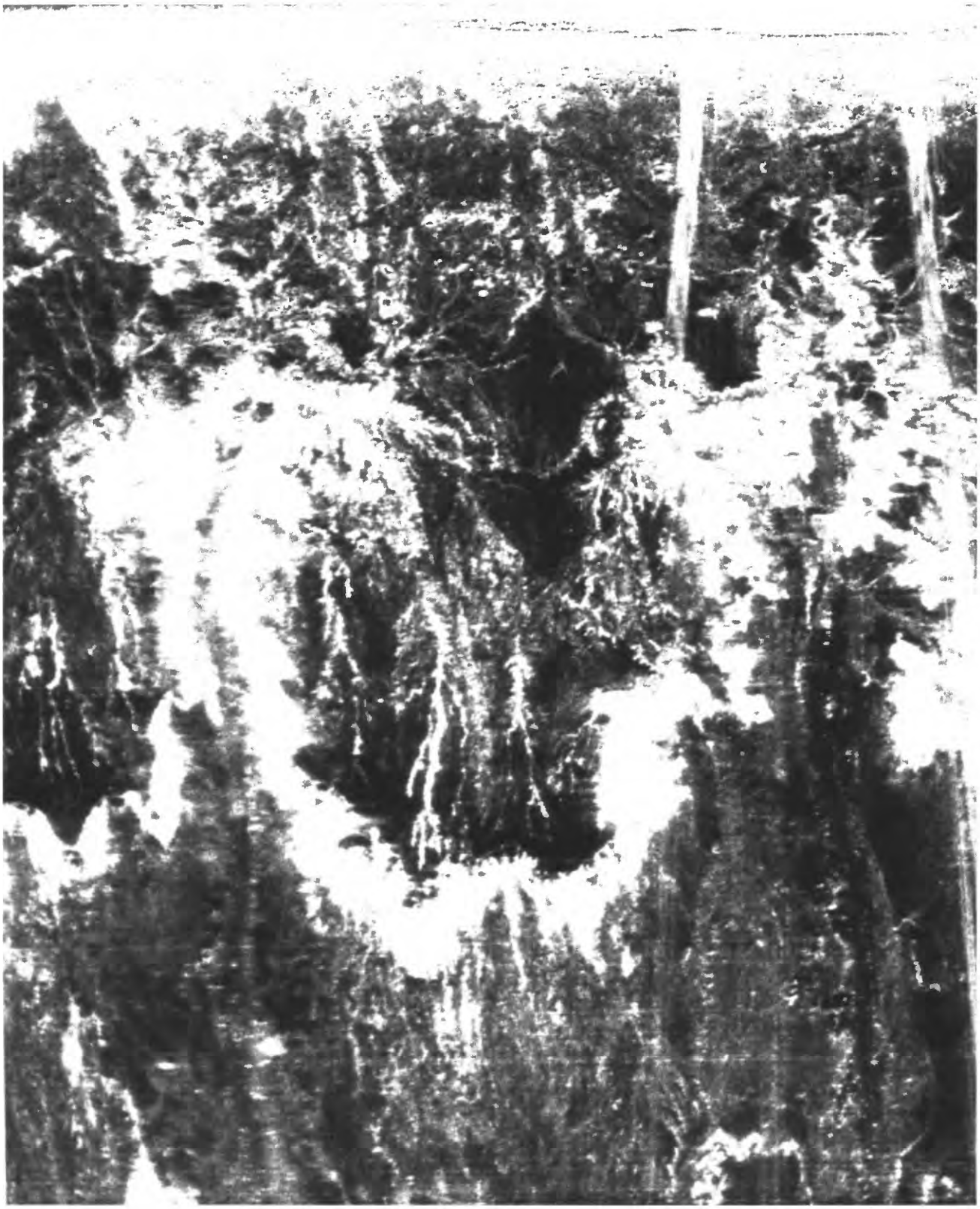

Figure 19i

Schaber and Breed

Figure 20a

Figure 20b

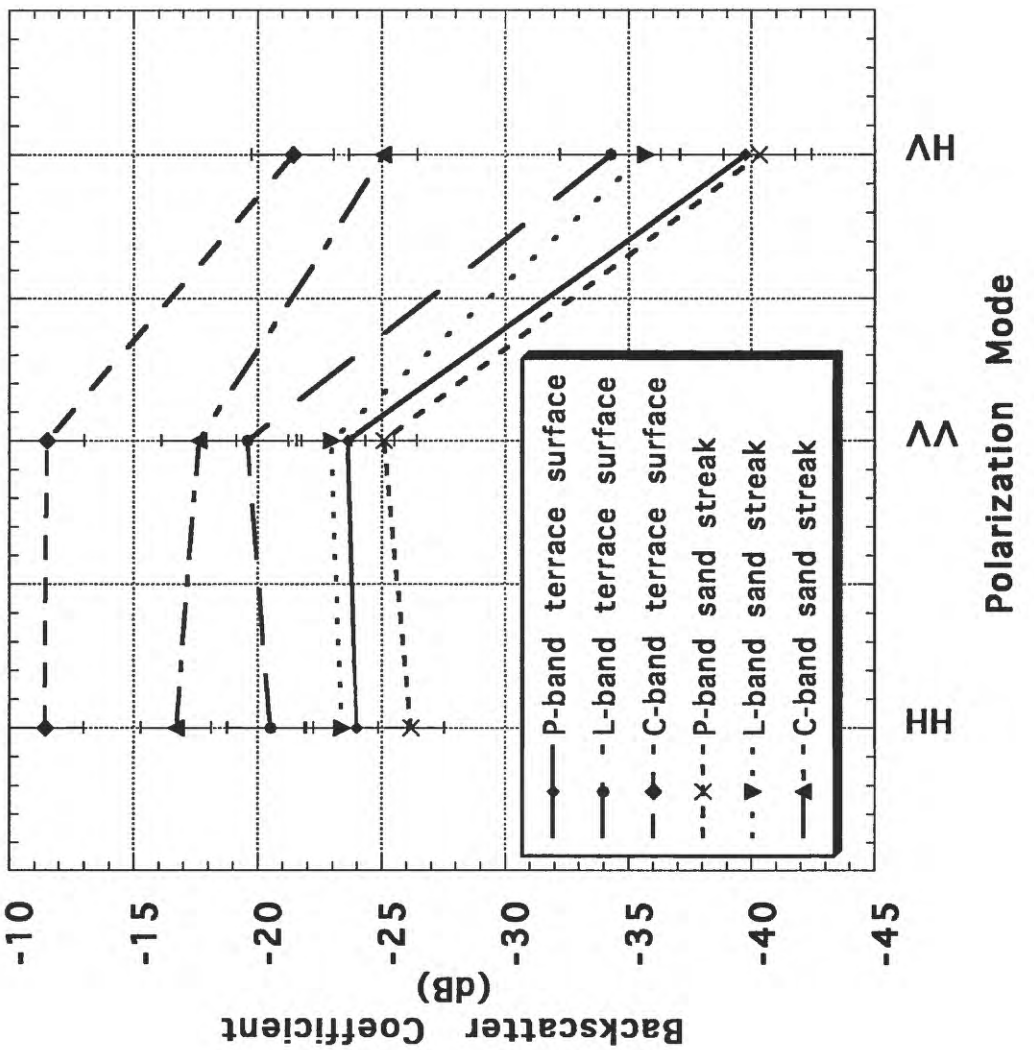
Backscatter Coefficient (dB)
-10
-15
-20
-25
-30
-35
-40
-45
HH
VV
HV
Polarization Mode
P-band terrace surface
L-band terrace surface
C-band terrace surface
P-band sand streak
L-band sand streak
C-band sand streak

Figure 21a

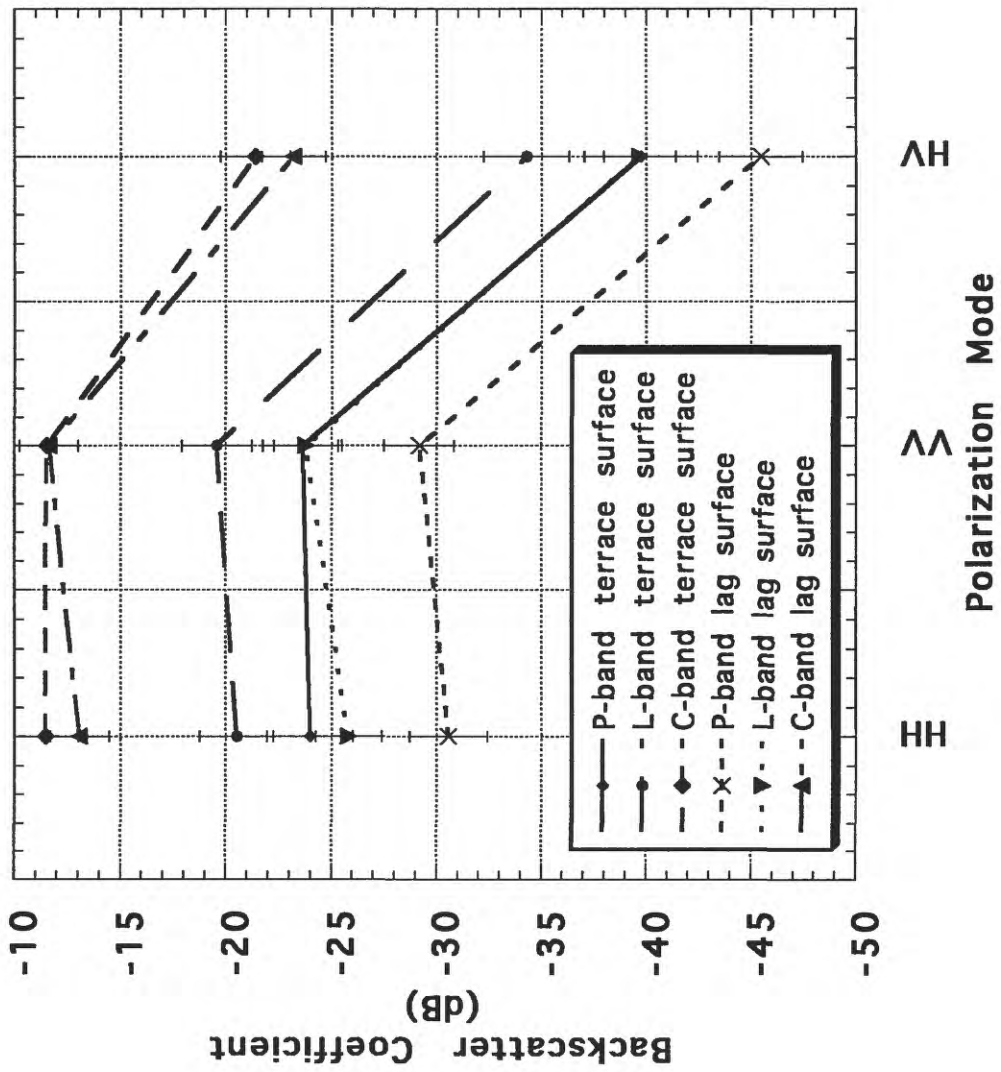
Backscatter Coefficient (dB)
-10
-15
-20
-25
-30
-35
-40
-45
-50
HH
VV
HV
Polarization Mode
P-band terrace surface
L-band terrace surface
C-band terrace surface
P-band lag surface
L-band lag surface
C-band lag surface

Figure 21b

Figure 22

(68 cm)
1.18 (7.35)
2.35 (3.7)
2.93 (0.74)
4.19 (0.52)
5.87 (0.37)

(dB/m)

Table 1. Theoretical Radar Imaging Depth[a] and Attenuation (db/m) vs. Loss Tangent for X-, C-, and L-Band Radar Signals in Desert Sediments with Low-to-Medium Loss

Loss Tangent (Tan δ)	*X-Band (3 cm)*	*C-Band (6 cm)*	*L-Band (24 cm)*	*Geologic Medium (Examples)*
0.1	0.05 (167.5)	0.10 (83.8)	0.42 (20.9)	Gravelly to moderately cemented sandy alluvium
0.05	0.10 (83.9)	0.21 (41.9)	0.83 (10.48)	Small-gravel sandy alluvium
0.01	0.13 (16.77)	0.26 (8.39)	1.04 (2.10)	Fine-grained sandy alluvium
0.007	0.18 (11.74)	0.37 (5.87)	1.48 (1.47)	Dry blow sand
0.005	0.26 (8.39)	0.52 (4.19)	2.07 (1.05)	Dry blow sand

[a] The values above are computed assuming that the radar imaging depth (RID) (see Footnote 1) (two-way penetration depth-in and -out) of a low loss medium (e.g., dry sand or small-pebble alluv.) with a complex dielectric constant (ε_c) of 3.4 is equivalent to 0.25 times the attenuation distance ($1/a$) as defined in the equations below (Von Hippel, 1954, p. 28). Such a relationship was determined empirically at a wavelength (λ) of 25 cm by Schaber et al. (1986) following field and laboratory studies of SIR-A data in southern Egypt and northwestern Sudan. The attenuation produced by a dielectric is frequently expressed as the attenuation distance, $1/a$ through which the field strength decays to $1/e=0.368$ of its original value. The following formulas are taken from Von Hippel (1954, pp. 29–33).

Attenuation Distance (m): 1) For $\tan\delta=0.0001$–0.05: $$\frac{1}{a}=\frac{\lambda}{(\pi\tan\delta)(\sqrt{\varepsilon_c})};$$

2) for $\tan\delta=0.05$–50: $$\frac{1}{a}=\frac{\lambda}{2\pi}\sqrt{\frac{2}{(\varepsilon_c)(\sqrt{1+\tan\delta}-1}}.$$

Attenuation 8,686a (db per meter): 1) For $\tan\delta=0.0001$–0.05: $$8.686a=\frac{(8.686)(\pi)(\tan\delta)}{\lambda}(\sqrt{\varepsilon_c});$$

2) for $\tan\delta=0.05$–50: $$8.686a=\frac{17.37\pi}{\lambda}\sqrt{\frac{(\varepsilon_c)(\sqrt{1+\tan\delta}-1}{2}}.$$

Table 2- Information On SAR Images Shown For The Yuma Site					
SAR SENSOR	ACQUISITION DATE	SAR BAND/	POLAR.	INCIDENCE ANGLE	IMAGE
AIRSAR [MISSION NO. (FLIGHTLINE)]	(ARCHIVE ID No.)	WAVELENGTH	MODES	(DEGREES)	RESOLUTION
SRL (SIR-C/X-SAR) [DATA TAKE NO.]		(CM)			(M)
ERS [ORBIT/TRACK]					
AIRSAR-290(1) GR*	5/21/91(CCT ID CP1253/Near)	C/6, L/24, P/68	HH, VV, HV	25 to 55	5
SRL-1 D.T. 56.30 GR#	4/12/94 (X-band HRMGDDP19960603201414)	X/3, C/6, L/24	HH,HV	X-band=20.2;	25
	(C-band PR 11652, L-band PR 11651)			C- and L-band=22.7	
ERS-1(4466/313) GR	5/23/92 (CCT ID S0005742)	C/6	VV	23	25
*SL = Slant range projection geometry (See Sabins, 1997, pp. 181-182)					
#GR = Ground range projection geometry (See Sabins, 1997, pp. 181-182)					

Table 3- Priority Ranking of AIRSAR Images From pass 290-1 For Delineating Geologic Units, Ordnance Targets, and Cultural Features at the Yuma Study Site (Barry M. Goldwater Bombing and Gunnery Range, Arizona)(Refer to Fig. 4)	
Geologic Units, Ordnance Targets, and Cultural Features	**Recognition Level Ranking (Best to Worst-L to R)**
Sand-Mantled Alluvium (Unit 1)	PHH(VV)*[1]**, CHH(VV)[2], LHH(VV)***, CHV***, LHV# PHV#
Scald Surfaces (Unit 2)	PHH(VV)##, LHH(VV), CHH(VV)***, CHV***, LHV#, PHV#
Coarse river gravels (Unit 3)	CHH(VV)##[1], CHV[1], PHH(VV)[2], LHH(VV)***, LHV#, PHV#
Gunnery Target T1(ordnance debris)[1]	PHV##^, LHV^, PHH(VV), LHH(VV), CHV, CHH(VV)
Gunnery Target T1 (target circle)[2]	CHV, PHH(VV), LHH(VV), CHH(VV), LHV, PHV
Gunnery Target T1 (perimeter of tires)[1]	LHV, PHV, PHH(VV), LHH(VV), CHH(VV), CHV
Gunnery Target T2 (ordnance debris)[1]	PHV##, LHV, PHH(VV), LHH(VV), CHV, CHH(VV)
Gunnery Target T2 (target circle)[2]	Not discernible on any AIRSAR image; obscured by ordnance debris
Gunnery Target T2 (perimeter of tires)[1]	Not discernible on any AIRSAR image; obscured by ordnance debris
Gunnery Target T3 (ordnance debris)[1]	PHV, LHV, PHH(VV), LHH(HV), CHV, CHH(VV)
Gunnery Target T3 (twin mounds)[1]	PHV, LHV, CHV, CHH(VV), PHH(VV), LHH(VV)
Access Roads	CHH(VV)[1], CHV[2], PHH(VV)[1,2], PHV, LHV[2], LHH(VV)[2]
Fence lines	PHV##[1], PHH[1] (ENE-trending fences best), LHH[1] (ENE-trending fences
	only), LHV[1]; Not discernible on CHH(VV), CHV, and LHH(VV) images
*( ) Overall equivalent ranking	
**[ ] Image tone (1=radar bright, 2=radar dark)	
***Poorly delineated	
# Very Poorly Delineated	
## Far superior to all other SAR Images	
^ Obscured in part by radar interference	

Table 4- Standard Deviation of Height (cm) For Four Rayleigh Roughness Criteria*					
SAR BAND	WAVELENGTH (CM)	RAYLEIGH TRANSITION	RAYLEIGH ROUGH	RAYLEIGH SMOOTH	FRAUNHOFER SMOOTH
		22 DEGREE INCIDENCE ANGLE			
P	68.0	9.17	16.67	2.93	2.29
L	24.5	3.30	6.00	1.06	0.82
C	5.7	0.77	1.40	0.25	0.19
X	3.0	0.40	0.74	0.13	0.10
		45 DEGREE INCIDENCE ANGLE			
P	68.0	12.02	21.85	3.85	3.00
L	24.5	4.33	7.87	1.38	1.08
C	5.7	1.01	1.83	0.32	0.25
X	3.0	0.53	0.96	0.17	0.13
		55 DEGREE INCIDENCE ANGLE			
P	68.0	14.82	26.94	4.74	3.70
L	24.5	5.34	9.71	1.71	1.33
C	5.7	1.24	2.26	0.40	0.31
X	3.0	0.65	1.19	0.21	0.16

* See footnote 5 in text for explanation of Rayleigh Criteria

Table 5-Portrayal on ERS-1 CVV Image of Geologic Units, Ordnance Targets, and Cultural Features at the Yuma Study Site (Barry M. Goldwater Bombing and Gunnery Range, Arizona)(Refer to Fig. 12)	
Geologic Units, Ordnance Targets, and Cultural Features	**Portrayal on Image**
Sand-Mantled Alluvium (Unit 1)	Non-descript compared to AIRSAR CVV image
Scald Surfaces (Unit 2)	Radar dark [2]* as opposed to radar bright [1] on AIRSAR CVV equivalent (see text discussion); better contrasted against unit 1 on AIRSAR image
Coarse river gravels (Unit 3)	Very poorly delineated from Unit 1 compared to AIRSAR (see Fig. 4a,d)
Gunnery Target T1(ordnance debris)[1]	Only core area of debris field well defined
Gunnery Target T1 (target circle)[2]	Very well defined; much better than on AIRSAR CVV image (see Fig. 4d)
Gunnery Target T1 (perimeter of tires)	Not discernible
Gunnery Target T2 (ordnance debris)[1]	Only core area of debris well defined
Gunnery Target T2 (target circle)	Not discernible; obscured by ordnance debris
Gunnery Target T2 (perimeter of tires)	Not discernible; obscured by ordnance debris
Gunnery Target T3 (ordnance debris)	Not discernible
Gunnery Target T3 (twin mounds)	Not discernible
Access Roads	Only small sections visible; very poorly defined [2]
Fence Line	Not discernible
*[ ] Radar bright [1] or radar dark [2]	

Table 6- Priority Ranking of SRL-1 (SIR-C/X-SAR) Images from Data Take 56.3 For Delineating Geologic Units, Ordnance Targets, and Cultural Features at the Yuma Study Site (Barry M. Goldwater Bombing and Gunnery Range, Arizona)(Refer to Fig. 13)	
Geologic Units, Ordnance Targets, and Cultural Features	**Recognition Level Ranking (Best to Worst-L to R)**
Sand-mantled alluvium(Unit 1)	LHH[2]**, XVV[1], CHV[1], CHH#, CHV#, LHV^
Scald surfaces (Unit 2)	LHH##, CHH, CHV***, XVV***, LHV^
Coarse river gravels (Unit 3)	XVV[1], LHH[2], CHH, LHV^
Gunnery Target T1(ordnance debris) [1]	LHV##(despite excessive interference), CHV, LHH, CHV, CHH, XVV
Gunnery Target T1 (target circle)[2]	CHH, LHH, XVV, CHV, LHV
Gunnery Target T1 (perimeter of tires)[1]	XVV***, Not discernible on other SRL images
Gunnery Target T2 (ordnance debris) [1]	LHV##(despite excessive interference), CHV, XVV,
Gunnery Target T2 (target circle) [2]	Not discernible on any SRL image; obscured by ordnance debris
Gunnery Target T2 (perimeter of tires) [1]	Not discernible on any SRL image; obscured by ordnance debris
Gunnery Target T3 (ordnance debris) [1]	LHV##(despite excessive interference), CHV, CHH, LHH, XVV#
Gunnery Target T3 (twin mounds) [1]	LHV#, CHV, CHH, LHH#, XVV#
Access roads	Barely discernible [1] on all SRL images
Fence lines	Not discernible on any SRL image
*( ) Overall equivalent ranking	
**[ ] Image tone (1=radar bright, 2=radar dark)	
***Poorly delineated	
# Very Poorly Delineated	
## Far superior to all other SRL Images	
^Image degraded by radar interference	

Table 7- Information On SAR Images Shown For The Ward Terrace Sand Streak Site					
SAR SENSOR (FLIGHTLINE OR ORBIT/TRK) PROJECTION MODE	ACQUISITION DATE (OUTPUT ID)	SAR BAND/ WAVELENGTH (CM)	POLARIZATION MODES	INC. ANGLE (RANGE) (DEGREES)	IMAGE RESOLUTION (M)
AIRSAR/340(2A), SL* (Pass A)	5/21/91(CM3139)	C/6, L/24, P/68	HH, VV, HV	25 to 65 degrees	5
AIRSAR/340(6A), SL (Pass B)	5/21/91 (3323C)	C/6 , L/24, P/68	HH, VV, HV	10 to 60 degrees	5
ERS/1(PRI)(4881/227) GR**	5/23/92 (CCT ID S0005744)	C/6	VV	23 degrees	25
* SL = Slant range projection geometry (See Sabins, 1997, pp. 181-182)					
**GR = Ground range projection geometry (See Sabins, 1997, pp. 181-182)					

Table 8- Priority Ranking of AIRSAR Images From Pass A (340-2) For Delineating Selected Geologic Features At Ward Terrace (see Figure 18)	
Geologic Feature	**Recognition Level Ranking**
	(Best to Worst-L to R)
Sand streak on Ward Terrace	CVV(HH)#, CHV (penetrated at L- and P-band)
Recent drainages with sand	CHV, CHH, CVV (undetectable on L- and P-band images)
In-filled floors on NE side	
of Ward Terrace	
Dendritic channels on both	PHV, LHV, PHH(VV), LHH(VV), CHV, CHH, CVV
sides of the sand streak on	
Ward Terrace	
Flat, lag-covered surfaces	PHV, PHH, PVV, LHV, LHH, LVV, CHV, CHH, CVV
on Ward Terrace	
Barchan dunes in Landmark	LVV(HH), PHH(VV), LHV, PHV**, CHV, CHH, CVV
Tonahakaad Washes	
Contact of elongate sand sheets	CVV(HH)# (undetectable on other SAR images)
in Landmark and Tonahakaad	
Washes	
Recent drainage channels in	LHV, CVV, CHH, LVV(HH), CHV, PVV, PHH, PHV**
Landmark Wash	
Full width of Landmark Wash	CHV, PVV, CHH, PHH(VV), LHH(VV), PHV, CHV
Roughness variations within	CHH, CHV, CVV, LHH, PHH, PHV, LVV, LHV,PVV
the Little Colorado River	
channel	
* ( ) Overall equivalent ranking	
# Far superior to all other SAR frequency/polarization modes	
** Somewhat obscured by image smear (see text)	

Table 9- Priority Ranking of AIRSAR Images From Pass B (340-6) For Delineating Selected Geologic Features at Ward Terrace (See Figure 19)	
Geologic Feature	**Recognition Level (Best-to-Worst; L-to-R)**
Sand streak on Ward Terrace	CVV(CHH)*#, CHV, LHH(VV), LHV (penetrated at P-band)
Dendritic channels with sand In-filled floors on NE side of Ward Terrace	CVV(CHH), CHV, LHH(VV), PHH(VV), LHV, PHV
Dendritic channels on both sides of the sand streak on Ward Terrace	PHV, LHV, LVV(LHH), PHH(VV), CHV, CHH(VV)
Flat, lag-covered surfaces on Ward Terrace	PHV, PVV, PHH, LHV, LVV, LHH, CHV, CHH, CVV
Barchan dunes in Landmark Tonahakaad Washes	PVV(HH), LHH, LVV, CHV, LHV**, PHV**, CHH, CVV
Contact of elongate sand sheets in Landmark and Tonahakaad Washes	CVV#, CHH, LVV, (not obvious on LHH,HV and PHH,VV,HV data)
Most recent drainage channels in Landmark Wash	(not detectable on images from pass B)
Full width of Landmark Wash	(not covered during pass B see Table 5; Fig. 18)
Roughness variations within the Little Colorado River channel	(not covered during pass B; see Table 5, Fig. 18)
# Far superior to all other SAR frequency/polarization modes	
**Somewhat obscured by image smear	